UNIVERSITY OF SOUTHAMPTON

FACULTY OF PHYSICAL & APPLIED SCIENCES

Optoelectronics Research Centre

Ultra-high spatial and temporal resolution using Scanning Near-field Optical Microscopy

Sam A. Berry

Thesis for the degree of Doctor of Philosophy

January 19, 2013

UNIVERSITY OF SOUTHAMPTON

ABSTRACT

FACULTY OF PHYSICAL & APPLIED SCIENCES
OPTOELECTRONICS RESEARCH CENTRE

Doctor of Philosophy

by Sam A. Berry

Scanning near-field optical microscopy (SNOM) is a system that can image beyond the conventional diffraction limit. It does this by collecting the information contained within evanescent fields. This unique ability to image using evanescent fields also enables SNOM to directly measure the electric field distribution in waveguides, where light is guided by total internal reflection.

When SNOM is used with a spectrally resolving detector, local temporal phenomena can be detected by analysing spectral interference in the spectra collected by the probe. This spectrally resolving configuration was used to directly measure inter-modal group velocity difference in a multimode ridge waveguide and, using the modes' spatial profiles to experimentally determine the mode amplitude coefficient ratio. Such an ability to provide measurements on the local dispersion characteristics and relative modal amplitudes of guided light establishes SNOM as a route for investigating the conversion of current single mode photonic devices into multimode devices.

The spectrally resolving SNOM system was also used to investigate the sources of temporal delays created by a quasi disordered scattering sample, which was based on John H. Conway's pinwheel tiling. Whilst the measurements do not create a complete picture of the scattering phenomena in this work, suggestions for improvement are offered with the aim establishing spectrally resolving SNOM systems as tools for mapping localised temporal phenomena in disordered scattering systems.

DECLARATION OF AUTHORSHIP

I, Sam A. Berry,
declare that the thesis entitled

Ultra-high spatial and temporal resolution using Scanning Near-field Optical Microscopy

and the work presented in the thesis are both my own, and have been generated by me as a result of my own original research. I confirm that:

- this work was done wholly or mainly while in candidature for a research degree at this University;
- where any part of this thesis has previously been submitted for a degree or any other qualification at this University or any other institution, this has been clearly stated;
- where I have consulted the published work of others, this is always clearly attributed;
- where I have quoted from the work of others, the source is always given. With the exception of such quotations, this thesis is entirely my own work;
- I have acknowledged all main sources of help;
- where the thesis is based on work done by myself jointly with others, I have made clear exactly what was done by others and what I have contributed myself;
- parts of this work have been published as:
  - Berry, S. A., Gates, J. C., & Brocklesby, W. S. (2011). Direct spatial-temporal discrimination of modes in a photonic lightwave circuit using photon scanning tunnelling microscopy. CLEO/Europe and EQEC 2011 Conference Digest (p. CF p19). Optical Society of America.
  - Berry, S. A., Gates, J. C., & Brocklesby, W. S. (2011). Determination of spatio-spectral properties of individual modes within multimode waveguides using spectrally resolved near-field scanning optical microscopy. Applied Physics Letters, 99(14), 141107.

Signed: Date:

ACKNOWLEDGMENTS

Well I can say that the last four years at the ORC have certainly been a journey of self-discovery, where the limits of my understanding, critical thinking, patience, and improvisation have all been tested thoroughly. It would, without a doubt, been an impossible journey had it not been for the valued input from many members of the ORC, friends, and family. Since I have limited space, I will mention a select few here.

First and foremost, huge thanks go to Dr James Gates and Dr Bill Brocklesby for converting me from a university graduate into a scientist. Their combined efforts and wisdom have enabled me obtain the practical and analytical skills required to endure the SNOM project. Their patience and guidance has been greatly appreciated.

Huge thanks also go to the members of the ORC for being there academically and socially, as required. Special thanks to Dr Peter Lanchester for ensuring I did not lose sight of my goals. Special thanks also go to the ultrafast x-ray group for letting me be part of them, developing my knowledge in scientific areas outside near field imaging and providing lab equipment when necessary; the same thanks also go to Prof Peter Smith's group.

Infinite thanks to my friends and family who, despite significant lack of contact (especially over the last two years) have stuck by me and are a phone call away when I need them. Finally, thanks to Simon who has remained at my side despite a significant devotion of my time and efforts to my work and community volunteering role.

Thank you all! :-)

CONTENTS

- CHAPTER 1 -

INTRODUCTION

This chapter gives background knowledge on microscopy and its history with details of milestones in scanning near-field optical microscopy (SNOM). It then contains details of previous experiments in which SNOM was applied to study waveguides of the type studied in this thesis. This chapter is then concluded with brief descriptions of the chapter contents.

1.1 FIELD OF RESEARCH

1.1.1 THE DIFFRACTION LIMIT

The scope of SNOM applications extend wide due to its nature as a characterisation tool for the nano-world. Conventional systems used to characterise optical devices depend on the collection of light after free-space propagation (usually from, but not limited to, an illuminating source). Typical examples of this are cells studied under a conventional microscope; the cells perturb the light from the illuminating source, the scattered waves propagate in free space and are collected by a detector. The limitation of such free-space propagation imaging systems is diffraction.

Propagating light cannot be confined to linear dimensions much smaller than $\frac{\lambda}{2n}$ inside a medium (where n is the refractive index of the medium and λ is the wavelength of the propagating light in a vacuum). The diffraction limit was first defined by E. Abbe in 1873[1]. It was then later re-arranged by Lord Rayleigh[2, 3] to the form

$$\delta x \geq \frac{1.22\lambda}{2n\sin\frac{\theta}{2}} \tag{1.1}$$

where θ is the full collection angle of light. Since this equation does not include a

factor for the "quality of components" of the imaging system, systems that use propagating light are fundamentally limited to this resolution. Diffraction limits the highest attainable resolution using a free-space optical microscope to between 200 - 300 nm.

The resolution of images beyond that of a conventional optical microscope requires a system that either uses an illumination source with shorter wavelengths or a propagating medium with a refractive index much larger than unity. Such systems exist (X-ray microscopy, electron microscopy & oil-immersion microscopy to name a few), but they do not enhance the resolution whilst accurately reflecting materials' electric-field responses at optical frequencies. There are some systems that use other physical principles to construct a super-resolution image of the sample, which will be discussed in chapter 2.

Since many objects in nature and nanotechnology are of the nanometre scale, imaging tools that use free-space propagating light are not appropriate for spatially resolving how these objects respond to light at optical and near infrared (NIR) frequencies. Abbe himself is reported to have suggested this limit would eventually be overcome [4].

1.1.2 THE WORLD OF MICROSCOPY

To understand where SNOM fits in the world of microscopy, we can consider the different techniques used to probe the microscopic world. The most famous (and oldest) device used to view the microscopic samples is the conventional microscope. The first published work of images from the microscopic world was Robert Hooke's *Micrographia*. In this publication, detail never witnessed before was presented in illustrations of everyday objects observed under a microscope. This desire to see a more detailed world resulted in new discoveries; most notably the existence of cells in biology. The microscope enhanced the resolving power of the eye by focussing light, scattered by an object, from a large numerical aperture (or acceptance angle). In pursuit of higher resolutions, the microscope drove the technology and science behind it; resulting in high-quality optics and the discovery of the diffraction limit.

Unable to defy the diffraction limit, technologies were created that either used a shorter (than visible light) illumination wavelength or did not rely on the propagation of light to resolve features. Two such examples are x-ray diffraction and scanning tunelling microscopy (STM). X-ray diffraction uses a small illumination wavelength to increase the maximum imaging resolution, whereas STM uses a probe-sample contact method to scan and generate topographic information to create an image; the absence

of propagating light here makes the probe the factor that determines the maximum resolution attainable. Scanning electron microscopy (SEM) uses both a shorter illumination wavelength and a scanning method. In a SEM, a beam of electrons is focussed to a small spot using magnetic lenses and the resultant scattered light depends on the local properties of the area where the beam hits the sample. By scanning the electron beam focus across the sample, an image can be created using the magnitude of scattered electrons detected and the position of the focussed beam. SEM images are the most common high-resolution images used to date because of its high resolution, ease of use, and well-understood technology. SEM had previously only been able to image metallic samples, since charge would build-up on non-conducting samples and affect the incoming electron beam, and consequently, the resulting image. However, recent developments in the technology has introduced a variable pressure SEM where charge can be channelled through the atmosphere in the SEM chamber, thus enabling insulating materials to be imaged, albeit with slightly reduced resolution.

Whilst these microscopy techniques are useful for observing topographical features of samples that are just a few atoms in size, the response of the sample to the light is lost; thus spectroscopy cannot reveal interesting localised properties. This makes analysing the local electric-field responses of nanometre-sized objects outside of simulations difficult. As the field of photonics follows examples from nature and looks towards nano structuring of materials to engineer optical properties, there is a necessity to measure and characterise such structures at optical frequencies beyond the resolution limited by diffraction.

1.1.3 Brief history of SNOM

In 1928, E. Synge proposed a method for imaging beyond the diffraction limit[5]; this method involved the collection of the non-propagating evanescent wave, which contains high-resolution spatial information not contained in propagating light. By scanning a sub-wavelength aperture between a sample and illumination source, the evanescent wave at the aperture can be scattered into a propagating wave, providing the aperture is in range of the evanescent wave. This propagating wave can then be detected in the far-field region. Due to the technological constraints in Synge's time, positioning an aperture in the region of the evanscent field of readily attainable wavelength was not possible, consequently his idea was not implemented for over 40 years.

The first example of imaging beyond the diffraction limit was achieved by Ash and Nichols using microwaves[6]. Ash and Nichols scanned a sub-wavelength aperture

across the sample and obtained images beyond the diffraction limit; features down to $\lambda/60$ were resolved where the wavelength used was $\lambda = 3\,\text{cm}$. This result demonstrated the validity of Synge's sub-wavelength resolution imaging technique and so the application of this technique at optical frequencies was the next challenge. The evanescent wave at optical frequencies, as will be discussed in chapter 2, only extends a few tens of nanometres from a sample's surface. The technology to maintain such sample-probe distances was not available until ten years later.

In 1982, Gerd Binnig's Nobel Prize winning scanning tunnelling microscope presented technologies to maintain a sample-probe contact distance of a few nano-metres using piezoelectric translation stages and a current feedback loop[7]. The nano-positioning technology was quickly adapted by Pohl *et al.* to create a SNOM probe, which obtained the first sub-wavelength resolution image at an optical frequency[8]. Pohl's work and later works have almost exclusively used a sharp probe, which allows the probe to come into contact with the surface and then scanned across it.

Evanescent waves are not exclusive to scattering phenomena, they are also present at the boundaries of total internal reflections. Probing the evanescent field, the ability of SNOM to measure guided light using photon tunnelling phenomena was quickly discovered[9] and thus a sub-field of SNOM called Photon Scanning Tunnelling Microscopy (PSTM) was born. This meant that measurements, including spectroscopy, on guided light could be achieved[10]; making SNOM a useful tool for observing phenomena in integrated optics.

1.2 SNOM ON WAVEGUIDE PHENOMENA

In integrated optics, characterising waveguides is important for classifying performance, limitations, and searching for new potential uses. PSTM provides a means of investigating various properties of integrated devices, one such is determining the dispersion properties of waveguides over millimetre distances. Conventional methods for measuring the propagation constants require measuring the inter-modal delay over long distances. These methods are not sufficiently sensitive for measuring the properties of integrated devices. PSTM is a well-suited method for analysing the properties of waveguides in integrated optics and can spectrally resolve the local electric field intensities when used with a spectrally resolving detector, providing a method to investigate temporal phenomena. This ability to resolve beyond the diffraction limit with femtosecond time resolution (when used with a spectrally broad illumination source) enables PSTM to determine many properties of waveguides and has already played an

active role in characterising their guiding properties[11–21]. Thus as the number of different photonic devices increases, so does the applications of PSTM.

The ability of SNOM to image beyond the diffraction limit also makes it useful for analysis on the spatial profile of propagating modes, which have profiles with dimensions comparable to half the wavelength of light inside the medium (which is usually smaller than when propagating in air). Measurements on modal profiles can be used to determine the numerical aperture of the waveguide for particular modes. Recent studies on inter-modal delays and the spatial dependence of such delays have enabled the complete modal decomposition of multimode fibre outputs[22]. Since SNOM can collect local spectra on a waveguide surface, these techniques can be directly transfered to SNOM experiments to obtain local information of inter-modal interactions in certain photonic devices; this spatial beating profile was originally discussed in a paper by Mills *et al.*[21] where SNOM was used to track delays between pulses propagating in a waveguide.

1.2.1 Measuring the group velocities of modes

The work by Mills *et al.* looked at the ability of a spectrally resolving SNOM to investigate temporal phenomena. The individual group velocities of the modes in a highly multi-mode waveguide, excited by a mode-locked pulsed laser, were measured relative to the fundamental mode by collecting spectra along the waveguide and applying a Fourier transform to the spectra to identify temporal delays[21]. This experiment determined the group velocity differences between propagating modes over millimetre distances. By tracking spectral interferences in an ultra-fast coherent broadband source, femtosecond group-delay differences were measured. An extension to this project is to use the spectral interference caused by modal dispersion with an incoherent source to determine the relative group velocities of the modes; this is the work presented in chapter 4 of this thesis. This provides a convenient tool for the characterisation of waveguides without the nonlinear effects seen from using a mode-locked laser source.

1.3 Thesis outline

Chapter 2 presents the physics used to describe how high spatial resolution images are collected by using near-field microscopy. The angular spectrum model of diffraction is presented to demonstrate how the spatial profile of an electromagnetic (EM) wave with

sub-wavelength detail changes with propagation distance due to diffraction. This is followed by a short discussion on resolution and a few methods that different imaging systems employ to attain images beyond the diffraction limit.

Chapter 3 deals with the construction of a spectral SNOM system. The various components of a SNOM setup are discussed in some detail. The performance limitations due to the different systems utilised in a SNOM setup are also discussed along with potential sources of artefacts in data when one of the systems do not perform as desired.

Chapter 4 presents the data collected for the measurement of the relative group velocity of modes to the fundamental using spectral interference measurements with an incoherent source of light. The significance of using an incoherent source is discussed, followed by the ability to discriminate the higher-order modes from one another. The chapter ends with a suggested extension of the method to measure higher-order propagation constants from the propagation constant Taylor expansion.

Chapter 5 presents data from a quasi-isotropic photonic bandgap device where the structure causes random walks of photons. With the ability to temporally resolve local delays in the structure, the setup is used to investigate whether a temporally discriminating SNOM setup can identify areas of localisation or provide evidence of other optical phenomena.

Chapter 6 summarises the major contributions of the work presented in this thesis with some suggestions on future work.

REFERENCES

[1] E Abbe. Beiträge zur Theorie des Mikroskops und der mikroskopischen Wahrnehmung. *Archiv für Mikroskopische Anatomie*, 9(1):413–418, December 1873.

[2] J W Strutt. XXXI. Investigations in optics, with special reference to the spectroscope. *Philosophical Magazine Series 5*, 8(49):261–274,403–411,477–486, 1879.

[3] J W Strutt. On the manufacture and theory of diffraction gratings. *Philosophical Magazine*, 47:91–93, 1874.

[4] H Volkmann. Ernst Abbe and His Work. *Appl. Opt.*, 5(11):1720–1731, November 1966.

[5] E H Synge. XXXVIII. A suggested method for extending microscopic resolution into the ultra-microscopic region. *Philosophical Magazine Series 7*, 6(35):356–362, 1928.

[6] E A Ash and G Nicholls. Super-resolution Aperture Scanning Microscope. *Nature*, 237(5357):510–512, June 1972.

[7] G Binnig, H Rohrer, Ch Gerber, and E Weibel. Surface Studies by Scanning Tunneling Microscopy. *Physical Review Letters*, 49(1):57–61, July 1982.

[8] D W Pohl, W Denk, and M Lanz. Optical stethoscopy: image recording with resolution lambda/20. *Applied Physics Letters*, 44:651, 1984.

[9] RC Reddick, RJ Warmack, and TL Ferrell. New form of scanning optical microscopy. *Physical Review B*, 39(1):767–770, 1989.

[10] Din Ping Tsai, Howard E Jackson, R C Reddick, S H Sharp, and R J Warmack. Photon scanning tunneling microscope study of optical waveguides. *Applied Physics Letters*, 56(16):1515, 1990.

[11] Sergey I Bozhevolnyi and Laurens Kuipers. Near-field characterization of photonic crystal waveguides. *Semiconductor Science and Technology*, 21(5):R1–R16, 2006.

[12] R J P Engelen, Y Sugimoto, H Gersen, N Ikeda, K Asakawa, and L Kuipers. Ultrafast evolution of photonic eigenstates in k-space. *Nature Physics*, 3(6):401–405, 2007.

[13] H Gersen, T J Karle, R J P Engelen, W Bogaerts, J P Korterik, N F van Hulst, T F Krauss, and L Kuipers. Direct observation of Bloch harmonics and negative phase velocity in photonic crystal waveguides. *Phys Rev Lett*, 94(12):123901, 2005.

[14] T Chaipiboonwong, P Horak, J D Mills, and W S Brocklesby. Numerical study of nonlinear interactions in a multimode waveguide. *Optics Express*, 15(14):9040–9047, 2007.

[15] M Foroni, F Poli, A Cucinotta, and S Seller. Scanning Near-Field Microscopy of Photonic Crystal Fibers. In *Transparent Optical Networks, 2006 International Conference on*, volume 2, pages 84–87, 2006.

[16] J C Gates, J D Mills, and W S Brocklesby. Near-field scanning optical microscopy of standing waves in fiber Bragg gratings. *Applied Physics Letters*, 83(9):1890–1892, 2003.

[17] H Gersen, J P Korterik, N F van Hulst, and L Kuipers. Tracking ultrashort pulses through dispersive media: experiment and theory. *Phys Rev E Stat Nonlin Soft Matter Phys*, 68(2 Pt 2):26604, 2003.

[18] C W J Hillman, W S Brocklesby, T M Monro, W Belardi, and D J Richardson. Structural and optical characterisation of holey fibres using scanning probe microscopy. *Electronics Letters*, 37(21):1283, 2001.

[19] Aaron Lewis, Udi Ben-Ami, Nily Kuck, Galina Fish, Dora Diamant, Lev Lubovsky, Klony Lieberman, Sharon Katz, Amir Saar, and Michael Roth. NSOM the fourth dimension: Integrating nanometric spatial and femtosecond time resolution. *Scanning*, 17(1):3–13, 1995.

[20] John D Mills, Tipsuda Chaipiboonwong, William S Brocklesby, Martin D B Charlton, Majd. E Zoorob, Caterina Netti, and Jeremy J Baumberg. Observation of the developing optical continuum along a nonlinear waveguide. *Optics Letters*, 31(16):2459, 2006.

[21] John D Mills, Tipsuda Chaipiboonwong, William S Brocklesby, Martin D B Charlton, Caterina Netti, Majd E Zoorob, and Jeremy J Baumberg. Group velocity measurement using spectral interference in near-field scanning optical microscopy. *Appl. Phys. Lett.*, 89(5):51101–51103, July 2006.

[22] J W Nicholson, a D Yablon, S Ramachandran, and S Ghalmi. Spatially and spectrally resolved imaging of modal content in large-mode-area fibers. *Optics Express*, 16(10):7233, May 2008.

- CHAPTER 2 -

IMAGING PHYSICS

The ability of SNOM to image at resolutions beyond the diffraction limit (equation 1.1) is achieved by converting the evanescent non-propagating wave into a propagating one. The evanescent field contains high-spatial frequency image information and also exists at boundaries of total internal reflection. In this chapter, the theory of light propagation is presented, including light with spatial frequencies beyond the diffraction limit. Also presented is a short discussion on resolution and resolvability and an explanation on how some recent imaging systems are able to attain images beyond the diffraction limit.

2.1 THE ANGULAR SPECTRUM MODEL

The angular spectrum model provides an insight into the information contained within the evanescent field. In the model, we can consider a 2D spatial distribution of an electric field at a single wavelength as a superposition of plane waves at different angles of incidence. This angular spectrum of plane waves can be used to decompose the spatial variation of electric fields and reveals the nature of the diffraction limit. The proof starts with the fundamental equations that describe electromagnetic fields; electromagnetic phenomena obey Maxwell's equations and take the following form in the

absence of free charges (SI units):

$$\nabla.\mathbf{D} = 0, \tag{2.1}$$

$$\nabla.\mathbf{B} = 0, \tag{2.2}$$

$$\nabla \times \mathbf{E} = -\frac{\partial}{\partial t}\mathbf{B}, \tag{2.3}$$

$$\nabla \times \mathbf{H} = +\frac{\partial}{\partial t}\mathbf{D}, \tag{2.4}$$

where $\mathbf{E}, \mathbf{D}, \mathbf{H}$, and $\mathbf{B}$ are the electric field, electric displacement, magnetic field, and magnetic flux respectively. By taking the curl of equation 2.3 and then substituting in equation 2.4, the wave equation for light propagation in a homogeneous amorphous medium can be expressed as

$$\nabla^2\mathbf{E} = \frac{n^2}{c^2}\frac{\partial^2}{\partial t^2}\mathbf{E}, \tag{2.5}$$

where $n = \sqrt{\varepsilon_r \mu_r}$ is the refractive index of the medium and $c \approx 3 \times 10^8$ m s^{-1} is the speed of light. For the angular spectrum model, the idealised case of monochromatic illumination can be used. In such a case, an electric field solution to equation 2.5 can take the following form

$$\mathbf{E} = \mathbf{E}_0 \exp[\mathrm{i}\mathbf{k}.\mathbf{r}] \exp[-\mathrm{i}\omega t], \tag{2.6}$$

which is the equation for a plane wave with $k = n\omega/c$ where ω is the angular frequency of the field. When this expression is substituted into equation 2.5, the result is the Helmholtz wave equation for an electric field. The Helmholtz equation describes the spatial evolution of an electric field disturbance in a homogeneous medium and is described by the following

$$\nabla^2\mathbf{E} + k^2\mathbf{E} = 0, \tag{2.7}$$

where k is the scalar wavenumber of the wave. Because this equation describes the spatial evolution in a homogeneous medium (*e.g.* air), it can be used to identify the source of the diffraction limit. The impact the Helmholtz equation has on an image, which is described by an electric field with varying amplitude and phase across an image plane, whilst it propagates orthogonally from the image plane can be investigated.

If a sample is illuminated with a plane wave at normal angle of incidence, then the reflected wave at the surface will have an electric-field amplitude profile proportional to the complex reflectivity profile $r(x,y)$ of the sample's surface (in this case the surface

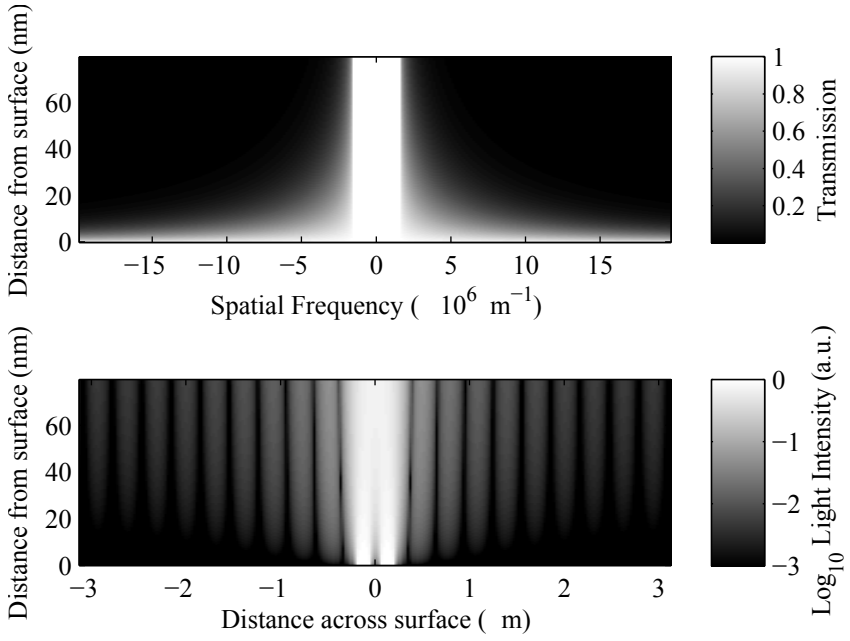

Figure 2.1: (top) The extent at which spatial frequency components exist from the surface due to diffraction for a wavelength of 633 nm, as determined by the exponential in equation 2.14. (bottom) The resulting image of two 100 nm apertures spaced 260 nm apart at different distances from the apertures using an illumination wavelength of 633 nm, calculated using the spatial frequency restrictions imposed by equation 2.14. By observing how, after just propagating 80 nm away from the surface, the two apertures are no longer resolvable, the short distance over which loss of image detail occurs can be appreciated.

is in the *xy* plane). Since the Helmholtz equation describes how an electric field varies in terms of the wave vector, it is useful to describe the surface reflectivity profile in terms of spatial frequency

$$\tilde{r}(u,v) = \frac{1}{2\pi}\iint_{-\infty}^{+\infty} \mathrm{d}x\,\mathrm{d}y\; r(x,y,0)\exp\Big[-\mathrm{i}2\pi(ux+vy)\Big], \tag{2.8}$$

where u & v are the spatial frequencies in the x & y directions respectively. The reflected electric field in the spatial domain can now be written as a function of $\tilde{r}$

$$\mathbf{E}(x,y,0) = 2\pi\mathbf{E}_0\iint_{-\infty}^{+\infty} \mathrm{d}u\,\mathrm{d}v\; F(u,v)\exp\left[\mathrm{i}\frac{2\pi}{\lambda}(\lambda ux+\lambda vy)\right] \tag{2.9}$$

$$= \mathbf{E}_0\iint_{-\infty}^{+\infty} \mathrm{d}u\,\mathrm{d}v\; F\left(\frac{\alpha}{\lambda},\frac{\beta}{\lambda}\right)\exp\Big[\mathrm{i}k(\alpha x+\beta y)\Big], \tag{2.10}$$

where λ is the wavelength and F (Fourier amplitudes) is the relative amplitudes of the plane wave with spatial frequencies u & v and is known as the scalar wave solution. α

and β represent direction cosines such that

$$F(u,v,) \propto \tilde{r}(u,v),$$
$$\alpha = \lambda u \qquad \text{and} \qquad \beta = \lambda v. \tag{2.11}$$

Equation 2.10 is the angular spectrum model that states mathematically that any spatial distribution of the electric field can be written as a superposition of plane waves with different directions cosines. Thus far, the direction normal to the plane of the surface/image (the z-axis in this case) has been ignored. It is introduced by adding a z axis dependency in the F term

$$\mathbf{E}(x,y,z) = \mathbf{E}_0 \iint_{-\infty}^{+\infty} F\left(\frac{\alpha}{\lambda},\frac{\beta}{\lambda},z\right) \exp\Big[\mathrm{i}k(\alpha x+\beta y)\Big]\,\mathrm{d}u\,\mathrm{d}v, \tag{2.12}$$

which now describes the electric field in 3D space by describing the electric field at a distance z from the surface as a sum of plane waves with different spatial frequencies in the surface plane. The relationship between $F\left(\frac{\alpha}{\lambda},\frac{\beta}{\lambda},z\right)$ and $F\left(\frac{\alpha}{\lambda},\frac{\beta}{\lambda}\right)$ can be found using the Helmholtz equation (equation 2.7). For equation 2.12 to obey the Helmholtz equation, the following must be upheld

$$\frac{\mathrm{d}^2}{\mathrm{d}z^2}F\left(\frac{\alpha}{\lambda},\frac{\beta}{\lambda},z\right) + k^2(1-\alpha^2-\beta^2)F\left(\frac{\alpha}{\lambda},\frac{\beta}{\lambda},z\right) = 0, \tag{2.13}$$

which dictates that

$$F\left(\frac{\alpha}{\lambda},\frac{\beta}{\lambda},z\right) = F\left(\frac{\alpha}{\lambda},\frac{\beta}{\lambda}\right) \exp\left[-\mathrm{i}kz\sqrt{1-\alpha^2-\beta^2}\right]. \tag{2.14}$$

This solution determines the how far, and to what extent, waves of various spatial frequencies $\left(\frac{\alpha}{\lambda},\frac{\beta}{\lambda}\right)$ can exist away from the surface at a particular wavelength. This solution is plotted numerically in figure 2.1 (top) as a tranmission mask for a spatial frequency propagating a distance away from the sample. The x axis the spatial frequency profile of the sample and the y axis represents the distance at which the corresponding spatial frequencies can propagate (or not) according to the restriction imposed by the exponential function in equation 2.14 (*i.e.* the diffraction limit); white represents a 100% tranmission and black represents 0 transmission. The central white column represents the spatial frequencies within the diffraction limit, thus they successfully propagate away from the surface. Spatial frequencies that represent image detail beyond the diffraction limit are attenuated and do have an electric field presence

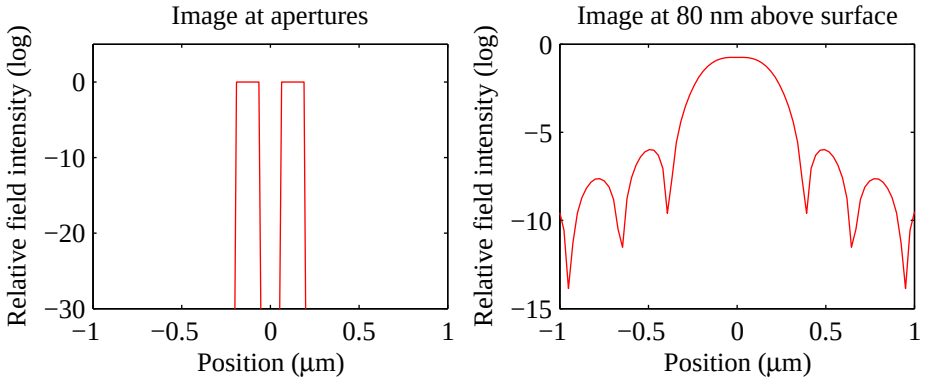

Figure 2.2: The image intensity plots of two 100 nm wide apertures spaced 260 nm apart in a dielectric medium at the aperture surface and a distance of 80 nm for a wavelength of 633 nm. On the left is the numerically simulated image which takes into account all the spatial frequencies required to create an image unrestricted by the diffraction limit, the right shows the image with the high spatial frequencies limited by diffraction; even with a log scale, the two peaks cannot be resolved.

further than 80 nm from the sample surface. It can be seen in this plot, that to achieve resolutions corresponding to just $\lambda/10$ (15×10^6 m^{-1}), the image collection device need to be accessing the scattered light at just 10 nanometres away from the surface.

The bottom plot in figure 2.1 is a numerical simulation of the highest resolution image (across x axis) attainable by collecting the light a distance away from the sample surface (y axis). The image is two 100 nm slits spaced 260 nm, using an illumination wavelength of 633 nm. After a propagation of a few tens of nanometres away from the sample surface, the sharp edges of the slits disappear and the two slits begin to blur into one intensity maximum, which causes the two slits to become unresolvable after propagating 80 nm. Also demonstrated in this figure is the appearance of diffraction fringes caused by the clipping of the spatial frequencies available to reconstruct the image after propagation.

Recalling equation 2.11, which describes how an electric field propagates away from the surface (z-axis) in terms of the electric field's spatial frequencies in the x-y plane. If the spatial frequency of the field in the plane of the surface is less than the spatial frequency of the illuminating wave (i.e. $u^2+v^2 < \frac{1}{\lambda^2}$ or $\alpha^2+\beta^2 < 1$), then the square-root term is real and so equation 2.14, oscillates in the z direction. However, if the spatial frequency of the electric field in the plane of the surface is greater than the spatial frequency of the illuminating wave, then the square root is imaginary and so the exponential term attenuates the electric field with increasing z; as shown in figure 2.1.

The resulting effect of this attenuation of high spatial frequencies can be observed

numerically in figure 2.2. In this figure a hypothetical slit structure, with dimensions smaller than the diffraction limit, is decomposed into its spatial frequency components and then combined with the solution from equation 2.14 using an illumination wavelength of 633 nm. Using the remaining spatial frequencies, the image is reconstructed and loss of resolvability of the two slits is clearly evident at just 80 nm away from the sample's surface.

2.2 RESOLUTION AND RESOLVABILITY

It is important in microscopy to differentiate between resolution and resolvability. This section aims to discuss the difference between the two with an aim for providing a definition for the resolution of an imaging solution, which is yet to receive a rigorous formal definition. The explanation of resolution and resolvability is written to assist the interpretation of resolution for typical sample types scanned using SNOM, where no features of the sample can be assumed.

The definition of resolution varies amongst the research community and is usually quoted as the value that gives the best resolution. Unfortunately, most often this is giving the value of the dimensions at which a known sample can be resolved. This often uses *a priori* knowledge of the sample to eliminate alternative interpretations of the results. The Oxford English dictionary (OED) defines resolution as *"The smallest interval measurable by a telescope or other scientific instrument"*[1], whereas the definition of resolve when applied to optical or photographic equipment is *"separate or distinguish between (closely spaced objects)"*[1]. Clearly the major difference between the definitions is the use of the word "objects". If one knows something about the object under study, the smallest interval measurable can be smaller than the smallest interval of the electric field oscillation.

This is best explained by considering figure 2.3, where numerical simulations of the diffraction limited image of two narrow slits with width w and separation d (from the edges) are presented. In (a), two slits much wider than the diffraction limit are spaced relatively far apart. They are clearly resolvable despite the interference fringes caused by diffraction. In (b), two slits with the same width as (a) are presented with their separation at the Rayleigh criterion. With this separation, the intensity is able to drop to zero and thus the fact that two separate slits are present is clear. In (c) however, two sub-wavelength slits ($< 6\lambda$) are separated at the Rayleigh criterion. It is clear now that the two slits are resolvable (the two slits can be separated), but are now beyond

[1] Oxford English dictionary 2012

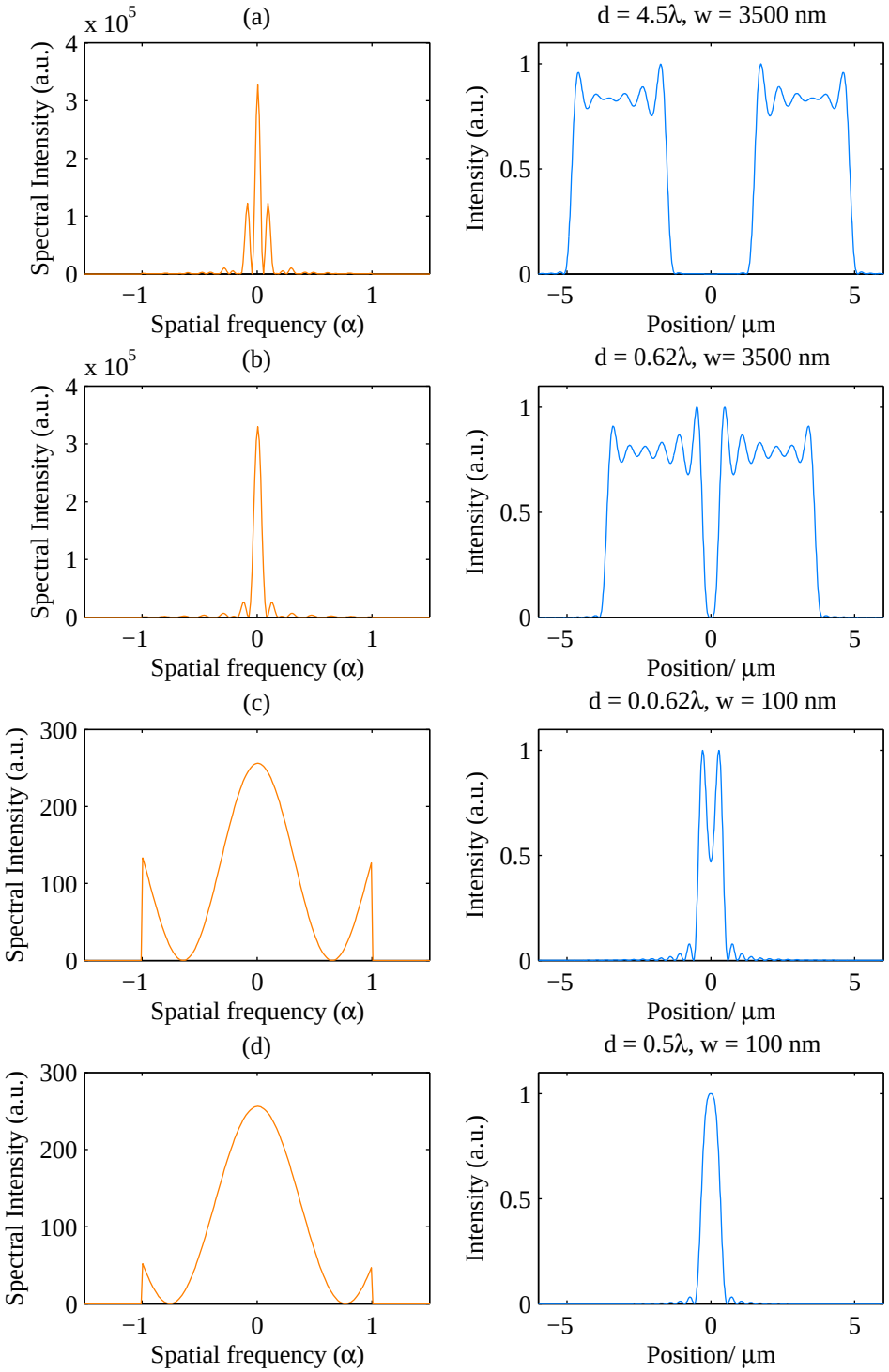

Figure 2.3: The numerical simulation of a prepared image at the diffraction limit (right) for different slit widths (w) and separations (d), alongside their Fourier spectra (left).

the resolution of the system; if the sample cannot be relied upon, we can no longer say with any certainty that there is a gap between the two slits since the intensity does not go to zero between the two peaks. This would prevent the detection of a failure during fabrication of such a hypothetical structure, since what is imaged is not a true reflection of the absorption profile at the required distance scale. Similarly in (d), the intensity profile no longer has two peaks and so it is not clear whether the image recorded is a true reflection of the object imaged since there are intervals smaller than the limit imposed by diffraction. A more precise definition of resolution must consider contrast and signal to noise ratio. A comprehensive review of resolution has been done previously[1].

To summarise the key issue, if a sample is known to consist of features much smaller than the diffraction limit, then using *a priori* knowledge about the sample under study will lead to the ability to resolve features. In such a case, the resolvability lies in there being features in its Fourier spatial frequency map. Using this technique, Astronomers are able to separate stars that are above the Sparrow limit (where the mathematical concept of resolvability lies in there being sufficient contrast in interference fringes in the image's spatial frequency map.

In microscopy however, it is more common that nothing about the sample can be assumed and so a result like the one presented in figure 2.3(c) could be interpreted as one larger slit with a slightly opaque centre. The only way of being sure that what is being measured is a true reflection of the sample is if the dimensions of the sample fall within the resolution of the imaging system; in other words, if the smallest interval of measurable contrast change occurs at the Rayleigh criterion.

Since the fundamental limit on resolution exists because of a restriction of spatial frequencies, it seems natural that a definition of resolution should depend on the spatial frequencies detected by the imaging system. Thus, the author believes that a standard definition of resolution should be based on the ability to measure a spatial frequency with a threshold above noise. As shall be seen in chapter 3, the ability of SNOM to image beyond the diffraction limit is demonstrated by displaying the spatial frequencies it has imaged.

2.3 SUB-WAVELENGTH IMAGING TECHNIQUES

The final section in this chapter provides a brief discussion of the current imaging techniques used to obtain images beyond the diffraction limit. The methods described, including SNOM, here employ scanning or fitting techniques to determine the spatial

dependence of intensity of light, which in certain circumstances means that the resolution of the device is not affected by the range of spatial frequencies detected (*i.e.* not affected by the diffraction limit). SNOM was, until recently, the only microscopic method available to obtain images beyond the diffraction limit. In the past decade other techniques including stochastic optical reconstruction microscopy (STORM), fluorescent microscopy with one nanometre accuracy (FIONA), stimulated emission depletion microscopy (STED), and superoscillation microscopy. These techniques have evolved from physical principles, known for some time, for going beyond the diffraction limit which are discussed in the following sections. However, these systems do not interact with the evanescent wave and thus are unsuitable for the characterisation of waveguides or samples that require the detection of evanescent waves, this limits their application in the field of photonic device characterisation.

2.3.1 STOCHASTIC OPTICAL RECONSTRUCTION MICROSCOPY

It has been demonstrated that small light emitting structures can be located to an arbitarily high precision by considering the cross-correlation of an image with an image 'kernel'[2]. This interesting method does not enhance resolvability of two features, but can accurately locate the position of emitters with separations much greater than the diffraction limit. A single molecule will emit its fluorescent such that it can be imaged as a diffraction limited sinc function whose central feature, or point spread function (PSF) has width of $\frac{1.22\lambda}{\mathrm{NA}}$. This PSF function can be fitted to a Gaussian function whose central position and respective uncertainty provide the location and accuracy of the location. This technique has been called fluorescent imaging with one nanometre accuracy (FIONA, more affectionately)[3].

This ability to locate light emitters with arbitrary precision is used in a new form of microscopy called stochastic optical reconstruction microscopy (STORM). In this form of microscopy, photo-switchable fluorophores are located using the method described above with FIONA. What gives STORM the ability to image beyond the diffraction limit is the controllable way the fluorophores can be turned off and on. Starting with all the fluorophores turned off, a low intensity pulse is used to activate a small fraction of the fluorophores. Ideally all the activated flurophores are a significant distance, in regards to the diffraction limit, away from one another. Once all the fluorophore locations are determined from their controlled fluorescence they are switched off. This process is repeated until as many fluorophores are possible are located[4].

Since the propagation of light can be described by Maxwell's equations, we can

use Gaussian beam optics to describe the behaviour of the light detected in three dimensions. By collecting spatial dependence of light with the collection optics position, the axial position of the fluorescent molecule can be detected. The advantage of this technique is that a 3 dimensional map of fluorescent molecule positions can be determined with an accuracy that is limited by the signal-to-noise ratio (SNR) instead of the diffraction limit[5]. The only limitation that restricts this imaging technique is molecules that fluoresce with the same wavelength must be separated by a distance greater than the diffraction limit.

The most obvious limitation with this technique, is that is requires the sample to be prepared with photo-switchable flurophores. Thus STORM's greatest field of application is in biochemistry where organic matter can be tagged with various fluorophores.

Other fluorescent microscopy methods

Other fluorescent microscopy techniques have demonstrated the ability to image beyond the diffraction limit. Most notably two photon absorption[6] and stimulated emission depletion (STED) microscopy[7]. These two techniques beat the diffraction limit by measuring the emission of fluorescence from a small excitation PSF and scanning. In two photon absorption, the PSF function of fluorescence is reduced by carefully overlapping the two pump wavelength PSFs. In such a case, excitation of the fluorescent sample only occurs where the two pump PSFs overlap. In STED an excitation beam, with a diffraction limited PSF, excites the fluorescent sample and then two "STED" pulses are used to stimulate emission at the outer extents of the original excitation PSF; the resulting spontaneous emission from the sample is recorded at various locations to construct an image.

2.3.2 SUPEROSCILLATIONS

Of the various methods used to obtain images with resolution greater than the diffraction, the superoscillation method is the most intriguing. In this system, an illumination spot of linear dimensions smaller than the diffraction is carefully prepared using a delicate balance of spatial frequencies; the study of such phenomena where a field oscillates faster than its highest Fourier component, yet still obeys the bandwidth and baud rate limits for information exchange, has attracted interest in signal processing and quantum field theory[8–11]. This spot is used to illuminate a sample and the reflected light recorded as the spot is scanned across the surface, in technique similar to STORM where the resolution now depends on the width of the spot and the precision

of the scanning optics.

This spot is created from a super-lens (a phase mask used to create the conditions necessary for a sub-wavelength spot) from the far-field region and the reflected light is collected from the far field region, this use of propagating light appears to violate the diffraction limit. The preparation of this sub-wavelength feature spot has been theoretically predicted since 1949[12].

What at first may appear to be an exception to the diffraction limit, can actually be explained using the concept of resolvability discussed in the previous section. This "nanoscope", as described by its implementers, is a scanning technique. As such, the retrieve image is a convolution of the small feature and the reflectivity/absorptivity (depending on mode of operation) of the sample. The reason this technique can retrieve information beyond the diffraction limit is because the diffraction limit does not affect the positional knowledge of the source spot. The size of the spot is one of two limiting factors, although it is undoubtedly at present the main factor; the remaining factor being the ability to precisely position the created spot.

A group at the University of Southampton has successfully used this technique to resolve features beyond the diffraction limit[13]; this has been confirmed by analysing the spatial frequencies present in their retrieved imaged.

The main drawback of this technique is that super-oscillations require huge dynamic range in intensity; the generated spot contains only a small fraction of the incident optical power. For a diffraction limited feature that oscillates at $\lambda/10$, side lobe intensities of 25 orders of magnitude greater are generated close to the oscillation for the class of superoscillation functions under study at the University of Southampton. The other drawback is that the preparation of a sub-wavelength, diffraction-limited feature requires a delicate balance of spatial frequencies, the ability to image surfaces with comparable topography is, at present, beyond the scope of this technique; this severely limits the samples and geometries that can be imaged.

2.3.3 Imaging with the evanescent wave

It is not surprising that the interaction between a SNOM probe and evanescent waves has been studied to some detail [14–18]; it is this interaction that enables SNOM to image beyond Abbe's diffraction limit. There are different ways a SNOM probe can interact with the evanescent field, this defines its type of probe. The different types of SNOM probe can be generalised into two categories: scattering probes and aperture probes[19].

Scattering probes, or apertureless probes, are probes which aim at detecting non propagating waves by the use of an optical antenna. The first reported use of such a probe was from [20]. More commonly aperture probes consist of a transparent tip with a small (ideally spherical) metal particle at the apex[21]. Under certain illumination, the presence of a small metallic particle acts as a dipole that can interact with the sample.

The other, and more common, type of probe used for SNOM is the aperture probe. This is usually an optical fibre pulled down to a tip with dimensions of a few tens of nanometres; in this form, the numerical aperture of the fibre is the aperture of the probe. This fibre tip can be coated in a metal to form a smaller (than uncoated) aperture at the apex. This coating is not required in situations where only the non-propagating, evanescent, fields exist; which is usually the case in photon scanning tunnelling microscopy. Without an aperture, scattered propagating light can reduce the resolution of the system since the detected signal is a convolution of the tip's PSF and the sample's light intensity.

REFERENCES

[1] A J den Dekker and A van den Bos. Resolution: a survey. *Journal of the Optical Society of America A*, 14(3):547, March 1997.

[2] J Gelles, B J Schnapp, and M P Sheetz. Tracking kinesin-driven movements with nanometre-scale precision. *Nature*, 331(6155):450–3, March 1988.

[3] Ahmet Yildiz, Joseph N Forkey, Sean a McKinney, Taekjip Ha, Yale E Goldman, and Paul R Selvin. Myosin V walks hand-over-hand: single fluorophore imaging with 1.5-nm localization. *Science (New York, N.Y.)*, 300(5628):2061–5, June 2003.

[4] Michael J Rust, Mark Bates, and Xiaowei Zhuang. Sub-diffraction-limit imaging by stochastic optical reconstruction microscopy (STORM). *Nature methods*, 3(10):793–5, October 2006.

[5] A M van Oijen, J Köhler, J Schmidt, M Müller, and G J Brakenhoff. 3-Dimensional super-resolution by spectrally selective imaging. *Chemical Physics Letters*, 292(1-2):183–187, July 1998.

[6] Stefan W. Hell. Improvement of lateral resolution in far-field fluorescence light microscopy by using two-photon excitation with offset beams. *Optics Communications*, 106(1-3):19–24, March 1994.

[7] Stefan W Hell and Jan Wichmann. Breaking the diffraction resolution limit by stimulated emission: stimulated-emission-depletion fluorescence microscopy. *Optics Letters*, 19(11):780, June 1994.

[8] Paulo J S G Ferreira and Achim Kempf. The energy expense of superoscillations. In *EUSIPCO-2002, XI European Signal Processing Conference*, page 347, 2002.

[9] Achim Kempf. Black holes, bandwidths and Beethoven. *Journal of Mathematical Physics*, 41(4):2360, 2000.

[10] M V Berry and S Popescu. Evolution of quantum superoscillations and optical superresolution without evanescent waves. *Journal of Physics A: Mathematical and General*, 39(22):6965–6977, June 2006.

[11] Yakir Aharonov, Jeeva Anandan, Sandu Popescu, and Lev Vaidman. Superpositions of time evolutions of a quantum system and a quantum time-translation machine. *Physical Review Letters*, 64(25):2965–2968, June 1990.

[12] Harold Osterberg and J Ernest Wilkins jr. The Resolving Power of a Coated Objective. *Journal of the Optical Society of America*, 39(7):553, July 1949.

[13] Edward T F Rogers, Jari Lindberg, Tapashree Roy, Salvatore Savo, John E Chad, Mark R Dennis, and Nikolay I Zheludev. A super-oscillatory lens optical microscope for subwavelength imaging. *Nature Materials*, 11(5):432–435, March 2012.

[14] J M Vigoureux, C Girard, and D Courjon. General principles of scanning tunneling optical microscopy. *Optics Letters*, 14(19):1039, October 1989.

[15] C Girard and D Courjon. The role of scanning mode in near-field optical microscopy. *Surface Science*, 382(1-3):9–18, 1997.

[16] D Van Labeke and D Barchiesi. Scanning-tunneling optical microscopy: a theoretical macroscopic approach. *Journal of the Optical Society of America A*, 9(5):732, May 1992.

[17] D Barchiesi and D Van Labeke. Application of Mie Scattering of Evanescent Waves to Scanning Tunnelling Optical Microscopy Theory. *Journal of Modern Optics*, 40(7):1239–1254, July 1993.

[18] D Van Labeke and D Barchiesi. Probes for scanning tunneling optical microscopy : a theoretical comparison. *Journal of the Optical Society of America A*, 10(10):2193, October 1993.

[19] D W Pohl. Optics at the nanometre scale. *Philosophical Transactions: Mathematical, Physical and Engineering Sciences*, 362(1817):701–717, 2004.

[20] U C Fischer and D W Pohl. Observation of single-particle plasmons by near-field optical microscopy. *Physical review letters*, 62(4):458–461, 1989.

[21] T Kalkbrenner, M Ramstein, J Mlynek, and V Sandoghdar. A single gold particle as a probe for apertureless scanning near-field optical microscopy. *Journal of microscopy*, 202(Pt 1):72–6, May 2001.

- CHAPTER 3 -

A PRACTICAL SNOM PROBE

This chapter discusses the construction and use of the SNOM setup used to collect the data in this thesis. The contents of this chapter present the methods used to realise a SNOM system and details the various roles of the different components and how they are used to probe the near-field region.

3.1 THE SNOM SETUP

Obtaining electric field data in the near-field region of a sample requires three main components: a sub-wavelength aperture/probe, a surface detection feedback loop, and nanometre-precision positioning. The following sections deal with the realisation and characterisation of each of these components, each component is critical for obtaining a near-field, sub-wavelength image. This is because of the non-propagating nature of the evanescent field; scanning a probe within the evanescent field region is the ultimate goal of a SNOM setup. An overview of the SNOM setup used in this thesis is presented in figure 3.1. The pink boxes represent the surface detection feedback system, the green boxes represent the positioning system, and the blue boxes represent the probe (and data collection) part of the SNOM.

The following sections will discuss the various methods used to realise the components of a SNOM probe, highlighting their advantages and disadvantages. Section 3.2 will present two methods used to create near field probes out of commercially available optical fibre.

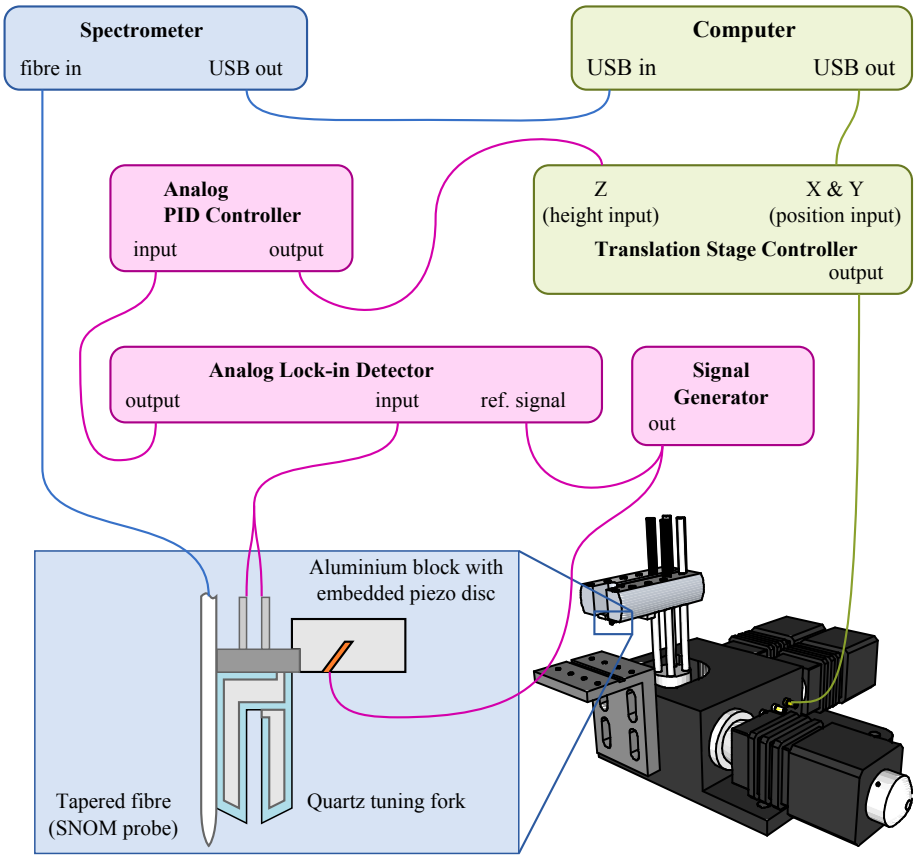

Figure 3.1: A schematic diagram of a typical spectral SNOM setup. The pink boxes and lines represent the force-feedback loop; the blue box and lines represent the spectral data collected by the SNOM tip; and the green boxes and lines represent the position controllers for the SNOM tip.

3.2 SNOM PROBES

A sub-wavelength aperture is required for obtaining images beyond the diffraction limit. Synge's original idea invovled sending light through a sub-wavelength hole and scanning this hole across the sample under investigation[1], collecting the scattered light in the far-field region. The first realised interpretation of this sub-wavelength hold was achieved by Pohl *et al.*[2] by using a quartz crystal tip coated in gold with a sub-wavelength aperture at the apex. Near field probes are more commonly made from optical fibre, which enables easy guidance to a detector and an intrinsic aperture from the guidance condition imposed by the core-cladding boundary. There are two common methods used today for creating near field probes out commercial fibre optics. The first involves a chemical etching process and the second is heating and mechanically pulling a fibre optic apart. The following sections detail the these processes and how they can be coated to create an aperture probe.

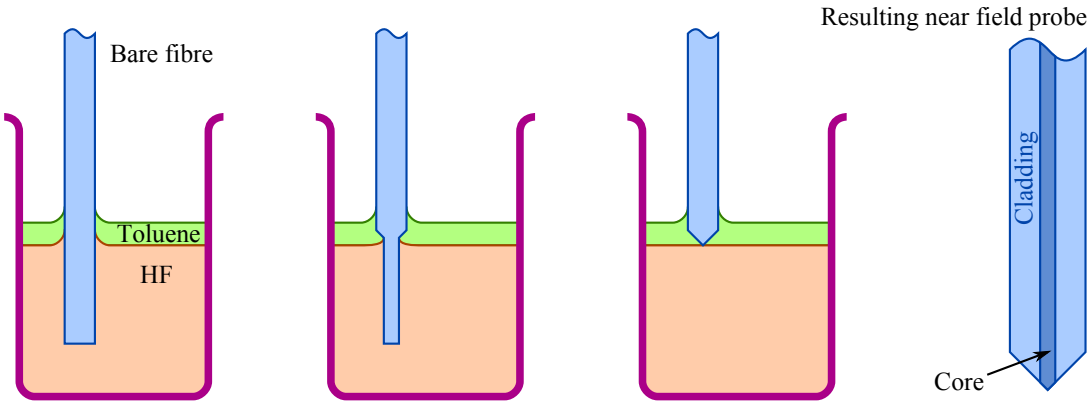

Figure 3.2: An exaggerated diagram of the wet etching method for creating near field probes out of optical fibres. From left to right depicts how, over time, the etching process forms a tip. A schematic of the resulting fibre is showed at the end. Note that the core's radius remains constant while the cladding is etched. Toluene was the organic solvent protective layer used for creating fibres in this work.

3.2.1 Etching fibres

The chemical etching method, as patented by Turner[3], is achieved by leaving a cleaved fibre in an etching solution. An organic solvent floats on top of the etching solution (Hydrofluoric acid) to prevent vapours from etching the fibre that is outside the solution and for controlling the depth of the meniscus at the fibre-acid boundary[4]. The meniscus that is created by the presence of the fibre in the etching solution causes a taper to be created. This meniscus method for creating a taper is shown diagrammatically in figure 3.2.

Using this method, the core remains a constant diameter until the tapered region reaches the core. A large core enhances the transmission of the tapered fibre, which is an advantage since SNR is usually the limiting factor in SNOM scans. Another advantage with this method is that several probes can be etched at the same time and the results are repeatable. By introducing extra etching steps, the profile of the apex can be controlled[5]. The doping ratio of the fibre core and cladding can also affect the taper angle, adding an extra route to modify the etching result[6].

The main disadvantage is the acid used to etch silica is HF, which is highly toxic, as are the waste products. The precautions necessary for this type of fabrication make the turnaround for this method lengthy, compared with the alternative. Another disadvantage is that the etched surfaces are rough and this can reduce throughput due to scattering out of the probe.

It has been demonstrated that this etching process can be enhanced by performing

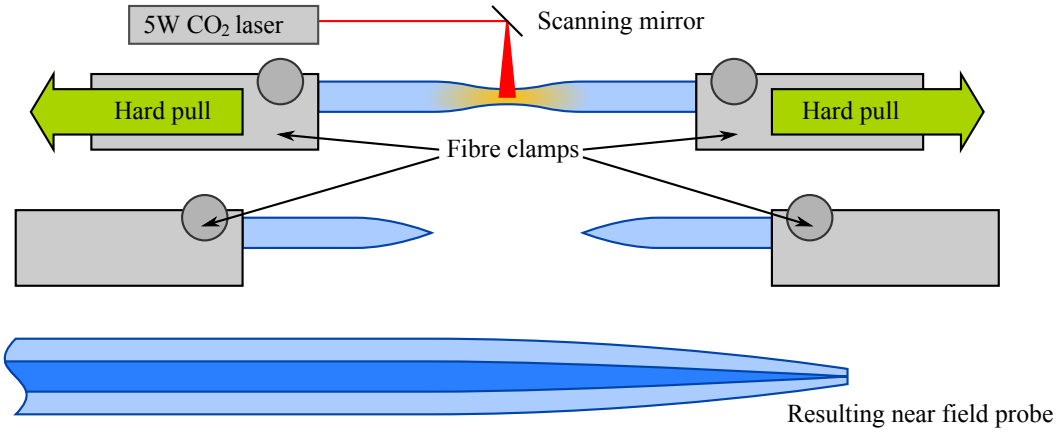

Figure 3.3: A diagram of the mechanical pull process. A CO_2 laser is focussed and scanned across a fibre, which is kept under a constant tension by the fibre clamps. When the fibre melts, the constant tension causes movement of the fibre. The puller monitors this velocity and once a certain velocity is reached, a hard pull is used to pull the fibre into two parts. The resulting fibre is a near field probe that has a slowly decreasing core size.

this etching process without removing the fibre's acrylate jacket[7, 8]. The result of this "tube etching" method generates smoother etched surfaces, enhancing the transmission and quality of any metallic coating used for an aperture. The acrylate jacket covering the fibre can be removed by dissolving after the etching processes.

3.2.2 PULLING NEAR FIELD PROBES

The most convenient method for creating near field probes, and the method used to create probes for all the data presented in this thesis, is the mechanically drawn method. The way this methods works is depicted in figure 3.3. A fibre is held into position and put under a constant tension by some clamps. Then a CO_2 laser with a controllable power output is focussed onto the fibre by a concave mirror, whilst being scanned in a pattern determined by the operator. When the fibre starts to melt, the clamps applying the tension begin to drift apart. When the clamps start to move at a specified velocity, a trip point is triggered and either a hard pull will be activated or the laser will be turned off (depending on the delay value). The delay represent the time delay between the laser switching off and the hard pull. A delay value less that 128 causes the trip point to start the hard pull with the laser running for a certain time, a delay greater than 128 causes the trip point to switch the laser off and wait a certain time before initiating a hard pull. Such fine control over the mechanical pulling process enables the fabrication

HEAT	320
FILAMENT	0
VELOCITY	18
DELAY	126
PULL	150

Table 3.1: The parameters used to created near field probes using the Sutter P-2000 commercial micro-pipette machine.

of tailored near field probes, where a trade off between aperture size and transmission efficiency can be chosen.

The resulting near field probes are highly customisable with the pulling parameters: HEAT, FILAMENT, VELOCITY, DELAY, and PULL[9]. HEAT specifies the output power of the laser. The FILAMENT parameter controls the scanning pattern of the laser beam on the fibre. The VELOCITY parameter sets the trip speed for the fibre clamps. The DELAY parameter sets the delay between the laser off and hard pull. The PULL parameter sets the force of the hard pull which is achieved by a solenoid with a controllable current supplied. The resulting effect of these parameters on the near field probe created has been studied[10] and the values used to create near field probes in this work is presented in table 3.1.

The main advantage of this method, over wet etching, is that it is very quick and easy. All the safety precautions necessary are achieved by design of the puller instrument. The results are highly repeatable and result in smooth tapers. The difference between near field probes created using this method and wet etching, is that the fibre's core radius reduces along the taper region. This results in reduced transmission down the fibre.

The primary reason for using the mechanical pulling method for creating near field probes in this thesis is because of the fast turnaround; a probe can be created in less than five minutes. Both methods have been praised for producing probes suitable for SNOM[11].

3.2.3 Creating aperture probes

Thus far, the near field probes discussed have exclusively been bare fibres. These kind of near field probes are known as apertureless probes. In such probes, the best attainable resolution is based on the size of the mode that propagates down the taper region (which can be bigger than the tip itself) and the amount of scattered light that can be coupled into the fibre at a location away from the apex. A metallic coating

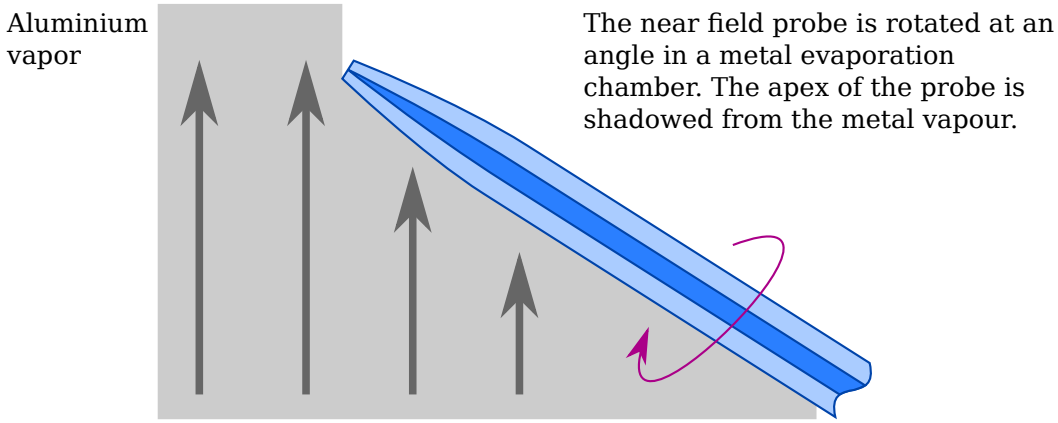

Figure 3.4: A diagram of the coating method for near field probes. The near field probe is rotated in a metal evaporation chamber so that an even coating is deposited on the fibre. The near field probe is rotated at an angle such that the apex of the probe is shadowed from the metal vapour. The resulting probe has an aperture at the apex, through which light can propagate and be guided.

can be deposited to restrict the size of the PSF of the near field probe and prevent any coupling of light at a location other than the aperture, which enhances the resolution attainable.

The method used to coat the near field probes in this work was a shadow evaporation method. The probe is placed inside a vacuum chamber on a mount that rotates the probe at a constant rotation speed. Once a vacuum is created, a tungsten heating element melts an aluminium sample creating a vapour. The vacuum is sufficiently high to create a large mean free path, which prevent random walks. The probe is angled so that the apex of the probe is shadowed from the aluminium vapour. The result is that an even amount of aluminium is deposited on the probe whilst the apex is left uncoated, providing an aperture down which light can propagate.

The result of coating the near field probes can be seen in figure 3.5 where the spatial frequencies detected in preliminary data, of a photonic quasi-crystal structure, are presented. In (a) the data was collected using an uncoated probe, whereas, in (b), the data was collected using a probe that was coated in Aluminium using the aforementioned shadow evaporation technique. The spatial frequencies that are allowed to propagate according to the diffraction limit are those within the green circle, which is on both plots.

In figure 3.5, preliminary data from scanning a disordered scattering structure embedded in a silicon nitride planar waveguide demonstrates that both coated and uncoated near field probes are capable of retrieving image information beyond the diffrac-

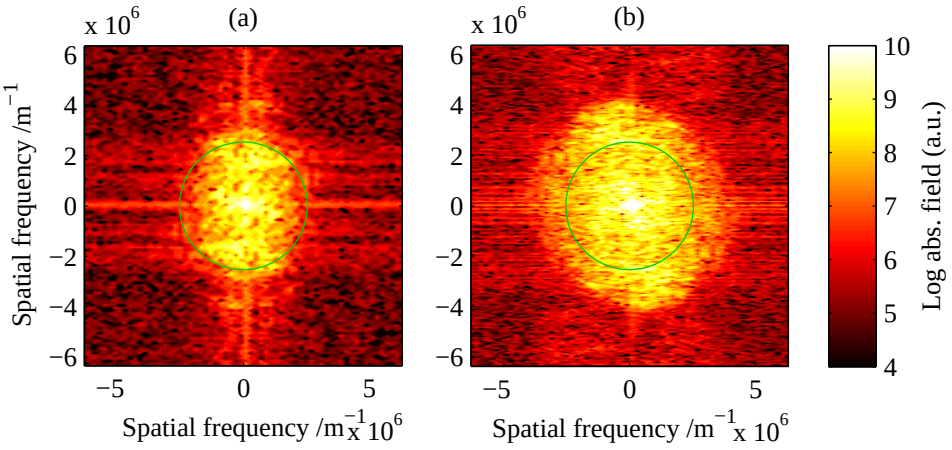

Figure 3.5: A log plot of the spatial frequency intensities detected for a sample with scatterers with spacing less than the diffraction limit for an uncoated probe (a) and a coated probe (b) at an illumination wavelength of $\lambda = 790$ nm. The green circle represents the spatial frequency cutoff of the Abbe limit $\lambda/2$. It can be seen that sub-wavelength imaging is possible with the uncoated probe, this can be seen at $y = \pm 4 \times 10^6$ m^{-1} in (a) where features beyond the diffraction limit are detected.

tion limit, since both plots reveal signals above noise outside the green circle. On both plots there are spatial frequencies outside the diffraction limit circle that create a series of vertical and horizontal lines just above the noise limit. These lines are artefacts and appear because of windowing of the data; the resulting response of windowing and applying a fast Fourier transform on the image produces artefact spatial frequencies. Different windowing choices of sample scans can enhance or diminish these artefacts and thus, even though they appear as give an indication of the highest spatial frequency present in the image at the extents, they are not useful for describing the resolution of the image.

The highest spatial frequencies, highlighted by the yellow regions, observed in both plots in figure 3.5 is just under 4×10^6 m^{-1}, which is the spatial frequency of standing wave interference effects for the illumination wavelength in a material with refractive index $n \approx 2$ (which is a good approximation for silicon nitride), suggesting that the features are caused by interferences of the illuminating source rather than topographical features. In (a), the uncoated probe was only reliable at detecting the 4×10^6 m^{-1} spatial frequencies along the y axis, which is most likely because it can only detect sub-wavelength resolution in the absence of scattered light. In which case, the spatial frequencies can be attributed to back reflected light in the guiding region of the waveguide where guided light dominates scattered light. These disordered scattering

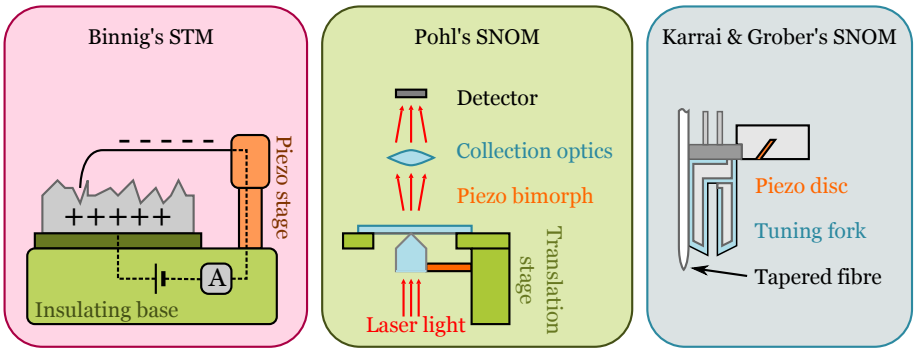

Figure 3.6: Digrams of the three main methods for near-field probe positioning used by Binnig; Pohl; and Karrai and Grober.

structures are revisited in chapter 5 (a diagram of the structure, from which these scans were taken, is presented in figure 5.4).

The ability to image beyond the diffraction limit using near field probes, both coated and uncoated, has been demonstrated. However, the method used to hold these probes in close proximity to the sample (within the evanescent field region has not been discussed). The following section deals with the method for maintaining a tip-sample distance at the nanometre scale.

3.3 SHEAR-FORCE FEEDBACK LOOPS

Nanopositioning with a feedback loop was the missing component that halted the practical realisation of Synge's idea of scanning a sub-wavelength aperture close to the surface of a sample. When Binnig presented his scanning tunnelling microscope, the technologies for nanopositioning and feedback loops became apparent. In 1984, Pohl *et al.* became the first group to adapt the STM technology to create a SNOM microscope[2]. This was done by using the conductive coating of the aperture (on a sharp quartz glass point), as a method of determining electrical contact between the probe and the sample. The construction of such a probe requires anisotropic etching of quartz in hydrofluoric acid, followed by a coating of chromium and gold, and then a formation of the aperture (traditionally by contact with a standard microscope slide); the aperture is, more recently, etched using a focussed ion-beam because of its high controllability.

Pohl's technique, similar to Binnig's original, requires that the sample under study is conductive. This is a problem since most materials that are transparent are dielectric. Fortunately, Khaled Karrai and Robert Grober developed a near-field positioning system that did not require a conducting sample[12]. Instead, their atomic-force feedback

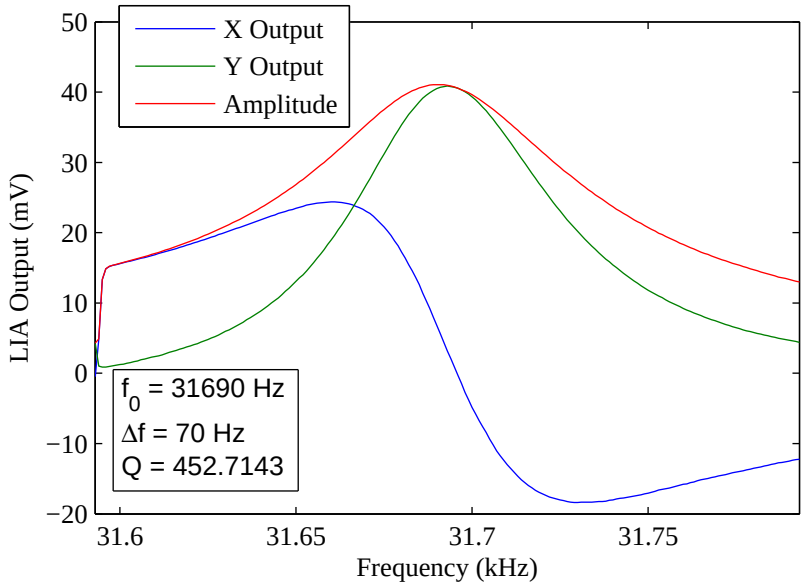

Figure 3.7: The resonance response of a piezo tuning fork with a near field probe mounted onto one of the prongs, detected using a lock-in detector. The reference phase was adjusted so that the X output (blue line) is zero at the resonant frequency. The Y output (green line), in this case, yields a large value at the resonance and is used as the input for the PID feedback loop.

loop monitored changes to the probe's resonance conditions while moving it closer to the sample surface. Measurement of the probe's resonance was achieved by mounting the probe on a piezo-electric tuning fork, dithering the setup and detecting the resonance response by monitoring the signal across the piezo-electric tuning fork.

The SNOM setup is dithered by connecting a signal generator to the piezo-electric disc mounted in the SNOM head. The electric signal generated by the tuning fork owing to the dithering is amplified and sent to a lock-in amplifier (LIA) which uses the driving signal from the signal generator as the reference signal. As the dithering frequency is raised, the amplitude response of the system detected by the LIA is recorded; the result of which can be seen in figure 3.7. In figure 3.7, the reference phase is changed to produce a small voltage at the X output (blue line) at resonance, thus producing a large voltage at the Y output (green). The Y output is then used as the input for the proportional integration differentiation (PID) controller, since its voltage changes the most for changes in resonance amplitude. The Y output is preferred over an electronic calculation of the amplitude to ensure the fastest electronic response to amplitude changes is sent to the PID controller.

The system is driven at a frequency just below resonance (usually 12 Hz below resonance), so that an increase in either the dampening factor or resonant frequency

would cause a reduction in amplitude of the system. This is critical for the feedback loop, since proximity to the surface must cause a predictable (in terms of increase or decrease) voltage change from the LIA so that the PID controller can respond accordingly. The rationale for expecting an increase in the resonant frequency upon close proximity to the sample is that it is effectively fixing the free end of the oscillations making the system more rigid. With the system oscillating below resonance, the PID controller is set to search for the position of the probe that gives a certain amplitude decrease.

The PID controller outputs the voltage that controls the height of the near field probe. Its output ranges from 0 to 10 V which, once connected to the probe's piezo controller, corresponds to fully retracted to fully extended respectively with a 20 μm range. The output of the PID controller depends on the input, setpoint, PID constants, and the time searching for the setpoint. If the difference between the input and setpoint (target) voltages is described as $\varepsilon(t) \equiv V_{\text{target}} - V_{\text{in}}(t)$ and is called the error signal, then the output voltage is described by

$$V_{\text{out}}(t) = P\left(\varepsilon(t) + I\int_{t_0}^{t} \mathrm{d}t \cdot \varepsilon(t) + D\frac{\mathrm{d}}{\mathrm{d}t}\varepsilon(t)\right), \tag{3.1}$$

where P, I, and D are the PID constants for the controller. It is not necessary to utilise the differentiation term in samples with small changes in topography since only small corrections are needed by the PID controller. By observing the error signal trace responding to step changes in height, the P and I constant can be tuned to give a quick response without heavy oscillations. The limiting factor in this response speed is the tuning fork's Q factor; with a bandwidth usually around 70 Hz, the time constant for amplitude changes is 14 ms. The LIA's time constant was set at a similar value to get sufficient accuracy *vs.* response time. Typical values used for the PID coefficients were $P = -2.3$, $I = 21\ \text{s}^{-1}$, and $D = 0$. However the constants were tuned by scanning a test grating and observing the response of the error signal after all near field probe replacements.

Most atomic-force microscopes (AFM) use a similar technique for measuring the topographical features of samples. While the resonance setup and probe can be tweaked to achieve atomic resolution[13], the resolution of a SNOM probe is related to the size of the probe's aperture and since this is typically 10s of nanometres in diameter, it is not usually necessary to have such precision for samples studied with a SNOM setup.

Using this PID feedback loop, changes in height encountered as the probe is scanned across the surface of a sample can result in quick adjustments to the probe's height.

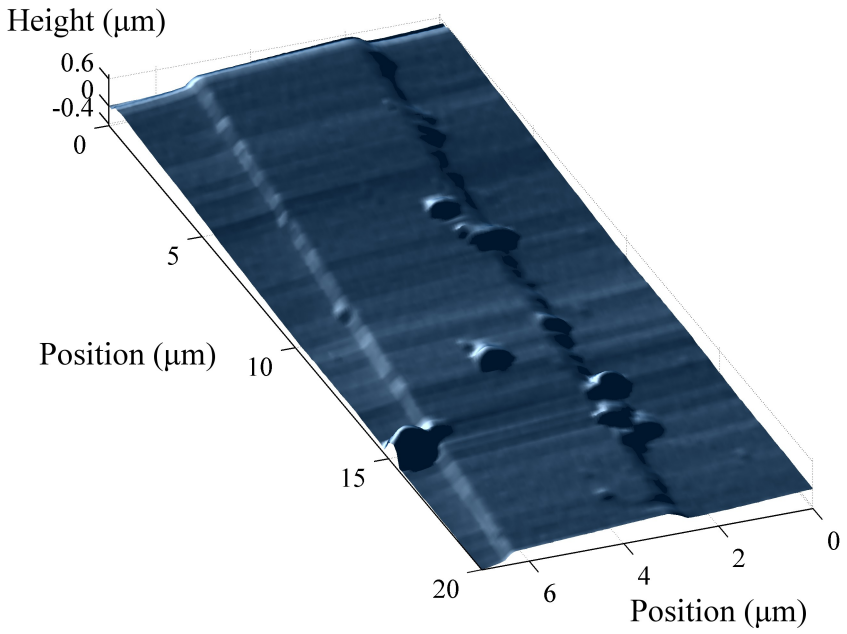

Figure 3.8: AFM topographic data taken whilst scanning a tantala rib-waveguide. Debris on the surface of the guide affect the propagation of modes; debris can be easily detected by analysing the topographic data.

This not only prevents damage to the near field probe, but can provide topographical information about the sample under study. This is most useful when searching for waveguides that have topographical features or explaining why the electric field is not as expected for a certain structure. Figure 3.8 is an AFM trace of a tantala ridge waveguide and demonstrates a good example of how the AFM can identify issues with intensity. The local intensity mapped for this structure the local electric field was attenuated greatly between 10 μm $< y <$ 15 μm. Upon examining the AFM trace, it was apparent that debris on the surface of the guide was responsible for the attenuation; the debris are the small pieces of dust on and around the ridge that runs down the y axis. This figure also demonstrates how the AFM trace can provide information about the location of the guiding area for a guide, with topographic features.

3.4 NANOPOSITIONING

The SNOM head was positioned using a Thorlabs 3-axis NanoMax translation stage, which consists of stepper motors for coarse control with 4 mm travel and piezoelectric actuators providing fine control with a range of 20 μm at a resolution of 5 nm. The stepper motors and the piezoelectric acuators for the x and y axes on the flexure

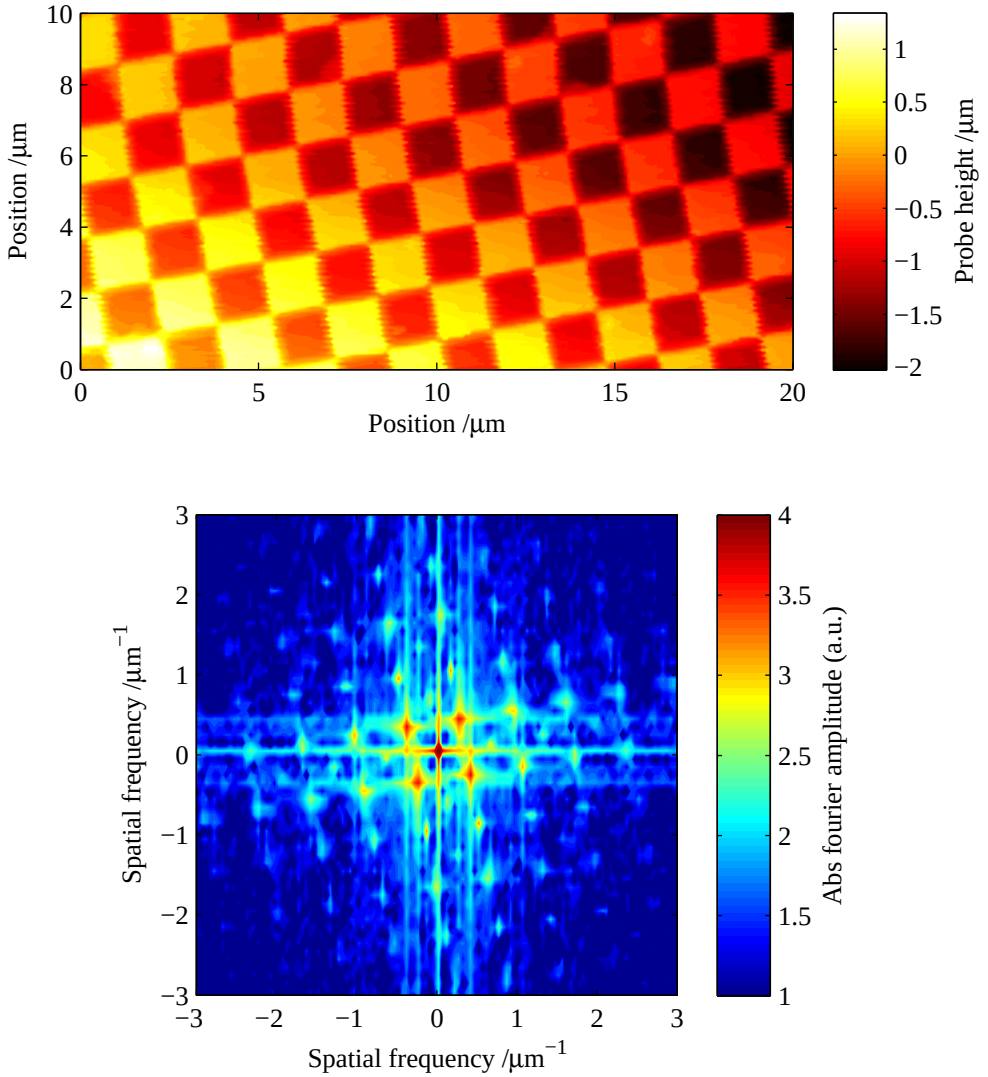

Figure 3.9: (top) An AFM scan of a TGX01 test grating. Edge-to-edge features are fabricated to be 3 μm and the changes in height are 1 μm. (bottom) Fourier analysis of the AFM data. Amplitude peak at $u = 0.325\ \mu\text{m}^{-1}$, which corresponds to a period of 3.08 μm.

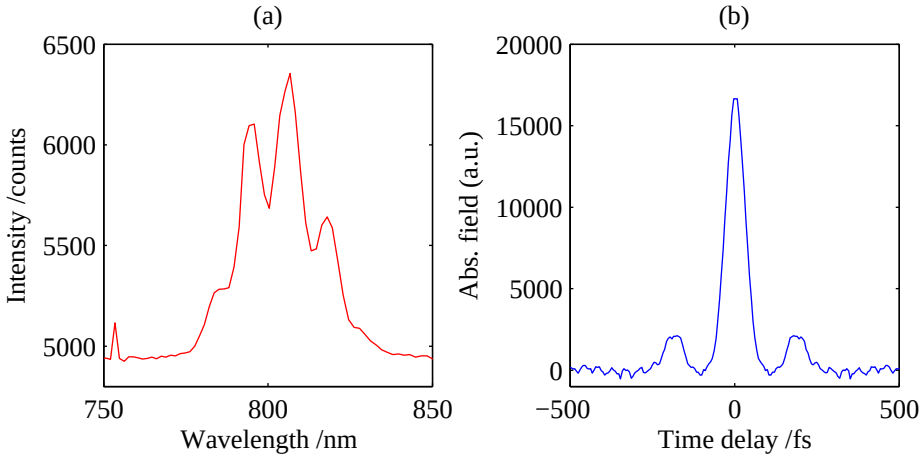

Figure 3.10: (a) A spectrum collected through the SNOM probe with interference caused by a signal time delay. (b) The FFT of the spectrum (the autocorrelation), showing the delays as satellite features away from the central feature.

stage were controlled using a software interface provided with the stepper motor and piezo controllers. The piezoelectric actuator for the z axis was controlled by an analogue piezo controller whose input signal was the output of the PID controller for rapid response to probe resonance conditions.

Piezo actuators are prone to hysteresis, this affects the ability to reliably measure distances when scanning in both directions while raster scanning. The voltage to displacement conversion by the piezo stage is also nonlinear. So that the piezo stage can be used to measure distances realiably, a strain-gauge loop was utilized for the x and y axis actuators. This feedback loop monitors the strain the piezo actuators exert on a strain sensor and use a PID feedback loop to determine the voltage to apply to achieve a target displacement. To test the reliability of the strain-gauge loop, a test grating with known dimensions was scanned. This scan of a TGX01 test grating is presented in figure 3.9 along with the Fourier transform of the height data to identify the periodicity of the test structure, which has a period of 3 μm. The spatial frequency plot has an amplitude peak at $u = 0.325\ \mu\text{m}^{-1}$, which corresponds to a period of 3.08 μm which is in good agreement with the specifications of the test grating, which declare a period of 3 μm. This demonstrates that the strain gauge is well calibrated.

3.5 Spectrally resolving SNOM

The detector used for collecting the data presented in this thesis was an Ocean Optics QE65k spectrometer. At the wavelengths under study, the spectrometer has a wave-

length resolution of 0.75 nm, which corresponds to a frequency resolution of 362 GHz. This enables the detection of time shifts of up to 1.3 picoseconds. The broadband light source used in the experiments had a bandwidth of 25 nm, which provide a resolution of approximately 40 fs for detecting time delay phenomena. Figure 3.10 shows a spectrum with interference features alongside its Fourier transform. The features in this spectrum are caused by a time delay in the signal detected and the time delays are easily seen in the Fourier transform plot which, from the Weiner-Khintchine theorem, is the autocorrelation of the signal. When collecting spectra to analyse in this way, it is important to ensure that the SNOM probe does not affect the spectrum collected. The spectrum can be normalised using software if this is the case and the inherent low powers involved with near field detection inhibits unwanted nonlinear interaction with the SNOM probe itself.

3.6 PRACTICAL CONSIDERATIONS

Maintaining a sample-probe distance of just a few nanometres makes the setup sensitive to environmental factors. More specifically, the setup is sensitive to thermal drifts, air currents, and vibrations. Air currents can vary the amplitude response of the feedback loop such that the PID controller, trying to maintain a set amplitude, can incorrectly interpret the amplitude response as the probe drifting away from the sample; this would cause the PID controller to crash the probe into the sample. To avoid air currents affecting the setup in this way, the SNOM was enclosed in a polystyrene box during scans.

Acoustic vibrations can also damage the near field probe as they can significantly affect the probe-sample separation at a speed to which the feedback loop cannot respond. To minimise vibration of the SNOM setup, the setup was built on a large optical breadboard which was placed on inflated wheelbarrow tyre inner tubes. For scans which were performed during high-risk exposure to vibrations, the entire setup was also placed on vibrationally isolated “floating” optical table.

Thermal drifts are usually relatively slow, such that the force-feedback loop can respond to subsequent changes in probe-sample distance much faster than thermal fluctuations can alter it. Large temperature variations, however, can alter the amplitude response of the force-feedback loop, which can cause system to crash the probe into the sample. Owing to this temperature stability dependence, long scans were timed to run overnight when the building’s temperature was most stable.

The preparation of the shear-force detection probe resonance condition and bring

the sample into and out of contact with the sample was all managed by software developed by the author. This software monitored and maintained the resonance condition for the feedback loop during scans so that scans for many hours could be performed even in changing environment conditions, without fear of critically damaging the near field probe. The software also managed the tessellation of SNOM scans, which extends the working area of the SNOM's 20 x 20 μm piezo-stage scanning range to, in principle, the 4 x 4 mm range of the stepper motors used.

3.7 CHAPTER CONCLUSION

The component parts of a SNOM system have been described and their role in enabling one to access the information contained within the evanescent field. The two most common methods for creating near-field probes was discussed along with a comparison of the spatial frequencies detected by a coated and uncoated probe. The shear-force feedback loop method of detecting proximity to the sample surface using a tuning fork was described.

The equipment used to position the near field probe was detailed and the test grating scan used to ensure the stage was calibrated was presented. The influence of environmental factors on the SNOM setup was also described, including the effects: air currents, temperature drifts, and vibrations. The software developed to utilise the full potential of the hardware used was also discussed.

REFERENCES

[1] E H Synge. XXXVIII. A suggested method for extending microscopic resolution into the ultra-microscopic region. *Philosophical Magazine Series 7*, 6(35):356–362, 1928.

[2] D W Pohl, W Denk, and M Lanz. Optical stethoscopy: image recording with resolution lambda/20. *Applied Physics Letters*, 44:651, 1984.

[3] Dennis R Turner. Etch procedure for optical fibers, 1984.

[4] G A C M Spierings. Wet chemical etching of silicate glasses in hydrofluoric acid based solutions. *Journal of Materials Science*, 28(23):6261–6273, December 1993.

[5] M. Ohtsu. Progress of high-resolution photon scanning tunneling microscopy due to a nanometric fiber probe. *Journal of Lightwave Technology*, 13(7):1200–1221, July 1995.

[6] Togar Pangaribuan, Shudong Jiang, and Motoichi Ohtsu. Highly controllable fabrication of fiber probe for photon scanning tunneling microscope. *Scanning*, 16(3):362–367, December 2006.

[7] Patrick Lambelet, Abdeljalil Sayah, Michael Pfeffer, Claude Philipona, and Fabienne Marquis-Weible. Chemically Etched Fiber Tips for Near-Field Optical Microscopy: A Process for Smoother Tips. *Applied Optics*, 37(31):7289, November 1998.

[8] Raoul StoÌĹckle, Christian Fokas, Volker Deckert, Renato Zenobi, Beate Sick, Bert Hecht, and Urs P Wild. High-quality near-field optical probes by tube etching. *Applied Physics Letters*, 75(2):160, 1999.

[9] Sutter Instruments. P-2000 Micropipette puller operation manual, 2008.

[10] G A Valaskovic, M Holton, and G H Morrison. Parameter control, characterization, and optimization in the fabrication of optical fiber near-field probes. *Applied Optics*, 34(7):1215, 1995.

[11] Patrik Hoffmann. Comparison of mechanically drawn and protection layer chemically etched optical fiber tips. *Ultramicroscopy*, 61(1-4):165–170, December 1995.

[12] Khaled Karraï and Robert D Grober. Piezo-electric tuning fork tip-sample distance control for near field optical microscopes. *Ultramicroscopy*, 61(1-4):197–205, December 1995.

[13] S Orisaka. The atomic resolution imaging of metallic Ag(111) surface by non-contact atomic force microscope. *Applied Surface Science*, 140(3-4):243–246, February 1999.

- CHAPTER 4 -

SPATIO-TEMPORAL DISCRIMINATION

The ability of SNOM/PSTM to obtain information beyond the diffraction limit has been discussed and demonstrated in the preceeding chapters. The focus of this chapter is on the temporal information one can obtain by using spectral information from a SNOM scan. This chapter firstly focusses on the motivations for exploring multimode waveguide phenomena and dispersion measurements, and then presents waveguide theory to explain the sources of the temporal delays in a waveguide; including one method used to model the guiding behaviour of the waveguides under study. Details on how a spectrally resolving SNOM can be used to identify different modes by their delays are then discussed.

4.1 MULTIMODE WAVEGUIDES

Waveguides provide the means to a create photonic lightwave circuit (PLC). PLCs are used in telecoms for sorting and processing certain information carried by infrared light. However, these systems are limited to single-mode operation and multimode components limit the performance of such PLCs. With the ability to reliably influence the propagation through multimode devices, a route to extending the performance of existing PLCs is realised. Such extension of a single mode system has already been demonstrated[1] in optical frequency mixers used for signal processing. Using asymmetric Y junctions, TM_{00} and TM_{10} were sorted after frequency mixing where it is not trivial to separate the input from the output. When operated in reverse, the Y junction provided a method of converting a single mode input into a higher order mode.

The ability to measure or predict the multimodal behaviour of PLCs is essential for developing practical multimode devices. Different propagating modes, as shall be presented later in this chapter, have different dispersion curves. This results spectral

features on the spectra collected after propagating through a multimode device. Analysis of these spectral features can identify the group delay between different modes[2]. The ability of SNOM to take spectra using a non-destructive method has enabled the measurement of the local group delay inside a waveguide by analysing spectral interferences along and across a waveguide[3–5].

Other research has demonstrated an ability to measure absolute propagation constants of single mode devices by analysis of the spatial frequencies present in interference fringes visible in SNOM scans of photonic crystal waveguides[6, 7]. Such a wealth of information available about a waveguide highlights suitability of SNOM to study integrated optics phenomena.

4.2 GROUP DELAYS IN WAVEGUIDES

To understand the causes of group delays in a multimode waveguide, the guidance condition for a waveguide must be solved. This can be done using a variety of methods including finite element modelling (FEM) and film mode matching (FIMM). Since the actual values are not important to investigate the source of group delays and how they can be measured, we can use a method that uses large approximation. One such approximate method is the effective index method. In this method, the guidance condition of the waveguide is determined by considering the guidance condition of four planar waveguide approximations based on the waveguide geometry.

The waveguides under study were tantalum pentoxide (tantala) ridge waveguides; application of the effective index method will be demonstrated on this type of waveguide.

4.2.1 EFFECTIVE INDEX METHOD

The effective index method (EIM) enables one to create approximate expressions for the guiding characteristics of waveguide structures by decomposing a waveguide into a set of 1 dimensional refractive index based on its geometry. This simplifies the mathematical treatment, as 1 dimensional refractive index profiles can be treated as a planar waveguide geometry. The EIM is restricted to finding only transverse electric (TE) or transverse magnetic (TM) modes, partial TE/TM modes cannot be found using this method as it uses the scalar wave equation to solve the guidance characteristics. The tantala waveguides studied in this work, had no partial TE/TM modes when analysed using commercial FIMM software and so the EIM is suitable for obtaining suitable

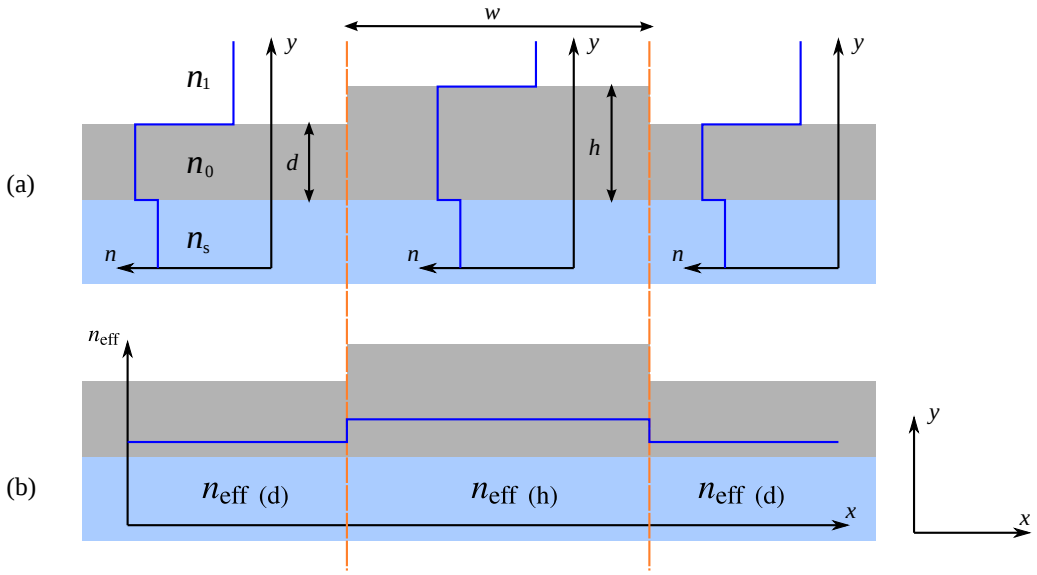

Figure 4.1: The application of the effective index method to a generic ridge waveguide is shown here. First, the structure is broken down into three sections to produce three planar waveguide structures to use for the first stage of the calculation, demonstrated in (a). Using the effective indices from these three planar waveguides, a fourth planar waveguide is constructed, demonstrated in (b). The solution of this final planar waveguide is an approximation for the guiding solution of the waveguide.

expressions for the expected guiding properties of the waveguides under study.

The first stage of the EIM involves breaking down the waveguide into three planar waveguides. This is illustrated in figure 4.1(a), where three vertical planar waveguids are constructed. For this waveguide geometry, the vertical direction must be separated first since there are no refractive index changes in the horizontal direction for the three sections of the waveguide as can be seen in figure 4.1. For each of the planar waveguides structures, an "effective index" is determined based on the geometry of the equivalent planar layer. For a simple case, the outer planar structures should be single mode for the wavelength used (the central region can be multimode, however this is not essential). With the effective indices from the three planar structures, a fourth planar waveguide can be created, this is illustrated in figure 4.1(b). The guiding properties from this fourth $n_{\text{eff}}(x)$ planar waveguide yields the approximate guiding properties for the waveguide under study.

4.2.2 The guidance condition

The guidance condition is the condition that the electric and magnetic fields must satisfy to be guided down the waveguide. As shall be shown, a discrete number of waveg-

uide modes travel down the guide whose total number and spatial profile depend on the geometry of the waveguide. Since the EIM method is used to determine the approximate guiding properties of the waveguides under study, the relatively simple case of solving planar guiding geometries can be used to determine the guidance condition of more complex structures. To find the guidance condition of a planar waveguide structure, fundamental electrodynamics can be used. The relationship between electric and magnetic fields can be described by recalling Maxwell's equations

$$\nabla \times \mathbf{E} = -\mu_0 \frac{\partial}{\partial t}\mathbf{H}, \tag{4.1}$$

$$\nabla \times \mathbf{H} = -\varepsilon_0 n^2 \frac{\partial}{\partial t}\mathbf{E}, \tag{4.2}$$

where ω is the angular frequency of the electric field and β is the propagation constant for the electric field. Assuming that the profile of the waveguide does not vary significantly along the propagation axis, the propagation axis (typically z) can be separated from the solution. This will yield solutions of the following form

$$\mathbf{E}(x,y,z,\omega) = \mathbf{E}(x,y)\exp\left[\mathrm{i}(\omega t - \beta z)\right] \tag{4.3}$$

$$\mathbf{H}(x,y,z,\omega) = \mathbf{H}(x,y)\exp\left[\mathrm{i}(\omega t - \beta z)\right], \tag{4.4}$$

which can be substitued into equations 4.1 and 4.2 to obtain the relationship between the electric and magnetic fields across (xy plane) and down the waveguide

$$\begin{cases} \dfrac{\partial}{\partial y}E_z + \mathrm{i}\beta E_y = -\mathrm{i}\omega\mu_0 H_x \\ \mathrm{i}\beta E_x - \dfrac{\partial}{\partial x}E_z = -\mathrm{i}\omega\mu_0 H_y \\ \dfrac{\partial}{\partial x}E_y - \dfrac{\partial}{\partial y}E_x = \mathrm{i}\omega\mu_0 H_z \end{cases} \qquad \begin{cases} \dfrac{\partial}{\partial y}H_z + \mathrm{i}\beta H_y = -\mathrm{i}\omega\varepsilon_0 n^2 E_x \\ \mathrm{i}\beta H_x - \dfrac{\partial}{\partial x}H_z = -\mathrm{i}\omega\varepsilon_0 n^2 E_y \\ \dfrac{\partial}{\partial x}H_y - \dfrac{\partial}{\partial y}H_x = \mathrm{i}\omega\varepsilon_0 n^2 E_z \end{cases} \tag{4.5}$$

where the $\mathbf{E}$ and $\mathbf{H}$ vectors have been separated into their Cartesian components. Since planar waveguide structures are being considered, electric field variation along one of the axis can be assumed to be zero; a solution along a given axis (x axis in this example) will be constant over an inifinite distance. Thus $\frac{\partial}{\partial x}\mathbf{E} = 0$ & $\frac{\partial}{\partial x}\mathbf{H} = 0$. Using this restriction, we can take the equations from 4.5 and obtain an equation that describes the variation of E_x with the y axis

$$\frac{\partial^2}{\partial y^2}E_x + (n^2k_0^2 - \beta^2)E_x = 0, \qquad E_y = E_z = H_x = 0. \tag{4.6}$$

This equation is one of two polarisation states that the waveguide can support. Since the electric field has a non-zero value in only the x axis in equation 4.6, it describes the variation of the transverse electric (TE) mode. A similar equation exists for the transverse magnetic (TM) mode, with the distinction that the y-dependant refractive index n is present:

$$\frac{\partial}{\partial y}\frac{1}{n^2(y)}\frac{\partial}{\partial y}H_x + \left(k_0^2 - \frac{\beta^2}{n^2}\right)H_x = 0, \qquad E_x = H_y = H_z = 0. \tag{4.7}$$

The fact that the TE and TM modes of the waveguide are described by different equations is also the reason they have different propagation constants for their respective modes. The propagation of these two polarisations is another source of inter-modal delay in a waveguide (including a single mode waveguide).

By recognising that the boundary conditions for a planar waveguide are essentially two reflecting surfaces above and below the core region, a transverse standing wave solution can be expected in the core of the planar waveguide structures, with attenuating fields in the cladding regions. This results in a solution for the electric field inside the planar waveguide that takes the following form

$$E_x = A_0 \begin{cases} \exp\left[-\alpha_1 y\right] & \left(y > \frac{d}{2}, \frac{h}{2}\right) \\ \cos\left[\kappa y + \phi\right] & \left(-\frac{d}{2}, -\frac{h}{2} <= y <= \frac{d}{2}, \frac{h}{2}\right) \\ \exp\left[\alpha_2 y\right] & \left(y < -\frac{d}{2}, -\frac{h}{2}\right), \end{cases} \tag{4.8}$$

where α_1 & α_2 represent the attenuation coefficients, κ represents the wavenumber of the standing wave core solution, and a phase factor to allow asymmetric waveguide solutions. These equations, when substituted into equation 4.6, show the relationship between the attenuation coefficients and the transverse standing-wave wavenumber with the propagation constant and the wavelength (k_0)

$$\kappa = \sqrt{n_0^2 k_0^2 - \beta^2} \qquad \alpha_1 = \sqrt{\beta^2 - n_1^2 k_0^2} \qquad \alpha_2 = \sqrt{\beta^2 - n_s^2 k_0^2}. \tag{4.9}$$

For a real solution, the magnetic field must be continuous across the refractive index boundaries. Expressions for the magnetic field can be obtained by using one of the

equations from 4.5 with the planar waveguide approximation $\left(\frac{\partial}{\partial x}\mathbf{E}=0\right)$

$$\mu_0 \omega H_z = \mathrm{i}\frac{\partial}{\partial y}E_x, \tag{4.10}$$

resulting in the following equations for the magnetic field

$$H_z = A_0 \frac{-\mathrm{i}}{\mu_0 \omega} \begin{cases} \alpha_1 \exp\left[-\alpha_1 y\right] & \left(y > \frac{d}{2}, \frac{h}{2}\right) \\ \kappa \sin\left[\kappa y + \phi\right] & \left(-\frac{d}{2}, -\frac{h}{2} <= y <= \frac{d}{2}, \frac{h}{2}\right) \\ -\alpha_2 \exp\left[\alpha_2 y\right] & \left(y < -\frac{d}{2}, -\frac{h}{2}\right). \end{cases} \tag{4.11}$$

For the electric field to be continuous, equation 4.8 dictates that $\pm\exp[\mp\alpha y] = \cos[\kappa y + \phi]$. This gives the following restrictions on which electric field solutions may propagate down the waveguide

$$\kappa\frac{h}{2} + \phi + m\pi = \arctan\left(\frac{\alpha_1}{\kappa}\right) \tag{4.12}$$

$$\kappa\frac{h}{2} - \phi + n\pi = \arctan\left(\frac{\alpha_2}{\kappa}\right), \tag{4.13}$$

where the integers m and n have been introduced to explicitly include the periodicity of the tan function. These boundary conditions combine to create the **guidance condition** of the respective planar waveguide structure

$$\kappa h - \arctan\left(\frac{\alpha_1}{\kappa}\right) - \arctan\left(\frac{\alpha_2}{\kappa}\right) = m\pi \tag{4.14}$$

$$2\phi - \arctan\left(\frac{\alpha_1}{\kappa}\right) + \arctan\left(\frac{\alpha_2}{\kappa}\right) = m\pi, \tag{4.15}$$

where the integers have been merged to become the mode number m of the waveguide. The discrete standing-wave solutions form a discrete set of modes that the waveguide can support. These equations demonstrate that only certain values of α_1, α_2, and κ can exist inside the waveguide; these are the values that determine the spatial profiles of the guided modes and three such spatial profiles are plotted in figure 4.2. In this figure, it can be seen that the intensity profile can identify the mode; this will be considered later when identifying the modes responsible for group delays in the waveguide.

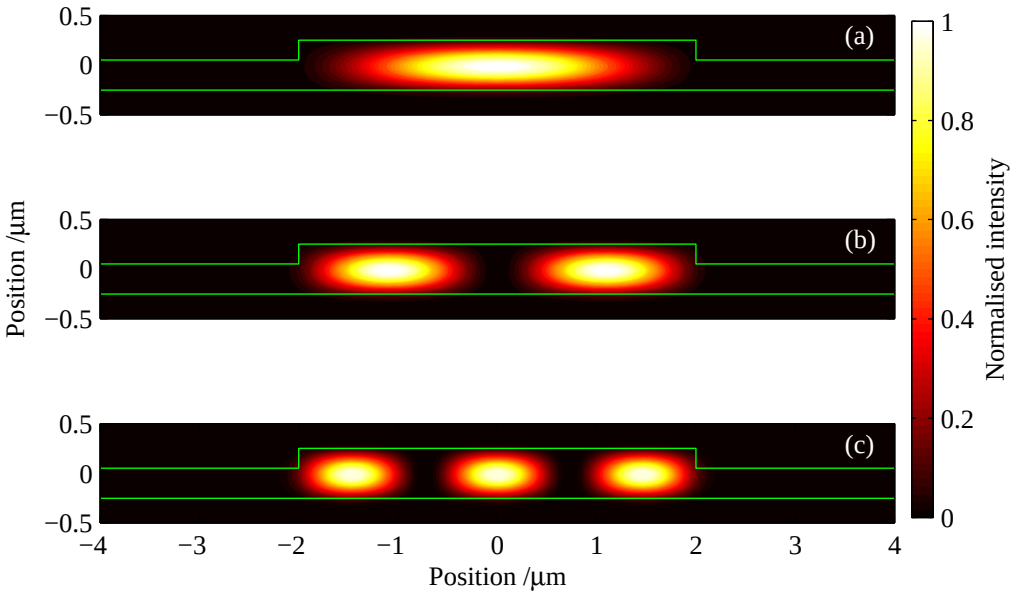

Figure 4.2: The intensity map for the first three guided TE modes for the tantala ridge waveguide structure have been plotted for a wavelength which allows multiple modes to be supported by a waveguide of such dimensions. (a) is the fundamental mode, (b) is the first-order mode and (c) is the second order mode.

4.2.3 WAVEGUIDE MODES AND GROUP DELAYS

The conditions required for waveguiding have now been discussed, it is now necessary to discuss the implications of them. Each mode travels down the waveguide with its own effective index and this results in inter-modal dispersion. The delays that accumulate between each mode can, as will be discussed, result in spectral features that enable one to directly decompose a waveguide's mode structure by taking localised spectra.

The presence of the free-space wavenumber k_0 with the solution wavenumber and amplitude coefficients (equation 4.9) mean that the solution to the guidance condition of a waveguide (equations 4.14 and 4.15) is **wavelength dependant** even in the absence of material dispersion. This is shown in figure 4.3 where two plots present the solution to the guidance condition with and without material dispersion included. The inclusion of material dispersion slightly perturbs the results that are obtained without. This suggests that the main factor in determining a waveguide's guiding characteristics is its geometry. Because of this, it is evident that an experimental method of measuring waveguide dispersion phenomena is useful for investigating waveguide geometries as a practical solution for multimode photonic devices is sought.

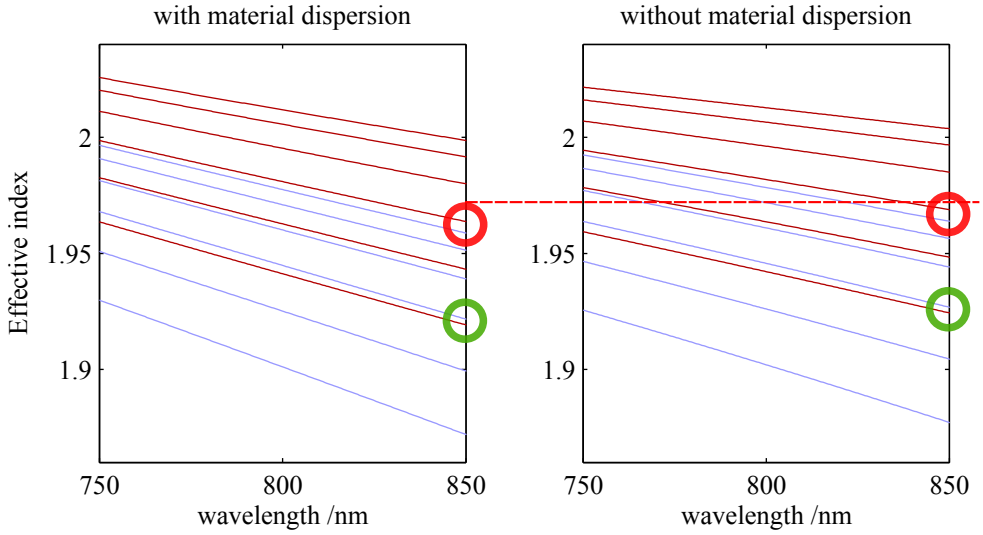

Figure 4.3: The core effective indices (TE modes: red lines, TM modes: blue lines) as solved using the EIM with and without including material dispersion in the model. This shows that, even without material dispersion, the modes have frequency dependence. A green and red circle highlights identical groups of modes in each plot, identifying the role of material dispersion on the modes. The inclusion of material dispersion in the model manifests as a small offset to the modes' effective indices.

4.3 SPECTRAL INTERFERENCE

The first section in this chapter discussed the sources of delays in the waveguide. This section will describe how SNOM can be used to measure these delays and how this method can lead to measurements on the individual modes propagating inside the waveguide.

The ability to take direct measurements on the guiding properties of multimode photonic lightwave circuits, is the likely route to extending the bandwidth of current single mode systems. The spectral region used in telecommunications has received much attention, thus the properties and production of materials for this spectral region are well known. To extend the bandwidth of devices already in use for telecoms, it would be desirable to make current devices use multimode effects; this would reduce the need to study new sources of light and would be compatible with existing telecoms devices.

4.3.1 BROADBAND PROPAGATION

The first section dealt with the physics of mode propagation for a single frequency; but propagation, as discussed earlier, depends on the frequency of light. By considering the spectral variation of the propagation constant β, the effects of temporal delays can

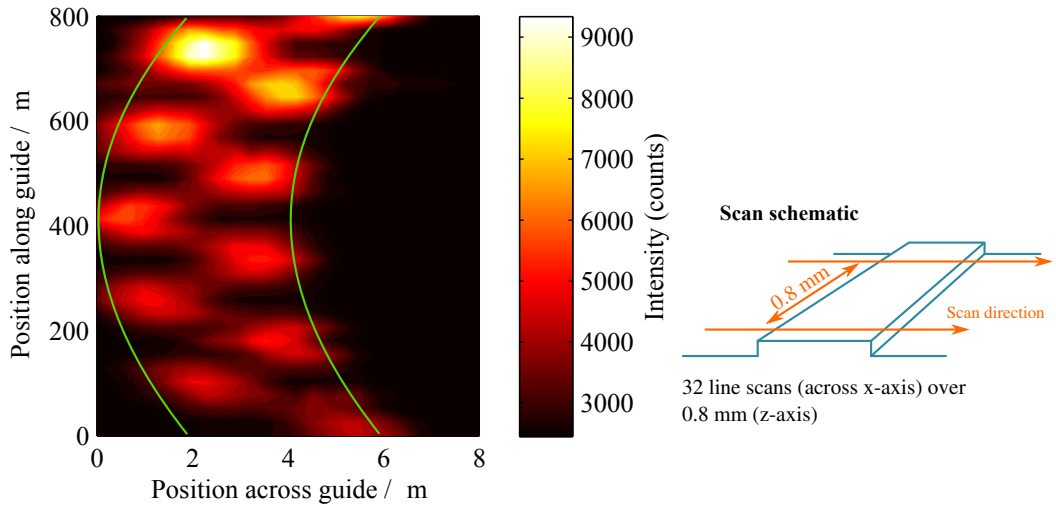

Figure 4.4: Experimental data of the intensity map of a narrow wavelength range propagating down a tantala ridge waveguide with the input coupling optimized for the first order mode propagation. The green lines represent the guiding region of the waveguide. The beat length of this interference is approximately 163 μm which corresponds to a refractive index difference of about $\Delta n = 0.005$. The apparent bend is a 2 μm drift over 800 μm and could be a thermal drift over the scan or dimensions within the acceptable fabrication precision.

be determined.

The propagation constant of a mode j can be written as a Taylor expansion around a central frequency ω_0 such that

$$\beta_j(\omega) = n_j(\omega)k_0 = \beta_j + \beta_j'\Delta\omega + \frac{1}{2}\beta_j''\Delta\omega^2 + \cdots, \tag{4.16}$$

where $\Delta\omega = \omega - \omega_0$. The first order Taylor expansion term has physical significance since β' is the inverse of the group velocity v_g which is the speed at which signals propagate down the waveguide. It has been discussed earlier that a waveguide supports discrete modes with different spatial profiles that have different propagation constants; further, these propagation constants have their own spectral response too as visible in figure 4.5. A simple two-mode TE waveguide will now be considered to investigate how inter-modal dispersion affects the spectral output. Such a two-mode system can be described by the following

$$\tilde{E}(\omega,x,z) = A(\omega)\sum_{j=0,1} m_j M_j(x)\exp\left[\mathrm{i}\beta_j\, z + \mathrm{i}\beta_j'\Delta\omega\, z\right], \tag{4.17}$$

where m_j and M_j are the j^{th} mode's amplitude coefficient and normalised mode profile

respectively. Measuring electric field requires an interferometric setup, and has been demonstrated on SNOM setups [8]. However, most spectrometers measure spectral intensity, thus the spectral intensity of this propagation is of greater interest and can be determined by considering the Hermitian inner product of the electric field

$$\tilde{I}(\omega,z) = m_0^2\tilde{A}^2\left(M_0^2 + r^2M_1^2 + 2rM_0M_1\,\cos[\Delta\beta\, z + \Delta\beta'\Delta\omega\, z]\right), \tag{4.18}$$

where $\Delta\beta = \beta_1 - \beta_0$ and a ratio of the mode amplitude coefficients has been defined $r = m_1/m_0$. The cosine in equation in 4.18 shows that spectral cosine fringes will become evident in the local spectra as a result of two modes travelling with different group indices ($v_g = \beta'^{-1}$). Equation 4.18 predicts the existence of mode beating along the propagation length from the first term of the cosine function. This is experimentally observed in figure 4.4 where the coupling was deliberately optimized to guide a large fraction of the input power in the first order mode. The resulting SNOM scan over 800 μm shows an alternating spatial beating pattern with a beat length of approximately 163 μm which corresponds to a refractive index difference of

$$\Delta n = \frac{\lambda}{\Delta z} = \frac{780\text{ nm}}{163\ \mu\text{m}} = 0.0048, \tag{4.19}$$

where Δz is the beat length of the interference. This result is in good agreement with the refractive index difference between the two corresponding TE modes predicted from the numerical solution of $\Delta n = 0.006$ presented in figure 4.5. This also demonstrates the ability of the SNOM setup to use the piezo actuators and stepper drivers to obtain scans over large scan areas.

The relationship between the first order propagation constant term β' (group index term) and the time delay between the modes can the following

$$\Delta t = \frac{z}{v_0} - \frac{z}{v_1} = \frac{z}{c}\Delta n_g \tag{4.20}$$

$$= z\,\Delta\beta'. \tag{4.21}$$

Time delays, as their name suggests, are better observed in the time domain. Equation 4.18 can be converted to the time domain by using a Fourier transform. Since the equation represents a power spectrum, the Fourier transform will yield the autocorrelation as dictated by the Weiner-Khintchine theorem

$$I(t,z) = (M_0^2 + r^2M_1^2)\,A^2(t) + rM_0M_1 \cdot \mathrm{e}^{\pm \mathrm{i}\Delta\beta z}A^2(t \pm \Delta\beta' z), \tag{4.22}$$

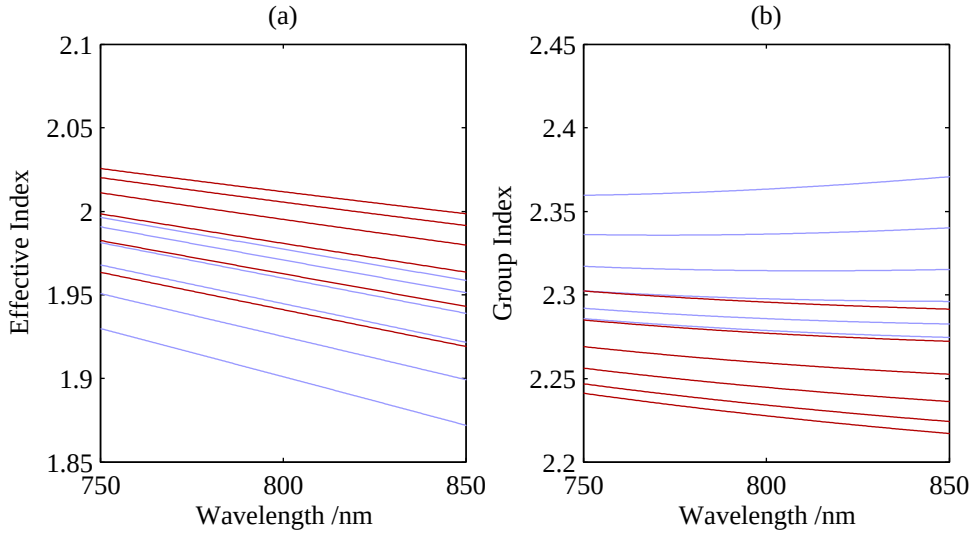

Figure 4.5: (a) The effective indices of the propagating modes inside the waveguide. The red and blue represent TE and TM solutions respectively. The lowest order mode has the greatest effective index, with higher order modes decreasing in effective index. (b) Simlar to the effective index, this plot represent the group index of each mode. This is the index that will determine how pulses (or spectra) of light will propagate down the waveguide.

where the mode amplitude coefficient for the fundamental mode m_0 has been combined with the spectrum envelope function $\tilde{A}(\omega)$ for clarity. This shows how the autocorrelation displays time delays as displaced features from the central maximum with a time delay equal to $\Delta t = \Delta\beta' z$; clearly easier to measure than counting spectral fringes. Equation 4.22 also demonstrates the effects of phase velocity dispersion between modes on the autocorrelation. It shows that a phase angle rotates as the light travels along the waveguide according to the refractive index difference between the modes.

The effects of inter-modal dispersion on the spectrum of a broadband source of light has been discussed, along with a method of determining the time delay between two corresponding modes using Fourier analysis. Modes also have spatial profiles inside the guides and SNOM enables localised spectra to be obtained. Using localised spectra, mode profiles can be observed by discriminating the waveguide mode profile temporally.

4.3.2 Temporal discrimination

In the previous section, the spectral features due to inter-modal dispersion was discussed with little mention of the modes' spatial profiles. Spectral fringes only occur

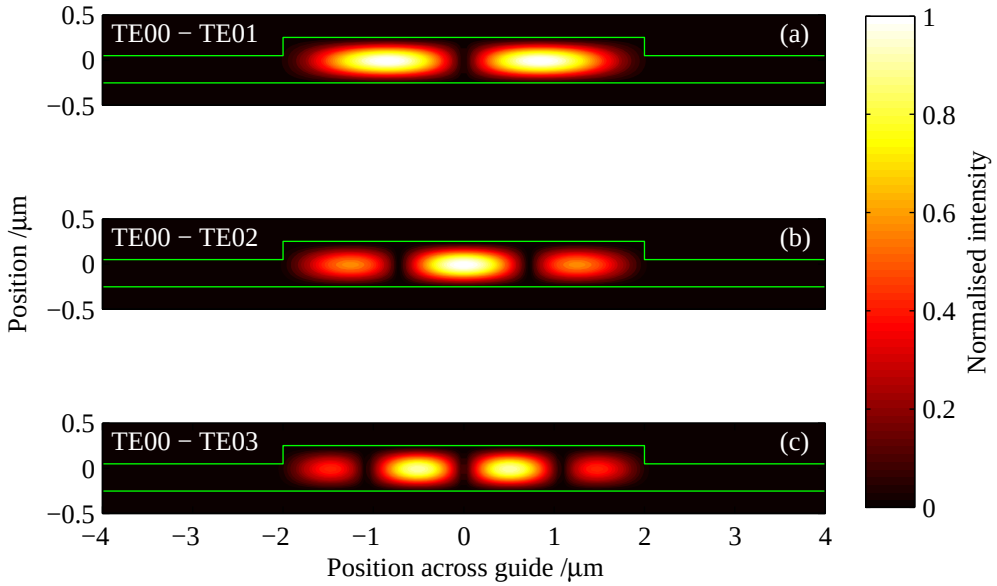

Figure 4.6: Numerical simulation of the intensity spatial overlap of various modes with the fundamental (indicated at the top left of each plot). Interference features caused by overlap with the fundamental mode are expected to be particularly prominent, owing to the fundamental mode's typically high relative power. Any features caused by the interference of modes in the waveguide will have a spatial dependence of the intensity overlap between the relevant modes across the waveguide.

between two modes in areas where their respective intensity spatial profiles overlap. This was shown in equation 4.22, where autocorrelation features away from the central max only occur if the M_0M_1 term is non-zero; the first-order mode profile is zero at the guide centre, so a delay feature would not be expected at the centre of the waveguide for any delay incurred with the first order mode. This is best understood by considering figure 4.6 where the absolute power overlap between different modes is plotted. At the top of figure 4.6 plot (a) shows the intensity overlap between the fundamental and first order modes and the absence of overlap at the centre of the guide is shown. The overlap between two higher order modes with the fundamental are also presented in figure 4.6 where one can observe that the number of intensity lobes can be used to identify the modes.

The spatial overlaps of higher order modes are presented in figure 4.7 where identifying the spatial overlap of higher order modes becomes more challenging with the increased number of lobes. Since the autocorrelation presents a field, features in close proximity (which occur in waveguides from modes with similar group delay differences) can interfere on the resulting autocorrelation plot. This is another factor that

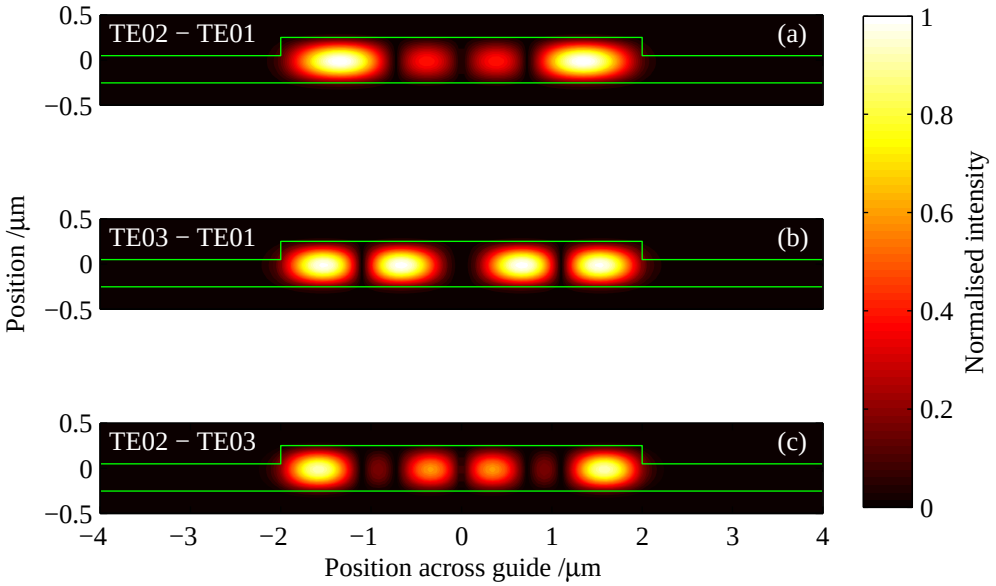

Figure 4.7: Numerical simulation of the intensity spatial overlap of various modes (indicated at the top left of each plot). Any features caused by the interference of modes in the waveguide will have a spatial dependence of the intensity overlap between the relevant modes across the waveguide.

can make analysis of waveguide with a large number of modes complicated. To avoid detecting modes with similar group delay differences, the coupled light was polarised to excite only TE modes, as their TM counterparts are expected to produce similar group delay differences. Another way to avoid interference between similar group delays would be to use a spectrally broad source. Using more bandwidth of light would increase the temporal resolution of the system; similar group delays could then be resolved from each other, rather than overlap and interfere.

The technique of plotting the spatial dependence of spectral interference has been applied to the output of fibres to analyse the modal content of fibres[9] where the term spatio-spectral (S^2) imaging was coined. An earlier work mentions that this spatial dependence of spectral interference could by used to separate modes with known spatial profiles[1]. This techniques has also been called cross-correlated (C^2) imaging[10]. The ability of SNOM to make non-destructive measurements and its ability to measure localised spectra was also discussed in previous SNOM work where the aim was to find a location with the greatest intensity overlap between all modes[11].

A theoretical prediction of the autocorrelation (x axis) against lateral position across the waveguide (y axis) can be seen in figure 4.8 for the waveguide under study. There is

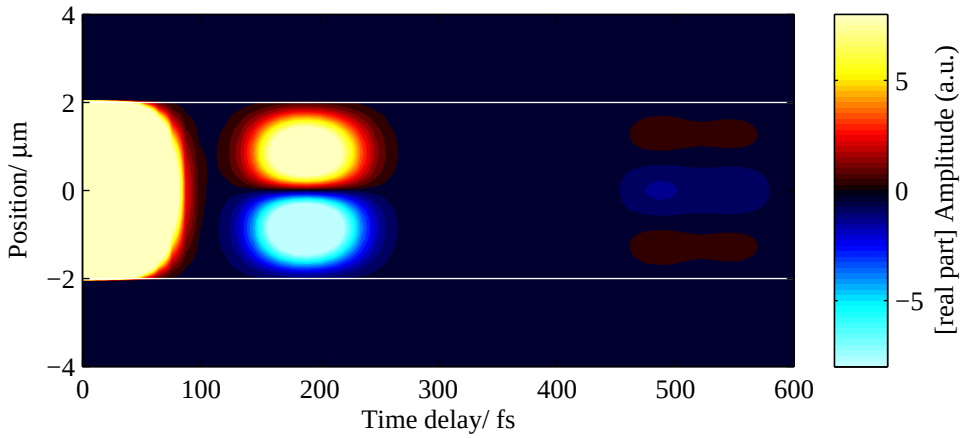

Figure 4.8: Numerical simulation of the theoretical autocorrelation vs. position of a tantala ridge waveguide for a TE illumination wavelength of 790 nm with 25 nm bandwidth using the EIM. The delays between the fundamental, first, and second order modes can be clearly seen on the autocorrelation. The phase profiles of the higher order modes are also distinguishable. This is because the fundamental mode's field does not go negative; thus, along with for a typical coupling it is usually the mode with the greatest power, it can be used as a reference mode inside the guide.

an autocorrelation feature resulting from a delay between fundamental and first-order modes at $t \approx 180$ fs; this can be identified by its spatial profile. The group delay from the first-order and fundamental modes is also visible at time delay $t \simeq 510$ fs, again identifiable by its spatial dependence. This plot is actually at a unique position where the phase angle introduced by the first Taylor term of the group delay difference has little, or no, imaginary part. The advantage of this position, is that the real part of the autocorrelation can be plotted to provide insight into the relative phase between mode lobes. In figure 4.8, the different colours represent positive (red) and negative (blue) field values. The fundamental mode has only one lobe and, thus, no polarity differences across its profile. This means that, provided it can be assumed that the fundamental mode is the mode with the greatest intensity in the waveguide, the positive-negative switches are caused by the higher order modes.

Figure 4.9 presents two plots from experimental data, showing how collecting spectra at different locations affects the autocorrelation measured. By changing which half of the waveguide (laterally speaking) to scan, the autocorrelation presents oppositely signed fields. This corresponds to a π phase shift in the spectra interference features which are due to the relative field overlap caused by the first-order mode. Using the fundamental mode as a reference, the spatial profiles of the higher order modes (overlapped with the fundamental profile) become visible in the autocorrelation at specified

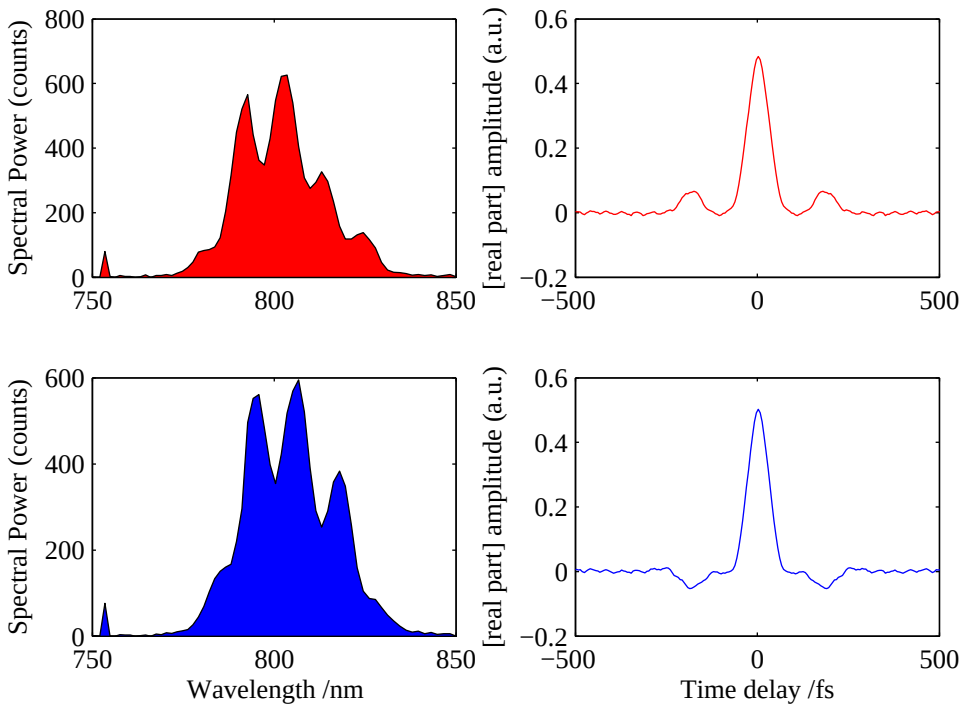

Figure 4.9: (left) Two spectra collected while scanning the the tantala waveguide excited by 790 nm with a bandwidth of $\pm$25 nm (coupling optimised to excite higher order modes with fundamental) at different sides from the centre of the guide. (Right) the Fourier transform of the spectrum, which by the Weiner-Khinchtine theorem is the autocorrelation of the signal.

time delays (in this particular case 180 fs), usually with an arbitrary phase angle attributed to their linear group delay difference which varies as a function of propagation distance down the waveguide. These time delays are simply the delay, at the particular location of where the spectra was collected, from the point of coupling of the waveguide modes. This enables one to make measurements on different modes locally in a waveguide, a highly desirable ability for characterising multimode photonic lightwave circuits for their use, or investigating their potential use, as multimode devices. In summary, this temporal discrimination technique separates a mode (and its spatial profile) from the incoherent sum of mode intensities by discriminating modes by the time delay they accrue with the fundamental mode.

Figure 4.10 shows the autocorrelation of spectra as a function of position across the waveguide collected by the SNOM system by scanning a probe in the near-field region across a Ta_2O_5 (tantala) ridge waveguide at approximately 8 mm from the point of coupling. The delay that has accumulated between the fundamental and first-order modes whilst propagating this distance can be seen clearly at a delay near 180 fs.

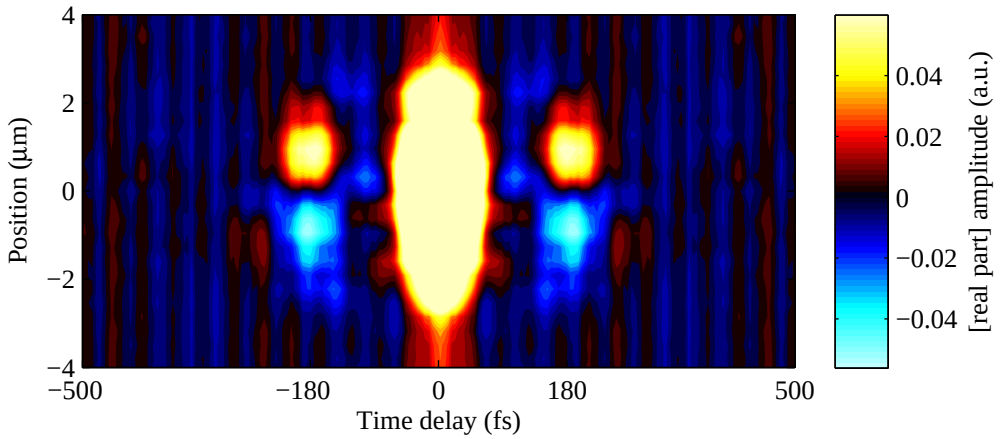

Figure 4.10: The autocorrelation of the local spectra collected by the SNOM of light propagating in the waveguide as a function of position across the guide. The delay between the fundamental and first order modes can be seen clearly at approximately 180 fs. At this delay, the mode overlap is observed. One can extract, since the overlap is with the fundamental mode, the first order mode's phase profile.

The resulting feature at this delay is in good agreement with the theory discussed, confirming that the delay can be attributed to the identified modes. The out-of-phase lobe feature, visible across the *y* axis in the figure, is expected from a first-order mode and also confirms that the identified modes are responsible for this particular group delay. As discussed previously, the phase angle between the lobes of the first-order mode and the fundamental mode changes as a function of position down the guide based on their **phase velocity** difference. It is by chance, that the spectra collected at the location of the scan resulted in phase angles of 0 or π, causing the real part of the autocorrelation to show the phase profile of the mode without any phase angle modification.

Unfortunately the delay between the fundamental and second-order cannot be seen in figure 4.10. This is owing to the limited signal-to-noise ratio available from the scan. Features from higher-order mode overlaps are predicted to exist but, owing to time limit of scans, was not attainable in the experimental setup used to collect this data. Further to interrogating the spectral interference across the waveguide profile, the group velocity difference between the modes can be directly observed by taking these autocorrelation measurements at different locations along the waveguide; this has been done previously[3]. If the propagation characteristics of the fundamental mode are known, or can be easily determined, then this method provides a way of obtaining the absolute propagation constants for each mode in the waveguide. This, combined with its non-destructive measurement nature, makes PSTM a practical route

for direct characterisation of multimode devices.

4.3.3 DIRECT MODE AMPLITUDE MEASUREMENTS

The most useful part of this localised temporal discrimination, is that it can separate a mode from an incoherent intensity sum of modes based on the temporal delay of the waveguide. Once separated from the other modes in the waveguide, one can start to determine, not just modal dispersion characteristics, but the relative power between modes.

To provide some insight into how a separated mode, or more accurately mode overlap, can provide relative mode powers, when localised spectral interferences depend on the overlap between two modes at the particular location collected, we return to equation 4.22 and compare the terms with the features in figure 4.10

$$I(t,z) = \underbrace{(M_0^2 + r^2 M_1^2)\, A^2(t)}_{\text{Central max.}} + \underbrace{r M_0 M_1 \cdot \mathrm{e}^{\pm \mathrm{i}\Delta\beta z} A^2(t \pm \Delta\beta' z)}_{\text{Autocorrelation features}}. \tag{4.23}$$

With the data, it is trivial to calculate the ratio between the central maxima and the features. The ratio between the central maxima and the corresponding autocorrelation features is represented by the following

$$\frac{a(t = \Delta\beta' z)}{a(t = 0)} = \frac{r M_0 M_1 \cdot \mathrm{e}^{\pm \mathrm{i}\Delta\beta z}}{(M_0^2 + r^2 M_1^2)}, \tag{4.24}$$

where we can correct for the phase angle term from the phase velocity difference if necessary. Now a function based on the normalised mode profiles and the mode amplitude ratio coefficient $R(x)$ is created and substituted into equation 4.24 such that

$$\frac{a(t = \Delta\beta' z, x)}{a(t = 0, x)} = \frac{R(x)}{R^2(x) + 1}, \qquad R(x) = r\frac{M_1(x)}{M_0(x)}, \tag{4.25}$$

$$\therefore \frac{a(t = \Delta\beta' z, x)}{a(t = 0, x)}\left(R^2(x) + 1\right) - R(x) = 0. \tag{4.26}$$

The term $R(x)$ can be called the **relative autocorrelation ratio** function since the ratio between two modes, which both have unique profiles, varies as a function of position across the waveguide. With equation 4.25, the relative autocorrelation ratio function can be determined for the data. In order to determine the relative mode amplitude coefficient, the normalised mode profiles $M_0(x)$ & $M_1(x)$ must be known or determined. In this work the mode profiles were solved numerically and substituted into $R(x)$ so

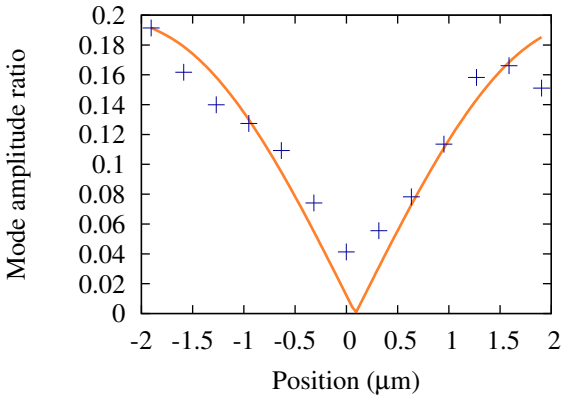

Figure 4.11: The relative autocorrelation ratio $R(x)$ as a function of position across the waveguide. The datapoints are the mode profile ratios as determined from the autocorrelation max/feature ratio and equation 4.25. The solid line is the fitted function using the mode amplitude coefficient ratio r. The fundamental mode outside $x = \pm 1.5$ μm drops significantly, this causes the accuracy of the measurement in this region to suffer.

that it can be fitted to the data, with the only fitting parameter being r, the mode amplitude coefficient. It is prudent to mention that the data depends on the inverse intensity of the fundamental mode, which drops near the noise level at the outer extent of the scans. This causes the precision of the relative autocorrelation ratio to suffer at these locations.

Figure 4.11 shows the relative autocorrelation ratio (the local field ratio between the modes) as a function of position across the waveguide profile. The data points were determined using equation 4.25 with the autocorrelation data, presented in figure 4.10, at a time delay of 180 fs. Using the normalised mode profiles M_0 and M_1 obtained from the EIM, the data was fitted to equation 4.25 using r as the fitting parameter, the result of which is displayed as a solid line. Typical experiments using this technique have considered such a value and called it the modal power index (MPI). MPI values are calculated with the assumption that most of the power exists in the fudamental mode (such that, using the equations presented in this work, $R(x)^2 + 1 \approx 1$). By using equation 4.26, this assumption of the power in the fundamental mode is not necessary and the ratio between modes with comparable power is possible.

Strictly speaking, the relative autocorrelation ratio $R(x)$ has three unknown parameters: r, M_0, and M_1; thus, if any two are known, the third can be determined using spectrally-resolving PSTM. It is unlikely that the normalised mode profiles cannot be determined, since modes can be determined using a variety of numerical methods for various waveguide geometries. Because of this, the only use of this interrogation of the spatial dependence of the spectral autocorrelations in this thesis, is for calculating the

relative mode amplitude coefficients since this is not trivial to predict in real systems.

In summary, the information that has been extracted in this work using localised spectral interferences is the relative group delay between two modes, the corresponding modes' amplitude overlap, and the relative power between them. This demonstrates how SNOM provides a useful tool for probing the inter-modal phenomena that occurs in a multimode waveguide of arbitrary geometries.

4.3.4 GVD AND SPECTRAL INTERFERENCE

Thus far, only the first two Taylor terms of dispersion have been discussed in terms of spectral interference. However, higher order dispersion can be obtained in principle using similar techniques. Traditionally, the group velocity dispersion (GVD) parameter, is determined by observing how the group velocity changed with wavelength. This can be done by observing spectral interference in the Fourier domain, over known distances. It is potentially viable however, to determine the GVD parameter without fitting a curve to the group velocity response of a waveguide, using the autocorrelation of the spectrum. This is useful for determining the local guiding characteristics of devices over a broad band of wavelengths. The precision of such non-destructive measurements using SNOM can be enhanced using linear regression over the propagation axis.

To understand how spectral interference can reveal the GVD parameter, we must return to equation 4.18. Previously, it was assumed that the propagation constant $\Delta\beta''(\omega)$, responsible for GVD, was negligible. Now the case where this is not a reasonable assumption will be discussed (i.e. for a broader spectrum or highly dispersive medium). The autocorrelation, using the convolution theorem, contains terms which are not delta functions; as such, analytical expressions are no longer trivial to express

$$I(t,x) = A^2(t) * \Bigg((M_0^2 + r^2 M_1^2)\delta(t) + rM_0M_1 \mathscr{F}\left[\cos\left(\Delta\beta\, z + \Delta\beta'\Delta\omega\, z + \frac{1}{2}\beta''\Delta\omega^2\, z\right)\right]\Bigg), \tag{4.27}$$

where $\mathscr{F}$ denotes the Fourier transform operator. The Fourier transform term has been left in its given form to keep the equations simple. It is not impossible, however, to breakdown the result of this equation since we know that a linear frequency dependence, $\Delta\beta'$ for example, results in a time shift in the Fourier domain. If one of the autocorrelations features is considered on its own and it is then centred (time-shifted)

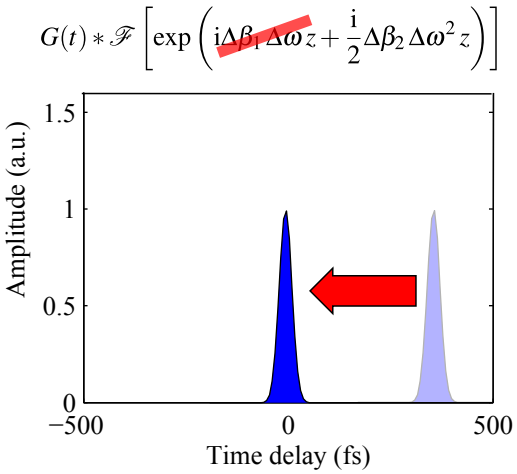

Figure 4.12: The pictorial effect of time-shifting an autocorrelation feature from inter-modal dispersion on the spectral interference equation. The term that depends linearly on frequency is removed, leaving only the group velocity dispersion term.

on the time axis, then the result in the frequency domain will be the original spectrum with the fringes due to the group velocity difference removed. This effect on the intensity spectrum is demonstrated pictorially in figure 4.12.

The resulting intensity spectrum from a time-shifted autocorrelation feature has the same spectrum envelope, since we have not considered powers that result in nonlinear effects in this thesis. The interference fringes will now follow a ω^2 dependence and can go negative (mathematically, the DC (central) feature on the autocorrelation was the feature preventing the intensity spectrum function going negative). This resulting feature can be fitted to a $\cos(\omega^2)$ function, and repeated with spectra collected at different locations along the guide, to take advantage of regression statistics and obtain an accurate value of the inter-modal GVD parameter. Such as a fit is presented in figure 4.13 where a numerically generated spectrum with spectral fringes from a defined GVD parameter was plotted with the time-shifted, back-Fourier-transformed autocorrelation feature. There is a slight discrepancy in the fit which can be attributed to the numerical sampling of time delays in the autocorrelation; when time shifting autocorrelation features numerically, one is confined by the discrete nature of time in the autocorrelation due to sampling in the frequency domain.

The numerically generated $\cos(\omega^2)$ function) presented in figure 4.13 was generated using a GVD parameter of $\beta_2 = -23$ ps^2 km^{-1} which is a typical value for bulk silica at optical frequencies[12]. The reconstructed power spectrum after time-shifting the relevant autocorrelation for an interference between spectra that has propagated through silica and free space for 3 cm, gives a value of $\beta_2 = -24.85$ ps^2 km^{-1}. This

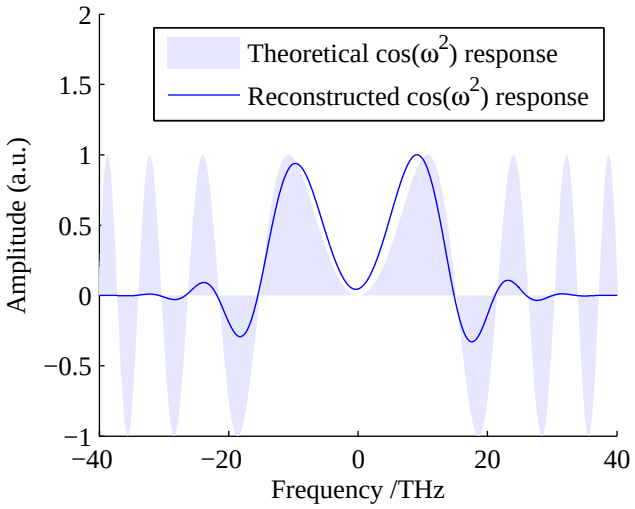

Figure 4.13: The plot of the cosine with the known propagation value at a particular location, with the time-shifted, back-Fourier-transformed autocorrelation feature. They show the expected results with a slight deviation from the actual cosine plot owing to the discreet time nature of the numerical data.

demonstrates that this method can, in principle, retrieve relative GVD parameters with 8% accuracy using similar spectral interference methods detailed in earlier sections of this chapter.

The ability to retrieve the relative GVD parameter from time-shifting autocorrelation features has been demonstrated on numerically generated data. The application of this technique requires a broadband light source and a multimode device. This would be a well-suited technique for measuring inter-modal GVD effects in integrated telecommunication devices and how they might be used for multimode processing.

4.4 Chapter summary

The sources of intermodal delays in a waveguide have been discussed by considering the solution of Maxwell's equations for a ridge waveguide structure. Waveguide dispersion was shown to exist even when material dispersion as absent and multimode waveguide structures were shown to have different dispersion characteristics for each of their guided modes.

The ability to make direct measurements on inter-modal effects using a spectrally-resolving PSTM device has been demonstrated. The group delay, accumulated between two propagating modes, has been directly observed in the temporal domain and the modes responsible were identified by their amplitude overlap profile. The group

delay difference between the first order and fundamental modes was determined consistent with the result obtained using numerical methods.

The relative mode amplitude coefficient between two waveguide modes was also determined by analysis of the autocorrelation central max and feature ratios.

A method of obtaining higher-order Taylor expansion terms for the propagation constant difference between two modes has been discussed. A test of this method was carried out on numerically generated test-data. The ability to observe delays via spectral interference and the local measurements of a SNOM probe has shown that PSTM is useful tool for mapping local delays in waveguide structures.

Future work may include using this localised spectral interference with a time-of-flight technique[13] or electrical spectrum measurements[14] to determine the absolute dispersion coefficients for modes in a waveguide.

REFERENCES

[1] Jonathan R Kurz, Jie Huang, Xiuping Xie, Takashi Saida, and Martin M Fejer. Mode multiplexing in optical frequency mixers. *Optics Letters*, 29(6):551, March 2004.

[2] D. Menashe, M. Tur, and Y. Danziger. Interferometric technique for measuring dispersion of high order modes in optical fibres. *Electronics Letters*, 37(24):1439, 2001.

[3] John D Mills, Tipsuda Chaipiboonwong, William S Brocklesby, Martin D B Charlton, Caterina Netti, Majd E Zoorob, and Jeremy J Baumberg. Group velocity measurement using spectral interference in near-field scanning optical microscopy. *Appl. Phys. Lett.*, 89(5):51101–51103, July 2006.

[4] Sam A Berry, James C Gates, and William S Brocklesby. Direct spatial-temporal discrimination of modes in a photonic lightwave circuit using photon scanning tunnelling microscopy. In *CLEO/Europe and EQEC 2011 Conference Digest*, OSA Technical Digest (CD), page CF_P19. Optical Society of America, May 2011.

[5] S. a. Berry, J. C. Gates, and W. S. Brocklesby. Determination of spatio-spectral properties of individual modes within multimode waveguides using spectrally resolved near-field scanning optical microscopy. *Applied Physics Letters*, 99(14):141107, 2011.

[6] Sergey Bozhevolnyi, Valentyn Volkov, Thomas Sø ndergaard, Alexandra Boltasseva, Peter Borel, and Martin Kristensen. Near-field imaging of light propagation in photonic crystal waveguides: Explicit role of Bloch harmonics. *Physical Review B*, 66(23):1–9, December 2002.

[7] Sergey I Bozhevolnyi and Valentyn S Volkov. Near-Field Characterization of Planar Photonic-Crystal-Waveguide Structures. *Philosophical Transactions: Mathematical, Physical and Engineering Sciences*, 362(1817):757–769, April 2004.

[8] J C Gates, J D Mills, and W S Brocklesby. Near-field scanning optical microscopy of standing waves in fiber Bragg gratings. *Applied Physics Letters*, 83(9):1890–1892, 2003.

[9] J W Nicholson, a D Yablon, S Ramachandran, and S Ghalmi. Spatially and spectrally resolved imaging of modal content in large-mode-area fibers. *Optics Express*, 16(10):7233, May 2008.

[10] D N Schimpf, R A Barankov, and S Ramachandran. Cross-correlated (Cˆ2) imaging of fiber and waveguide modes. *Optics Express*, 19(14):13008, June 2011.

[11] Tipsuda Chaipiboonwong. *Characterising nonlinear waveguides by scanning near-field optical microscopy*. PhD thesis, University of Southampton, 2008.

[12] Govind P Agrawal. *Nonlinear Fiber Optics*. Elsevier, 4 edition, 2009.

[13] Johan Hult, Rosalynne S Watt, and Clemens F Kaminski. Dispersion Measurement in Optical Fibers Using Supercontinuum Pulses. *Journal of Lightwave Technology*, 25(3):820–824, March 2007.

[14] J W Nicholson, S Ramachandran, S Ghalmi, E A Monberg, FV DiMarcello, M F Yan, P Wisk, and J W Fleming. Electrical spectrum measurements of dispersion in higher order mode fibers. *IEEE Photonics Technology Letters*, 15(6):831–833, June 2003.

- CHAPTER 5 -

TRACKING LIGHT IN A QUASI-RANDOM SCATTERER

Disorder based localisation has received much interest over the past 50 years. Yet, owing to its complex nature, it is not easily modelled and thus not fully understood. This type of localisation appears with impurities or imperfections that would usually cause diffusive transport, which is a type of transport where a wide range of propagation angles can be found at any location due to multiple scattering events. A number of objects that can undergo diffusive transport can be localised by disorder, including: electrons, magnetic spins, phonons, and photons. The cause of this localisation is coherence between multiple scattering paths. Since photons are easy to detect and, to a first order approximation, do not interact with each other, they are a good candidate for probing the nature of localisation in disordered media. Photonic bandgap structures with quasi infinite rotational symmetry are studied with PSTM, as they provide an environment in which the photonic bandgap phenomena should be identifiable, thus separable from their random scattering phenomena. This chapter gives a brief overview of the field of localisation and rotationally symmetric photonic bandgap materials then presents data obtained from such a rotationally symmetric photonic bandgap material: a pinwheel tile pattern which is suggested to have localisation properties owing to its quasi-random structure[1].

5.1 RANDOM SCATTERING THEORY

To allow effective interpretation of the results obtained with SNOM, it is prudent to spend some time on the basic theory of scattering and its background. This section

provides the motivation and theory necessary to understand the significance of the data collected for this project; a comprehensive review on the scattering of light by small particles is not necessary.

5.1.1 RANDOM SCATTERING OF LIGHT

The study of light propagation through a volume of disordered scatterers has its roots in astronomy where astronomers wished to understand how light from stars was affected by propagation through interstellar clouds. A comprehensive mathematical treatment of the macroscopic effects of light propagation through a scattering medium was published by Chandrasekhar in 1960[2]. In this publication, the effects of different scattering mechanisms were considered with some detail. However, the interference effects between different scattered paths was not considered; it is fair to assume that this is because any cumulative phase effects after propagating astronomical propagation distances between scattering sites would average to zero.

It was not until the 1985, when interference phenomena in highly-diffusive propagation of light were considered, that studies on how wave interference affects propagation were performed[3]. These studies were based on Nobel-prize research by Anderson where the transport of electron spin was inhibited by the interference of quantum states, published 27 years earlier.

This idea of highly diffusive propagation of light leads one to consider a definition of diffusive light. Diffuse light is light that, over a specified area, has its intensity uniformly distributed across all propagation directions. This is in contrast to most other types of light where the source can be located by studying the positional dependence of the spread of propagation angles present in the light.

5.1.2 ANDERSON LOCALISATION

Anderson first published work on localisation in 1958 where he gave a mathematical treatment of the diffusion of electron spin states between random “lattice” sites[4]. In this work, diffusion was halted owing to interferences of quantum wavefunctions’ random walk paths when the mean free path was on order of the wavelength. In later work, it was proposed that this “localisation” could be applied to classical waves; including light[3, 5, 6]. This phenomenon, whether applied to electrons or light, is now known as Anderson localisation or, sometimes, strong localisation. This condition where the mean free path is on order of the wavelength is known as the Ioffe-Regal regime and

is described as

$$kl^* \approx 1, \tag{5.1}$$

where $k = \frac{2\pi}{\lambda}$ is the wavevector and l^* is the mean free path between scattering events.

When diffuse light propagates in an non-absorbing diffusive (high density of elastic scatterers at random locations) medium, the transmission of intensity should follow an optical-equivalent Ohm's law[3] and decrease linearly with thickness providing that the thickness is greater than a few mean free paths of light. This diffusive propagation happens in sugars, white paint, clouds, and fog. A complete mathematical treatment of Anderson localisation is yet to be realised, and this is because a microscopic approach to tackling a system that cannot be broken down into unit cells is too complex[7]. However, light provides a framework to study its properties experimentally as photons do not interact with each other to a first order approximation, such that only phenomena caused by interference effects are observed; SNOM provides an experimental method of observing the microscopic behaviour of localisation.

5.1.3 Weak localisation

Similar to Anderson localisation, weak localisation is the term used to describe localisation effects that reduce transmission in random transparent medium (rather than inhibit it completely). Weak localisation occurs if paths traversed in a random medium can interfere, causing an increased probability that photons will return to their point of origin. As this probability increases, the chance that a photon will be returned back towards its source increases and thus the angular distribution of backscattered light decreases.

A consequence of this enhanced return probability is an enhancement of back-scattered light in non-absorptive media. Measurements on this back-scattered cone of light can reveal the mean free path of the light in the medium[8]. However, since the backscattered light does not penetrate the medium beyond a few mean free-path lengths, it does not contain detailed information about the localisation process or the role of absorption[9]. Weak localisation is considered the precursor to strong localisation (Anderson localisation)[10, 11].

5.1.4 Diffuse light propagation

Whilst macroscopic observations lack the rigour to explain the underlying causes of localisation, they can provide a way of quantifying localisation. Classical diffusion is

one such observation that can describe propagation through a random medium. The transmitted intensity from a source through a diffusive medium can be described by the Lambert-Beer law

$$I_{\text{source}}(z) = I_0 \exp\left[-z/l\cos\theta\right], \tag{5.2}$$

where $I_{\text{source}}(z)$ is the intensity of light direct from the source after propagating distance z though the diffusive medium, I_0 is the source intensity, l is the mean free path length and θ is the angle of incidence of the source. This equation is effective at describing the transmission of sunlight through clouds and car headlights through fog where, after a few mean free-path lengths, the source is invisible (its position is indiscernible) and only diffuse light reaches an observer. This should be the case for the samples studied in this project, which consist of an area containing scattering sites at "random" locations. For a non-absorptive medium, the intensity that does not get backscattered eventually gets converted into diffuse light. Diffuse light, unlike directional light, propagates through the medium obeying a diffusion equation

$$\frac{\partial}{\partial t} I_{\text{diffuse}}(\mathbf{r},t) = D\,\nabla^2 I_{\text{diffuse}}(\mathbf{r},t), \tag{5.3}$$

where I_{diffuse} is the diffuse light intensity at position $\mathbf{r}$ at time t and D is the diffusion coefficient. Since only the relationship between diffuse light intensity and distance is relevant in the context of SNOM system, whose scanning times result in the observation of steady state solutions, the time dependence is ignored; however, this equation is the first hint that diffuse propagation leads to effects in the temporal domain. For a planar geometry, and assuming that the system can be macroscopically regarded as isotropic perpendicular to the propagation axis, the diffusion equation reduces to $I''(z) = 0$ such that

$$I_{\text{diffuse}}(z) = I_0 \frac{L + z_0 - z}{L + 2z_0}, \tag{5.4}$$

where a phenomenological constant $z_0 \approx l$ which describes the offset of the trapping plane boundaries that provide the conditions $I(-z_0) = I_0$ and $I(L + z_0) = 0$, used as valid assumptions for the boundary conditions[7]. These boundaries exist outside the diffusive medium and represent the effective planes from where diffuse light enters the medium and the plane where the intensity would become zero. The total transmitted intensity can now be determined using the following

$$T = \frac{I_{\text{diffuse}}(z = L)}{I_0} = \frac{z_0}{L + 2z_0} \simeq \frac{z_0}{L}, \tag{5.5}$$

where the thickness L of the medium is assumed to be much greater than the mean free path l (hence also z_0) and no light from the source travels directly through the medium. As discussed earlier, diffuse light propagation follows an optical equivalent of Ohm's law for conductors. Anderson localisation causes a deviation from this diffusion solution and causes rapid exponential attenuation with increasing thickness.

In this simple case treatment, absorption effects have been neglected and such effects are beyond the scope of this investigation. It is possible to account for small absorption losses and, in the work described in this thesis, out of plane scattering using a scattering cross-section σ_{loss}. Thus far, the source intensity and diffuse intensity of propagating light have been treated separately. There is no trivial method of separating these two intensities when measuring the local intensity in a waveguide. This necessitates a theory that considers the propagation, and conversion from one to another, of these two types of intensities. Now, assuming homogeneous illumination of the scattering sample, we can express the intensity that is lost due to scattering and weak absorption as

$$\mathrm{d}I = -n\,\sigma_{\text{loss}}\,\mathrm{d}z, \tag{5.6}$$

where n is the density of scatterers such that the scattering mean free-path is $l = (n\,\sigma_{\text{loss}})^{-1}$. An expression for the loss of intensity can now be described as the difference between the intensity of light from the illumination source $I(z)$ and the in-plane scattered light $J(z)$ (which becomes the source of diffuse light in the system)

$$-\frac{1}{n\,\sigma_{\text{loss}}}\,\frac{\mathrm{d}}{\mathrm{d}z}I(z) = I(z) - J(z). \tag{5.7}$$

The two intensity terms have a dependence on the propagation angles with respect to the propagation axis. In this work, the launching mechanism prevents control of the source's launch angle and we scan areas far from the boundaries so we can assume that angular dependencies will be reduced for the macroscopic interpretation, thus intensity should decrease with z alone. An expression for the total intensity I_{total} as a function of propagation distance z can be described by the radiative transfer equation[7]

$$\frac{I_{\text{total}}(z)}{I_0} = \exp\left[-\frac{z}{l}\right] + \int_{-z_0}^{L+z_0}\mathrm{d}z' \int_0^1 \mathrm{d}\mu\,\frac{\exp\left[-|z'-z|/\mu\,l\right]}{2\mu}\,J(z'), \tag{5.8}$$

where we have introduced $\mu = \cos\theta$ such that for a propagating wave θ is the angle between propagation and the propagation axis $\mathbf{z}$. This equation describes the total intensity at a given location by summing the contribution of scattered light from each scatter site. Figure 5.1 shows a plot of this equation using numerical results from

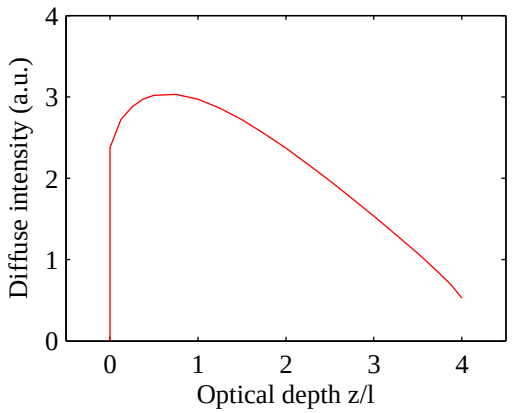

Figure 5.1: The diffuse intensity of light as a function of optical depth z/l, plotted using numerical data in Table 17 from Van de Hulst[12]. This plot shows the expected relationship between intensity of light and propagation for a system containing of a high density of isotropic scatterers in a slab geometry.

Table 17 in Van de Hulst[12] and this describes the expected form of the intensity *vs.* propagation distance relationship.

This section is concluded by summarising the effects of random scatterers. When random scatterers interact with light, they can convert a source with a known profile into diffuse light whose intensity profile as a function of propagation distance differs from that of a regular light source. This difference should enable one to identify whether diffuse or the incident light is being detected in the context of a SNOM scan where the intensity as a function of propagation distance is easily determined. If the mean free-path length of photons in the medium approaches its wavelength, the propagation of diffuse light will deviate from the expected linear case to exponentially attenuating; this reveals the onset of strong (Anderson) localisation. Since SNOM provides a non-destructive method to map the light intensity inside the waveguide, both the macroscopic and microscopic effects of random scatterers should be visible.

5.2 INTENSITY MAPPING IN PINWHEEL TILES

The scattering samples provided for this study, were not truly random as they were fabricated using computer code that provided a well-defined relationship between each scatter site, however they have a quasi-random structure owing to the fact that the region was a clipped region of a pinwheel tiling that is constructed using a seed tile rotated by irrational fractions of π. The results in the tiling pattern never appearing in the same rotational orientation and providing many different distances and angles

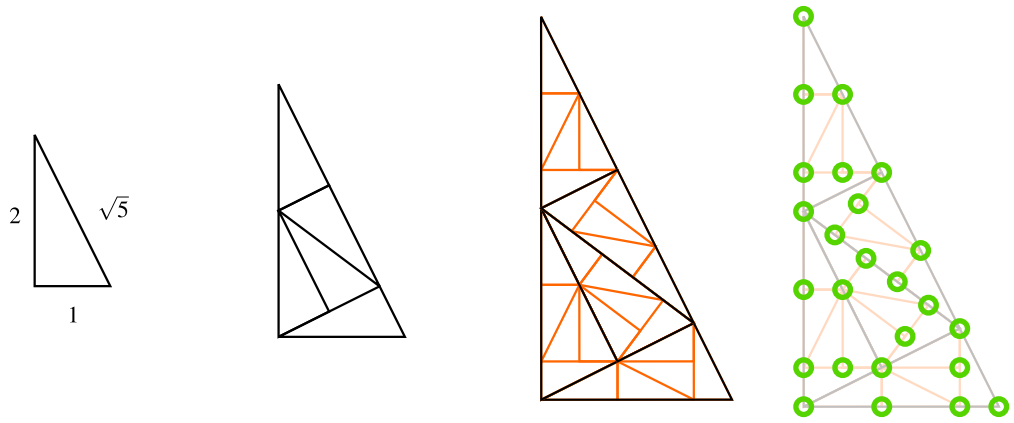

a.) Seed tile b.) First iteration c.) Second iteration - wth generated PQC

Figure 5.2: The construction of the pinwheel structure is depicted here. On each iteration, the seed tile is rotated by some irrational fraction of π. Due to this rotation, whilst there is a pattern that governs the position of the scatter sites, the structure cannot be decomposed into a unit cell and does not repeat itself and it does not contain any lines of symmetry.

between scattering sites like that of a random medium and a quasi-isotropic structure. This section will focus on the structure of the sample and then present the results obtained by a spectrally-resolving SNOM setup.

5.2.1 The pinwheel sample

It is highly desirable to have a photonic bandgap material with a high degree of rotational symmetry, since it offers more freedom in the angles that photonic crystal (PC) wavegudies can guide light efficiently. PC waveguides can only guide light efficiently down an axis of symmetry, because in other areas the effective spacing of the scatterers changes depending on projection angle.

Arbitrary bend angles are not efficient at guiding light and this is a cause of loss at junctions and bends; a typical bend angle would be 60° with a radius of curvature of one photonic crystal period. To create a less lossy PC waveguide, a greater selection of efficient guiding angles must be available; in other words, structures that possess rotational symmetry. Quasi-crystals, with their quasi-infinite rotationally symmetric photonic bandgap, have been studied as a potential route for photonic crystal waveguides with arbitrary bend angles[13, 14] and have also been shown to enhance the efficiency of transmission through 90° sharp bend angles[15]. Structures that posses such a photonic bandgap at any launch angle are known as complete photonic bandgap structures[16] and before photonic quasi-periodic structures only existed in periodic

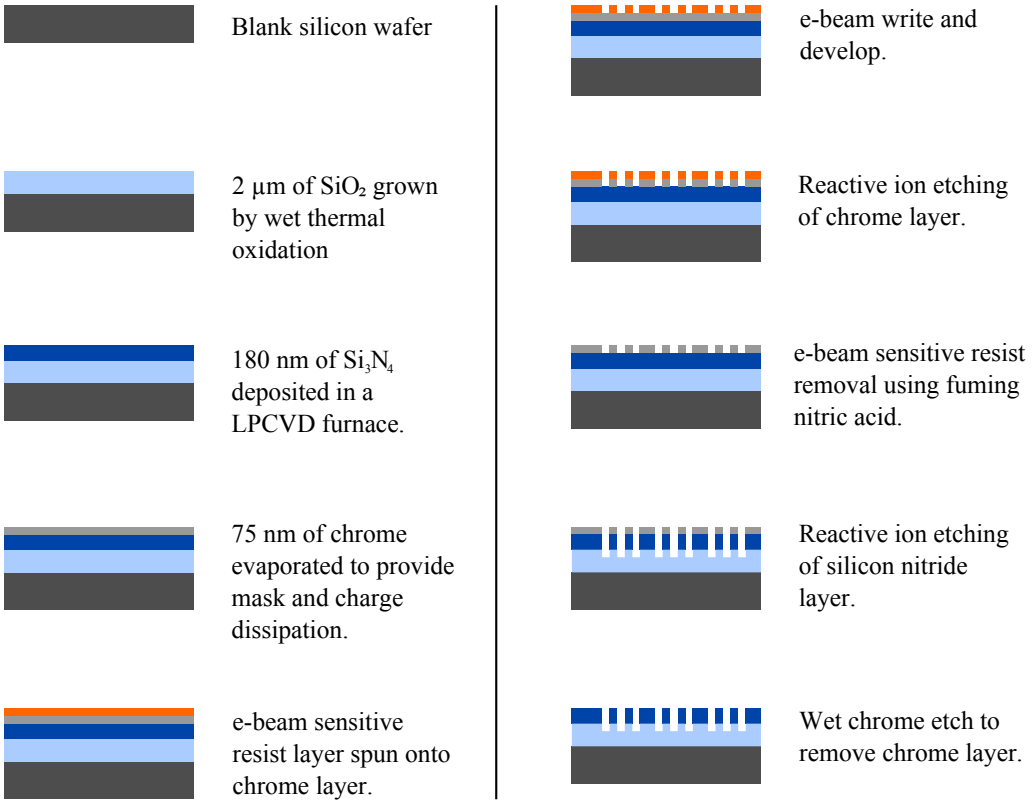

Figure 5.3: The fabrication process for creating the pinwheel tiling structure in silicon nitride. The chrome evaporation, e-beam write, and reactive ion etching of chrome was carried out by QUDOS Technology ltd. The other steps were carried out in cleanroom facilities at the University of Southampton.

structures with large refractive index contrast. Complete photonic bangaps with low refractive index contrast, can also be used to create slow light devices[17], which enhance light-matter interactions[18]. Slow light structures are of interest because of their potential application as optical buffers or memory elements[19, 20].

The sample studied in the spectrally-resolving SNOM setup was supplied by the School of Electronics and Computer Science (ECS) at the University of Southampton; the fabrication process is outlined in figure 5.3. The scattering region comprised of air holes roughly 110 nm in diameter spaced apart by a distance of around 285 nm. The silicon nitride layer was 180 nm thick, making the optical waveguide single mode in the vertical dimension for the wavelengths under study; this reduces complexity by avoiding intermodal dispersion caused by a multimodal nature in the vertical dimension. The guiding region up to the pinwheel region was of a slab waveguide slab geometry of silicon nitride approximately 75 μm thick, making it highly multimode in

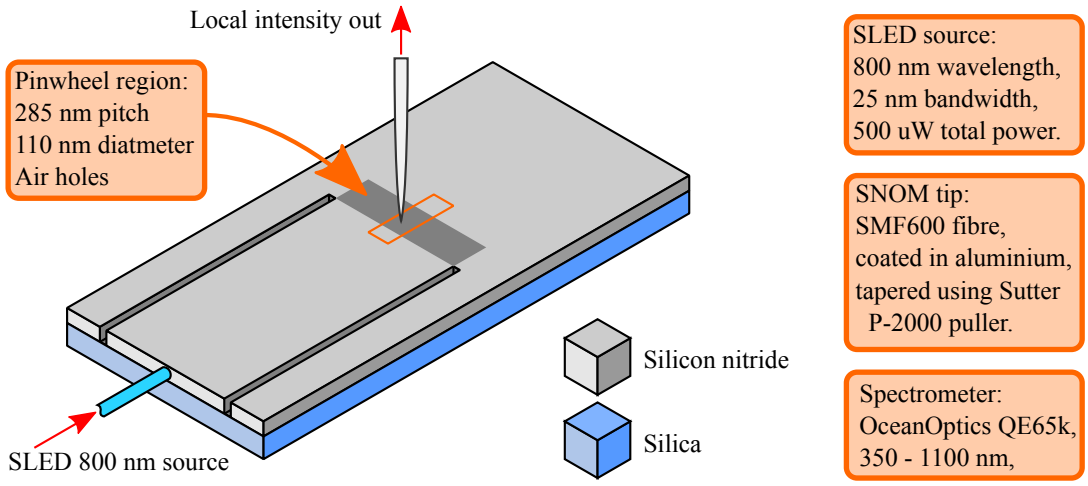

Figure 5.4: The experimental setup of the pinwheel intensity mapping experiment (not to scale). The fibre used to launch the SLED source was SMF600. The scanning area outline has been depicted as the orange rectangle surrounding the SNOM tip.

the lateral direction for optical wavelengths. This allows for near homogeneous illumination of the scattering region. A diagram of the sample and the experimental setup can be seen in figure 5.4.

The "game of life" was the creation that made John Horton Conway famous. However, he is a well-respected mathematician and is famous in the world of geometry for proving that a right-angled triangle with sides 1, 2 & $\sqrt{5}$ can be constructed using 5 smaller right-angled triangles with the same aspect ratio. This demonstrated in figure 5.2, where the construction of the triangles is shown for multiple iterations whose resulting pattern is known as pinwheel tiling. The holes were positioned according to this pinwheel tiling. On each interaction this seed tile is rotated by an irrational fraction of π, resulting in quasi-infinite rotation angles of the seed tile present for large sample areas; this is the key for creating a quasi-isotropic periodic bandgap medium. The quasi-random nature of the scattering sites, enables us to investigate, not only the nature of near-isotropic photonic bandgap materials, but the propagation of light in a random scatterer.

5.2.2 Intensity mapping

The pinwheel sample was illuminated using 633 nm light from a Helium Neon (HeNe) laser and 790 nm light from a super-luminescent light emitting diode (SLED). The SNOM probe was then scanned across the pinwheel region and the areas immediately before and after. The air holes are expected to scatter the guided light in the waveguide

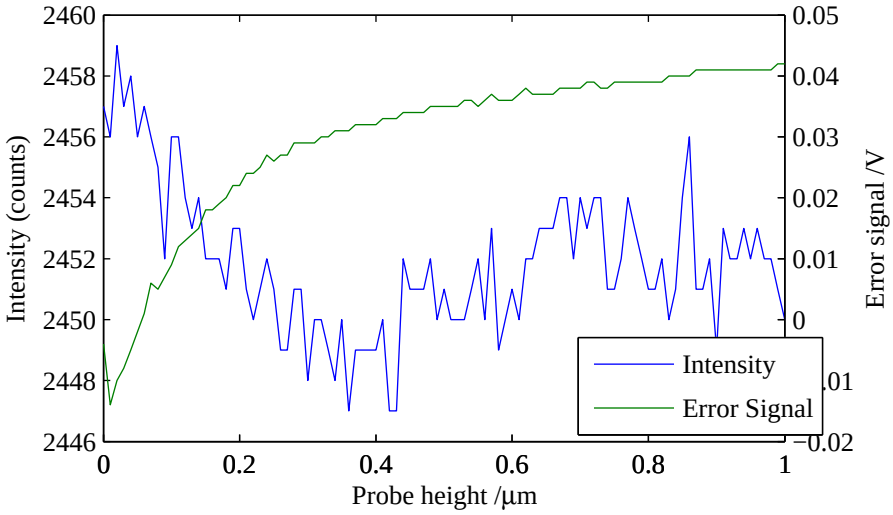

Figure 5.5: The intensity of light detected using an avalanche photodiode whilst bringing the near field probe down to the surface of the sample. The error signal (green) monitored from the PID controller reduces when in contact with the sample surface. As the probe gets closer to the near field region, the overall intensity reduces as less scattered can successfully launch into the probe. Once in the near field region, $x \leq 0.4\ \mu$m on this plot, the evanescent fields start to dominate the detected signal.

and thus expected to scatter light out of the waveguide. To ensure that light scattered outside the waveguide did not reduce the spatial resolution of the results, the probe was coated in aluminium using the shadow evaporation technique.

The effect of coating the near field probe on spatial resolution has already been presented in figure 3.5, where a direct comparison on the spatial frequencies detected with both coated and uncoated probes were presented for scans on this pinwheel sample. The response of a near field probe to scattered light can be demonstrated by monitoring the detected intensity as the probe is brought into the sample's near field region, this is presented in figure 5.5. In this figure, the intensity detected by an avalanche photodiode is plotted against the height of a nearfield probe as it is brought to the surface of the sample (at $x = 0\ \mu$m). As the probe is brought towards the sample surface ($x > 0.4\ \mu$m), the instensity of light detected decreases as less scattered light can be launched into the fibre successfully. Once in the near field region, $x \leq 0.4\ \mu$m in this figure, light from the evanescent wave dominates the detected signal. Whilst this figure suggests that the near field region extends to 400 nm away from the surface, this is not the case. Thermal drifts, whilst moving the probe and counting photons, are responsible for the apparent large near field region.

With a spectrometer connected to the near field probe, the area depicted in figure 5.4 was scanned. Focussing on the results from the HeNe laser source, the local inten-

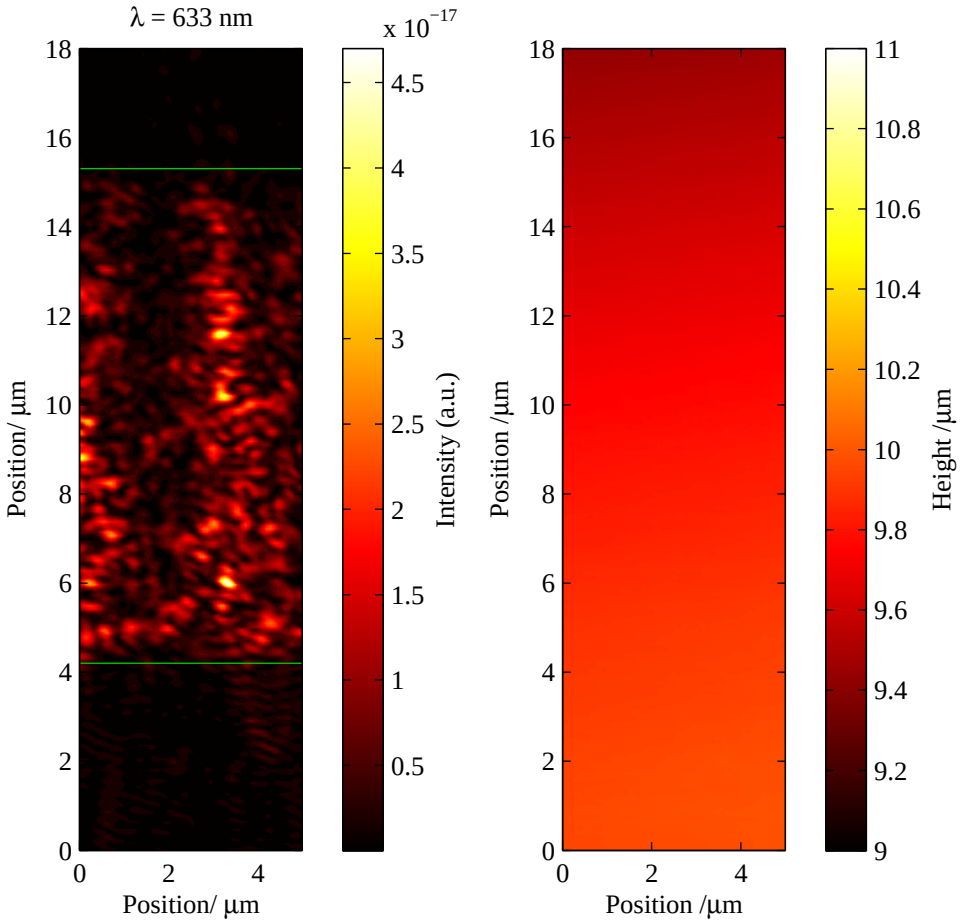

Figure 5.6: Left - The intensity of light from a He:Ne laser (633 nm) mapped using an aluminium coated SNOM tip. Right - the AFM trace of the SNOM scan, demonstrating that the localised intensities mapped are not due to defects on the surface of the waveguide.

sity detected is displayed in figure 5.6 alongside the AFM trace. Not easily seen in this figure, the relatively even input distribution of light quickly accumulates distinct paths once inside the pinwheel region between 4 μm $\lesssim y \lesssim$ 15.5 μm; some features present in this intensity map can be compared to the arbitrarily angled rows of scattering sites as seen in figure 5.2. As equation 5.8 predicts, an overall increased intensity of light in the pinwheel region reveals that more scattering is occurring in this region; the subsequent scattering is causing light to be scattered back towards the beginning of the structure, which is described by the integral part of equation 5.8. This high amount of scattering causes a large amount of light to be scattered out of the guiding layer. This out-of-plane scattering necessitates a coated near field probe, since local intensities can be mapped with higher precision using a coated probe in the presence of scattered

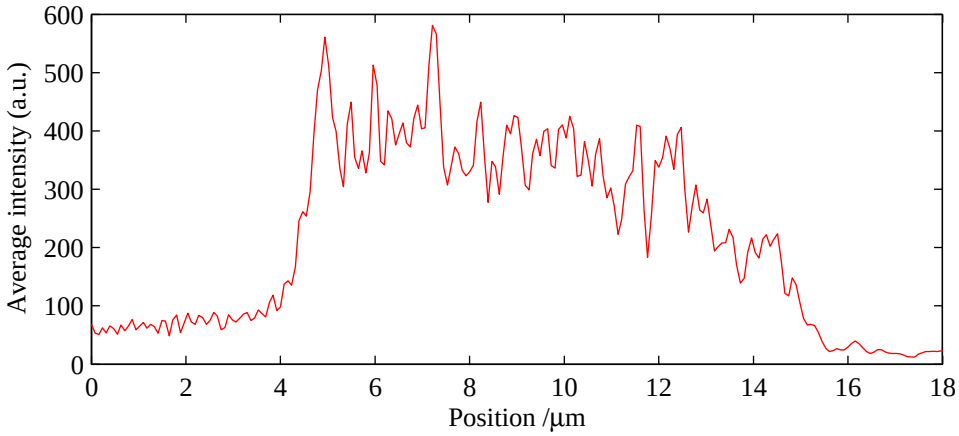

Figure 5.7: The line average He:Ne 633 nm light intensity as a function of position along the propagation axis. The pinwheel region is between $x = 4$ μm and $x = 15$ μm. The intensity profile appears to follow equation 5.8, suggesting that the dominant source of light detected is diffuse.

light, as discussed in chapter 3.

The flatness of the AFM trace in figure 5.6 shows that the macroscopic distributions of light are not due to surface defects on the waveguide and supports the argument that they are due to multiple scattering events caused by the sample's structure. The bright and dark fringes seen throughout the pinwheel region are interferences between the multiple scattering paths of light caused by the scattering sites inside the waveguide.

Figure 5.7 shows the average local intensity of the He:Ne light detected as function of propagation distance in the experiment. The pinwheel region is clearly identified by an overall increase in intensity, which appears not to decay exponentially along the propagation axis and is of similar form to that plotted in figure 5.1 which is described by equation 5.8. This is strong evidence that strong scattering exists in the pinwheel region, causing diffuse propagation of light to occur. The area leading up to the pinwheel region $0 < y < 4$ μm has a smaller linear increase in intensity. This linear intensity profile could be attributed to back-scattered light.

5.2.3 SPECTRALLY RESOLVING RANDOM PATHS

A medium comprising of a random structure, where interference affects the mean free path of propagating light, would have a delicate spectral response as the random paths for one wavelength would interfere differently from that of another. Figure 5.8 shows the different intensity distributions for the same scan area as figure 5.6, this time using an incoherent super-luminescent light emitting diode (SLED) with central wavelength

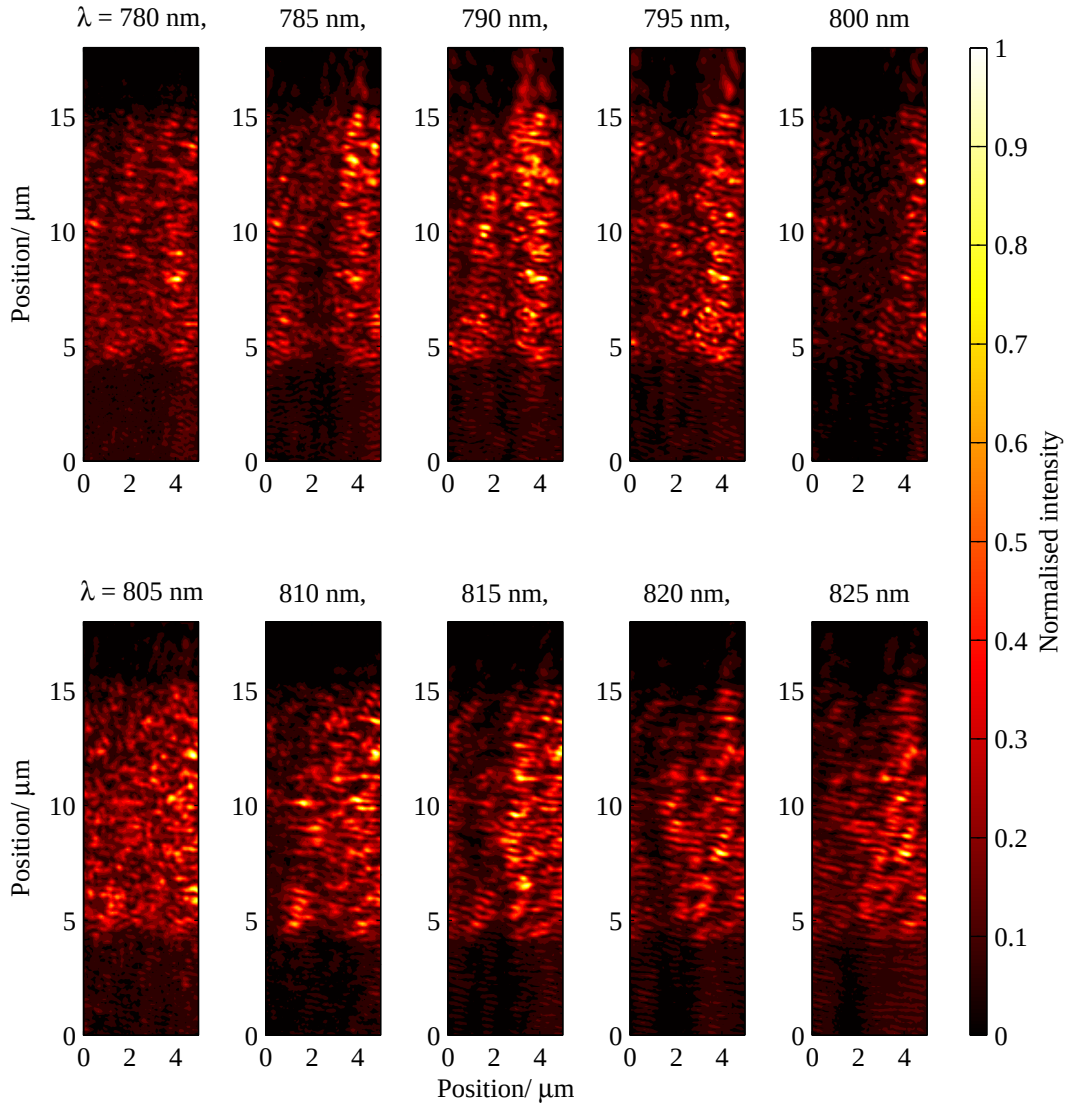

Figure 5.8: The light intensity mapped, for the same scan region of figure 5.6, for different intensities from 790 nm ± 25 nm, incoherent, SLED source. Figure 5.9 highlights some interesting features of this data for selected plots.

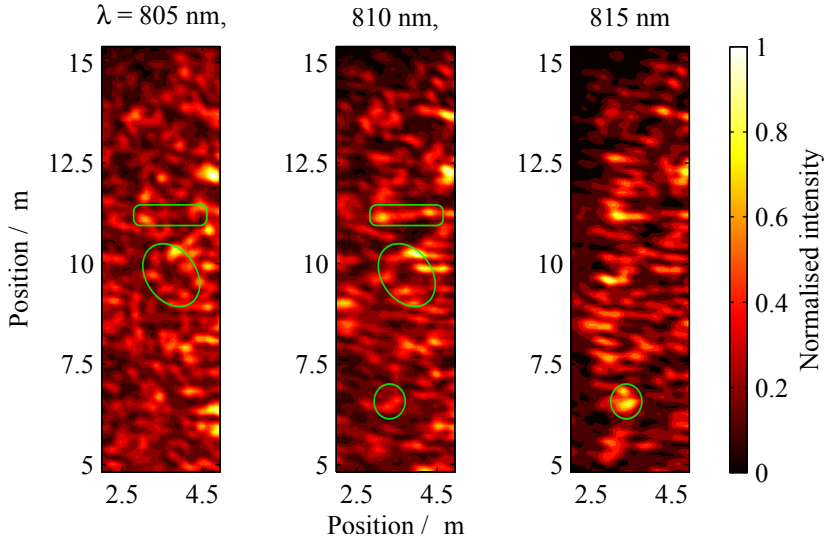

Figure 5.9: A close-up comparison of the intensity map presented in figure 5.8 for three wavelength separated by 5 nm. The top and bottom green rectangle and ellipses in the centre plot (also mapped on the left and right plots respectively) highlight areas that are sensitive to small wavelength changes. The green ellipse on the left and central plots identify an area that appears to have a standing wave loop at $\lambda = 805$ nm.

of 800 nm and 25 nm bandwidth; the sensitive wavelength dependence of the medium response is clearly visible as each plot represents a wavelength change of only 5 nm; this is further highlighted in figure 5.9 by the highlighted regions, which correspond to the same areas with a wavelength change of 5 nm between each plot. Evidence of closed loop formations are visible as a ring patterns in figure 5.8, most notably at $x = 1\ \mu$m, $y = 10\ \mu$m, & $\lambda = 800$ nm (highlighted in figure 5.9 by the green ellipse for wavelength $\lambda = 805$ nm). The presence of such closed loops, as discussed earlier, is considered to be evidence of weak localisation, the precursor to Anderson localisation. Without the ability to determine the mean free path associated with the pinwheel structure for particular wavelengths, it is not possible to draw inferences on whether the presence of these closed loops in this experiment are associated with the Ioffe-Regal regime ($kl^* \approx 1$).

Observation of the light that successfully propagates through the pinwheel structure, producing intensity at $y > 15\ \mu$m reveals another interesting feature of this scan. For wavelength $\lambda = 790$ nm, the amount of light that successfully transmits through the pinwheel region is comparable, intensity-wise, to the light detected inside the pinwheel region. It is unclear why this enhanced transmission for $\lambda = 790$ nm is occurring, but it could be due to the geometry of this particular pinwheel region is causing the light at this wavelength to have a route that is partially guided and not scattered to the same

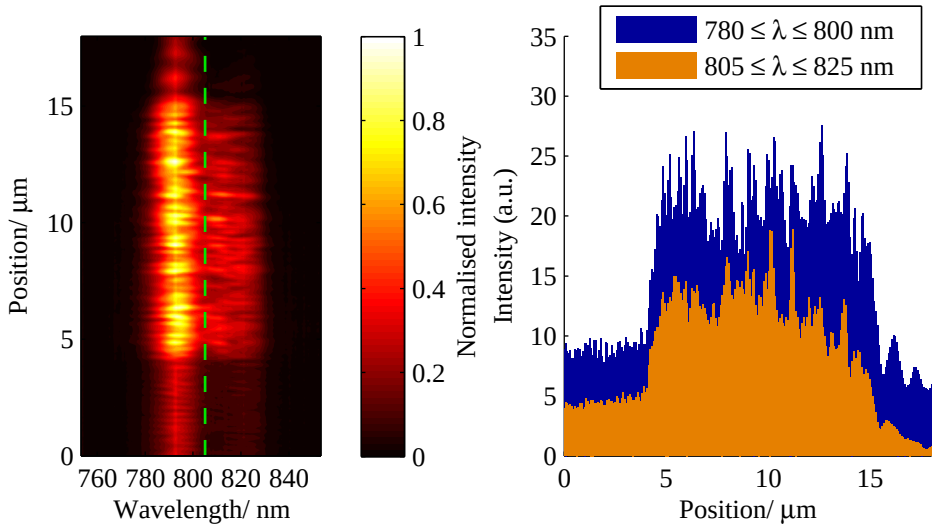

Figure 5.10: The spectral intensity plotted versus propagation distance through the medium. The spectra collected have been summed over the axis perpendicular to the propagation axis. Line plots of the two halves (separated by dashed green line) of the spectrum are given alongside for easier view of relative intensities.

degree as other wavelengths; it is not likely that this is due to the photonic bandgap nature of the medium as the wavelength does not correspond to the Bragg condition of any commonly found scatter site spacings. The argument for this is, at this wavelength of $\lambda = 790$ nm, a large proportion of the power seems to be localised between $2.5\ \mu\text{m} \leq x \leq 5\mu\text{m}$ which may suggest the light in this region is being guided; this is also the case for $\lambda = 800$ nm where some power also appears to propagate through the pinwheel sample. Providing that we can assume that this spatial restriction is not due to a photonic bandgap, there should be no such spatial localisation of optical power for a uniform illumination; this is perhaps the strongest evidence for the onset of localisation in this work.

To further observe the spectral response of the medium, it is beneficial to plot the spectrum (summed over the x axis) vs. the propagation distance so that one can see the spectral response as light propagates through the sample. This is plotted in figure 5.10, where the resonant response at $\lambda = 790$ nm can be seen directly. This resonant effect extends to the region before and after the sample region which suggests that this enhanced frequency response comes with a reflection of a substantial amount of power back towards the source of light. This may further indicate that the resonant response may be due to the photonic bandgap nature of the medium, since disorder-based localisation should occur across a range of wavelengths where the wavelength of light is greater than the mean-free path. However, the wavelength does not correspond

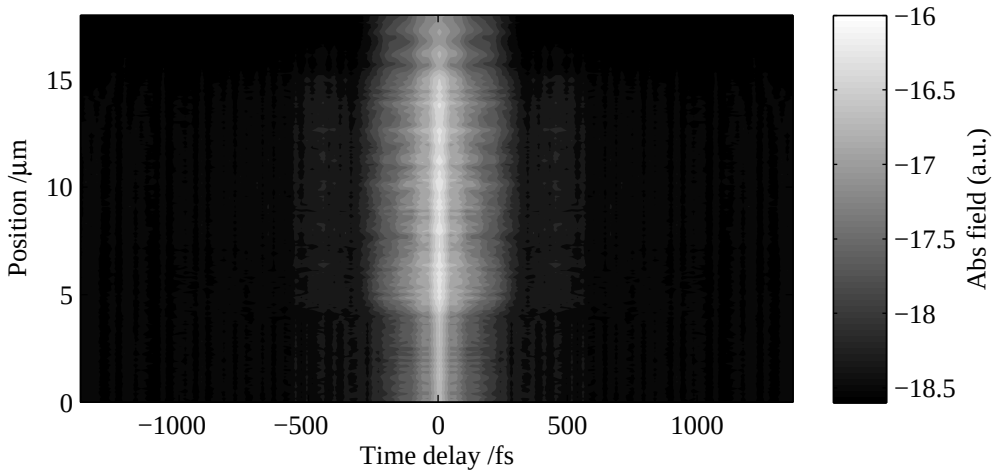

Figure 5.11: The average spectra autocorrelation as a function of propagation distance. The pinwheel region displays the delays present better (since the contrast is better).

to the Bragg condition for any of the common distances found within the pinwheel structure.

The transition between weak and strong (Anderson) localisation is not known at a microscopic level due to its complexity. As Anderson localisation starts to dominate the propagation mechanism, resonances in frequency may start to appear as destructive interferences cause an increased probability that light will travel down the path from which it came. Thus, it is not conclusive whether such frequency effects are actually due to Bragg conditions being satisfied or signatures of Anderson localisation.

The line plots are of the two regimes that are observed in figure 5.10, the "resonant" response (between wavelengths 780 & 800 nm) and the other half (between wavelengths 805 & 825 nm). The resonant response's average intensity profile remains fairly constant over the pinwheel sample, in contrast to the non-resonant response where the intensity starts to decrease after $y = 8\ \mu$m. This supports that the light at this wavelength may be guided by the pinwheel structure.

It is not unreasonable to consider that this may be a transition to a localised case where diffuse light is starting to be attenuated exponentially. For the wavelength studied here, and assuming that the pinwheel pitch 285 nm is a reasonable estimate for the mean free path, the wavelength can be compared with the mean free path l^* using the following

$$nkl^* = 1.8 \cdot \frac{2\pi}{800 \times 10^{-9}} \cdot 285 \times 10^{-9} \approx 4, \tag{5.9}$$

where n is the effective index in the pinwheel region and has been approximated. This equation suggests that the wavelength is comparable to the mean free path, but has

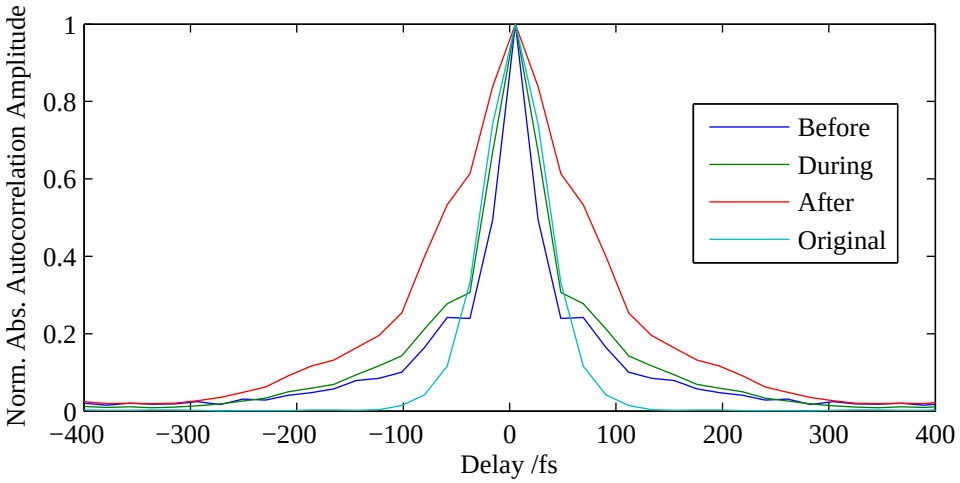

Figure 5.12: The normalised summed spectra autocorrelations for the three propagation regions (before, during, and after the pinwheel region). The unmodified spectrum autocorrelation is also plotted for comparison. It is clear that propagation (and reflection) through the pinwheel sample cause added delays to the original signal.

not reached the regime for Anderson localistaion. If disorder-based localisation occurs when the mean free-path becomes comparable to the wavelength of light then it is not unreasonable to expect a transition to appear over the wavelength range studied in this work. However evidence of this transition requires further analysis.

5.2.4 TRACKING TIME DELAYS

The work presented in chapter 4 revealed that a spectrally resolving SNOM could separate intensity maps based on the spatial distribution of time delayed signals. The same can be applied to this study of the quasi rotationally symmetric photonic bandgap structure. The random scattering paths that the medium creates should add delays with respect to the fundamental signal that propagates through the guide. In contrast to the delays present in chapter 4, where a well-defined delay accumulates between two modes, the random scattering nature of the medium should add a distribution of delays to the original signal.

The summed (across the x axis) autocorrelation as a function of propagation distance is presented in figure 5.11. The summed autocorrelation can show the distrbution of delays that exist for a specified propagation distance. There is a high refractive index contrast between the scatterers and guiding medium, such that the average impedance change at the boundaries causes reflections and may be contributing to the buildup of light in the pinwheel region. This causes impedance mismatch causes reflections,

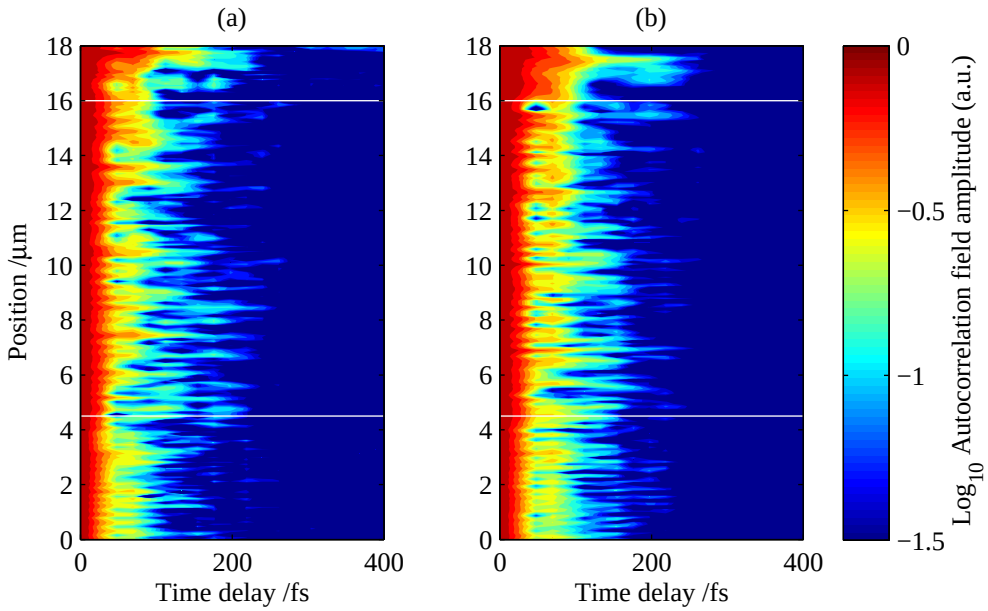

Figure 5.13: The autocorrelation (abs. field) taken as a function of propagation distance for two fixed position across the sample (line scan). The white lines denote the pinwheel sample region.

which masks the state of the light propagating towards the pinwheel region; the delays accumulated in the pinwheel region are present because of this reflection. To determine what delays are present due to the pinwheel region the autocorrelations for each region must be compared with the original source autocorrelation; this is presented in figure 5.12. The autocorrelations for each region of the scan have been normalised so that changes in overall intensity do not give the impression of delays that are just due to enhanced signal-to-noise ratio. The delays generated in the waveguide, similar to the delays found in the multimode waveguide in chapter 4, will manifest in the spectra autocorrelations as convolutions with the source's spectrum autocorrelation.

It is evident from figure 5.12 that delays have been created due to the scattering paths of the pinwheel region, since the width of the average autocorrelation of spectral measurements from the pinwheel sample is wider than the source spectrum autocorrelation. The area leading up to the pinwheel region and the pinwheel region itself have autocorrelation plots that differ significantly for the region after, which appears to have a much broader autocorrelation. It is likely that this is not due to a large distribution of delays, but a consequence of the narrow wavelength transmission around 790 nm.

It is not easy to identify specific delay phenomena in this data since delays local to a scattering site not identifiable when plotted with as an average distribution. Figure 5.13 presents two plots of the absolute autocorrelation field for two line scans that

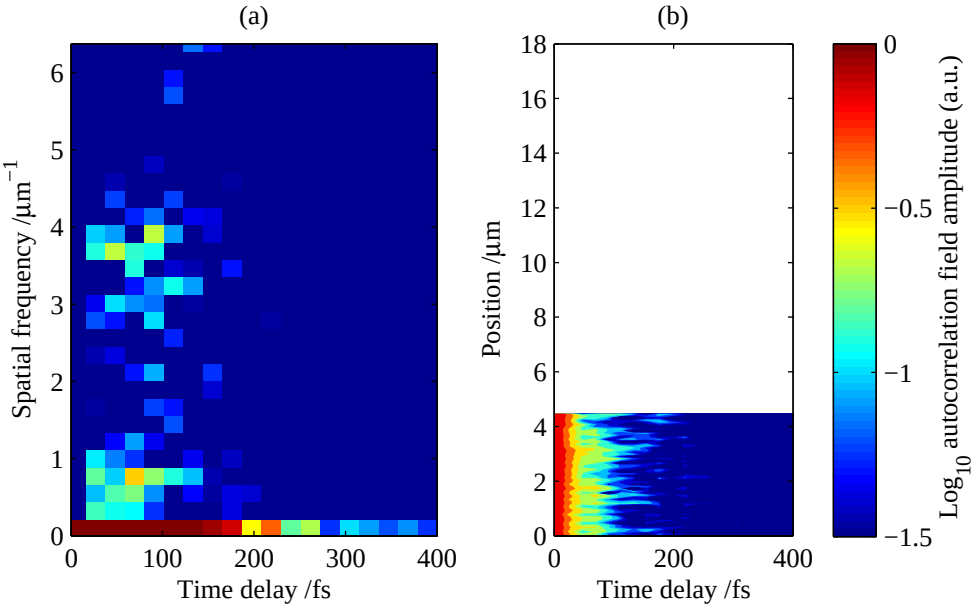

Figure 5.14: (left) Fourier analysis of the autocorrelation features along the propagation axis for the waveguide region before the pinwheel sample. (right) The abs. autocorrelation field *vs.* propagation distance of the data used in the Fourier analysis.

were scanned along the propagation axis of the sample at two different position across the waveguide. The plots are similar in terms of the width of the autocorrelations, which reveals that a translation does not infer significant changes in the scattering. Along the propagation axis, there appears to be a periodic structure to features in the autocorrelation, most notably between delays of 100 fs and 200 fs. To investigate periodicity in the delay features, the autocorrelations collected for one of the line scans was separated into before and during the pinwheel region, then each region was subject to a Fourier transform along the propagation axis. The results of which are plotted in figure 5.14 and 5.15.

In figures 5.14 and 5.15, the Fourier analysis of autocorrelation frequncies along the propagation axis reveal strong signals for a spatial frequency of 3.87 μm. The assumption that an effective index for the sample of $n_{\text{eff}} = 1.52$, obtained by solving the planar waveguide approximation described in chapter 4, for the guided waves is an overestimate is reasonable since the pinwheel region introduces a fraction of air holes into the silicon nitride and is the solution for the fundamental mode. The spatial frequency, assuming a refractive index of $n_{\text{eff}} \approx 1.52$, corresponds to a wavelength of 393 nm. This wavelength is very close to $\lambda_0/2 = 395$ nm and thus can be assumed to be due to a standing wave caused by reflections by the impedance mismatch at the pinwheel region boundaries. Working backwards, the effective index for the planar

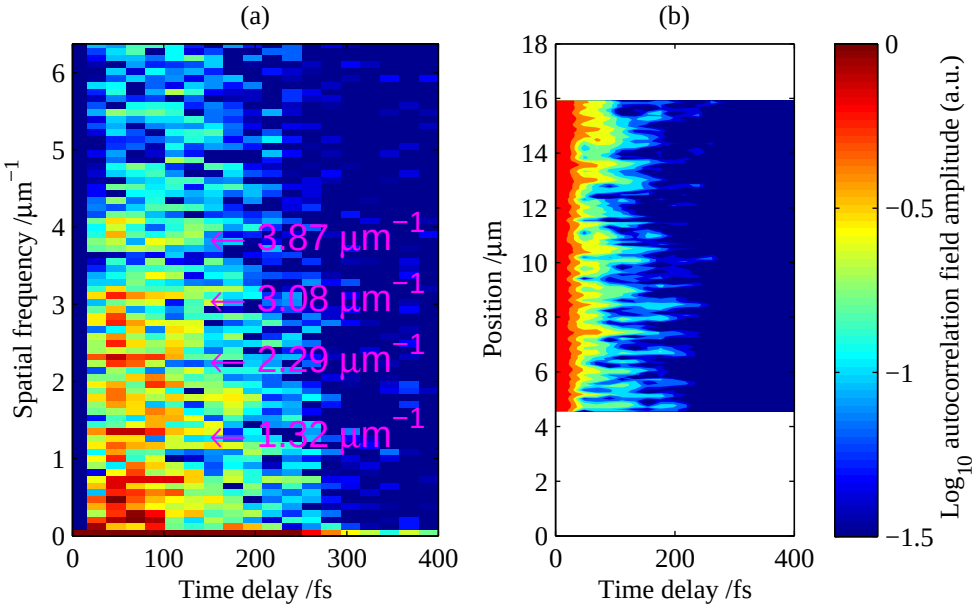

Figure 5.15: (left) Fourier analysis of the autocorrelation features along the propagation axis for the pinwheel region. Various spatial frequencies with strong signals are labelled. (right) The abs. autocorrelation field *vs.* propagation distance for the data interrogated with Fourier analysis.

layer can be determined using the spatial frequency measured

$$n_{\text{eff}} = \frac{\lambda}{2}u = \frac{790\text{ nm}}{2} \cdot 3.87\ \mu\text{m}^{-1} = 1.53 \tag{5.10}$$

where u is the spatial frequency detected. More interestingly, the spatial frequency of such a standing wave interference does not change significantly. This indicates that the average impedance approach to simplify the waveguide is not effective at describing the propagation of light through the pinwheel sample. This is likely to be due to the strong scattering nature of the pinwheel region, as plane waves do not propagate unperturbed through the sample. The resulting perturbations cause large variations in the propagation angles of the incoming light; it behaves as a light diffuser. As discussed earlier, the propagation behaviour of diffuse light differs from that of directional light.

The effectiveness of the planar waveguide approximation to predict effective index values has been demonstrated by the excellent agreement with the measured spatial frequency of a standing wave inside the waveguide. Solving the guidance condition for this planar waveguide geometry predicts a group index of $n_g = (n + \lambda \frac{\mathrm{d}n}{\mathrm{d}\lambda}) = 1.22$. Using this group index, the delays detected in the autocorrelation in figure 5.15 can be associated with a propagation path difference between photons. Delays of 200 fs correspond to a propagation path difference of 49 μm, which gives an indication

of the strong scattering present in this pinwheel region. The 25 nm bandwidth of the illumination limits the temporal resolution of the autocorrelation to 40 fs, which corresponds to a propagation path difference of approximately 9.8 μm inside the guide, which is a path comparable to the dimensions of the sample. Thus the ability to detect temporal phenomena at the scale of scattering lengths is restricted in this setup. A source with a larger bandwidth is required for investigating temporal phenomena at this scale.

5.3 CHAPTER SUMMARY

The different propagation mechanisms that light undergoes in a highly scattering waveguide has been briefly introduced and compared with data taken from a pinwheel tiling scattering waveguide. The pinwheel sample has been introduced and its usual characteristic as being a quasi-isotropic photonic bandgap device. The effective index of the fundamental mode in the guiding region has been determined experimentally by analysing the spatial frequency of standing wave patterns. The ability to measure the local E-field intensity at different wavelengths across the sample was presented with the aim of providing insight to the microscopic processes that are occurring due to multiple random scattering paths.

The pinwheel tiling's complex patterning structure makes it difficult to make conclusions on propagation characteristics of the sample due to the large amount of scattering. The next chapter looks at mapping temporal delays between propagating paths by using the temporal discrimination technique, the same technique used to identify mode field profiles in chapter 4.

REFERENCES

[1] Tom D M Lee. *Investigation of highly symmetric photonic quasi crystals*. PhD thesis, University of Southampton, 2006.

[2] S Chandrasekhar. *Radiative Transfer*. Dover Books on Physics. Dover Publications, 1960.

[3] Philip Anderson. The question of classical localization A theory of white paint? *Philosophical Magazine Part B*, 52(3):505–509, September 1985.

[4] P. Anderson. Absence of Diffusion in Certain Random Lattices. *Physical Review*, 109(5):1492–1505, March 1958.

[5] Sajeev John, H. Sompolinsky, and Michael Stephen. Localization in a disordered elastic medium near two dimensions. *Physical Review B*, 27(9):5592–5603, May 1983.

[6] Ad Lagendijk, Bart van Tiggelen, and Diederik S. Wiersma. Fifty years of Anderson localization. *Physics Today*, 62(8):24, 2009.

[7] M. van Rossum and Th. Nieuwenhuizen. Multiple scattering of classical waves: microscopy, mesoscopy, and diffusion. *Reviews of Modern Physics*, 71(1):313–371, January 1999.

[8] Yasuo Kuga and Akira Ishimaru. Retroreflectance from a dense distribution of spherical particles. *Journal of the Optical Society of America A*, 1(8):831, August 1984.

[9] G. Watson, P. Fleury, and S. McCall. Searching for photon localization in the time domain. *Physical Review Letters*, 58(9):945–948, March 1987.

[10] Meint Albada and Ad Lagendijk. Observation of Weak Localization of Light in a Random Medium. *Physical Review Letters*, 55(24):2692–2695, December 1985.

[11] Pierre-etienne Wolf and Georg Maret. Weak Localization and Coherent Backscattering of Photons in Disordered Media. *Physical Review Letters*, 55(24):2696–2699, December 1985.

[12] H C Hulst. *Multiple light scattering: tables, formulas, and applications*. Multiple Light Scattering: Tables, Formulas, and Applications. Academic Press, 1980.

[13] Tom D M Lee, Greg J Parker, Majd E Zoorob, Simon J Cox, and Martin D B Charlton. Design and simulation of highly symmetric photonic quasi-crystals. *Nanotechnology*, 16(11):2703–2706, November 2005.

[14] Me Zoorob, Md Charlton, Gj Parker, Jj Baumberg, and Mc Netti. Complete photonic bandgaps in 12-fold symmetric quasicrystals. *Nature*, 404(6779):740–3, April 2000.

[15] Chongjun Jin, Bingying Cheng, Baoyuan Man, Zhaolin Li, Daozhong Zhang, Shouzheng Ban, and Bo Sun. Band gap and wave guiding effect in a quasiperiodic photonic crystal. *Applied Physics Letters*, 75(13):1848, 1999.

[16] D Cassagne, C Jouanin, and D Bertho. Hexagonal photonic-band-gap structures. *Physical Review B*, 53(11):7134–7142, March 1996.

[17] Gregory J. Parker. Biomimetically-inspired photonic nanomaterials. *Journal of Materials Science: Materials in Electronics*, 21(10):965–979, July 2010.

[18] Thomas F. Krauss. Why do we need slow light? *Nature Photonics*, 2(8):448–450, August 2008.

[19] Fengnian Xia, Lidija Sekaric, and Yurii Vlasov. Ultracompact optical buffers on a silicon chip. *Nature Photonics*, 1(1):65–71, January 2007.

[20] Jacob B Khurgin. Optical buffers based on slow light in electromagnetically induced transparent media and coupled resonator structures: comparative analysis. *Journal of the Optical Society of America B*, 22(5):1062, 2005.

- CHAPTER 6 -

TEMPORAL DISCRIMINATION ON A HIGHLY SCATTERING SAMPLE

In the previous chapter, spectral interrogation of light propagating through a highly scattering sample was presented. This chapter looks into the temporal discrimination to as a tool to map delays. Theoretical plots of the temporal delays between paths is modelled for a small number of scatters to demonstrate what this abstract method of plotting delays can achieve. This technique is then applied to the spectral data collected in the previous chapter with the goal of identifying any localisation of delay features. Temporal discrimination is going to be the term used to describe the mapping of autocorrelation fields for a specified time delay value.

6.1 2D TEMPORAL DISCRIMINATION

In chapter 4, the autocorrelation field as a function of position across the waveguide was presented. This data was from a single line scan orthogonal to the propagation axis and identified the delay between two propagating modes. The relative phase between the modes' spatial profiles was also provided. For the pinwheel sample however, there is a 2D map of intensities at each wavelength. Conceptually, this complicates the presentation of information. To provide familiarity to the plots presented later in this chapter, this section aims to present plots using the temporal discrimination technique for simplified scenarios. A discussion about the suitability of this technique for measuring such phenomena is then discussed.

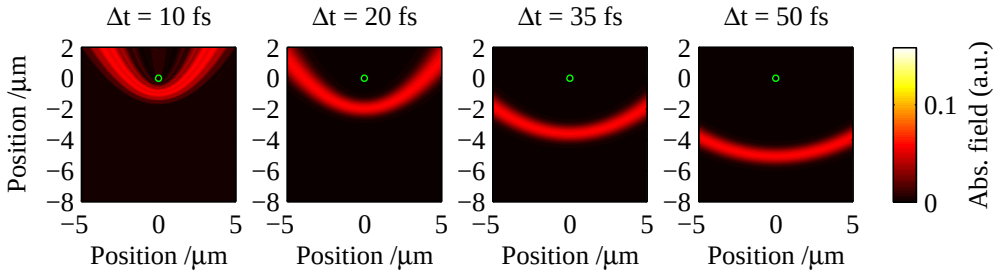

Figure 6.1: The theoretical plots of the temporal discrimination field maps for a single isotropic point scatterer, when illuminated with a source bandwidth of 130 nm at a central wavelength of 790 nm. Each plot represents four different time delays Δt (indicated by the delay above each plot).

6.1.1 A SINGLE POINT SCATTERER

With regards to scattering phenomena, the simplest case scenario is a single point scatterer, which scatters a plane wave isotropically. In this case scenario, light is scattered back towards the incoming plane wave and off at all angles, each of which acquire a delay with respect to the incoming plane wave. When plotting a field map after temporal discrimination, what is displayed in the plot are the areas where a specified delay can exist due to the geometry of the setup. Such a plot is presented in figure 6.1, where the absolute autocorrelation field corresponding to four different time delays Δt are plotted for a numerical simulation of an isotropic point scatterer under an illumination wavelength of 790 nm with 130 nm bandwidth (Gaussian profile). This plot highlights the areas where the specified delays can exist due to a propagation difference between the incident wave and scattered wave. Such an abstract plot is useful for locating the positions at which a certain delay might occur, which could be used in PLCs to impose time delays (or spectral finges) on signals for the purposes of optical processing.

Unfortunately, a 130 nm bandwidth was not available to use in the experiment.

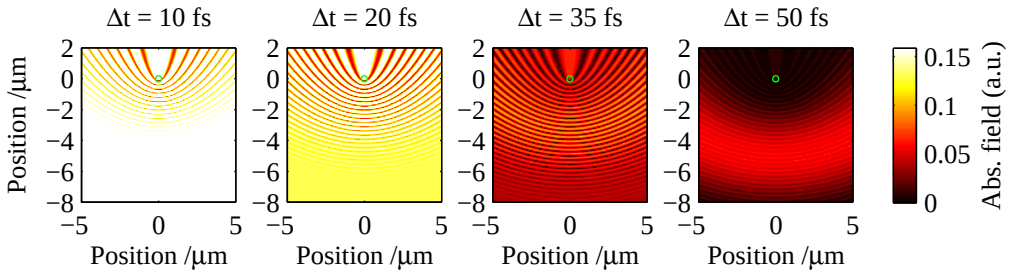

Figure 6.2: The theoretical temporal discrimination plots for the same setup as figure 6.1 using a source bandwidth of 25 nm.

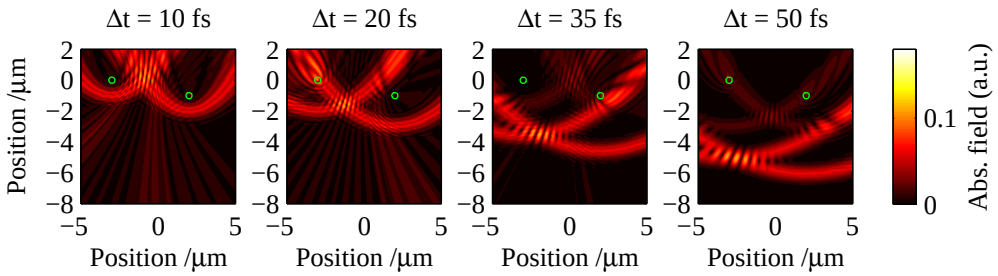

Figure 6.3: Theoretical temporally discriminated absolute autocorrelation fields for various time delays Δt (as specified above each plot) for two isotropic point scatterers under an illumination of wavelength of 790 nm and 130 nm bandwidth. At locations where time delays due to both scatterers and the incoming wave are equal, interference fringes manifest in the plots as the autocorrelation fields corresponding to each delay phenomena add up constructively or destructively.

This limits the temporal resolution of the spectra autocorrelations, which are used to construct the time delay maps. The same scenario, as figure 6.1, is modelled with a source bandwidth of 25 nm in figure 6.2. The bandwidth used in this figure matches that of the SLED used for illuminating the pinwheel sample in chapter 5. The subsequent reduction in temporal resolution has created artefact fringes in the plots for time delays below 50 fs. This is likely to be a consequence of the spectral width of the interference fringes due to such small delays being comparable to the spectral width of the source. Because of this, mapping a time delay that is smaller than the temporal resolution available due to the source bandwidth is not reliable.

6.1.2 Multiple scatterers

The effect of introducing multiple scatterers is now considered. As seen in chapter 4, the autocorrelations can provide information about the relative phase between two waves that have a time delay. This occurs because different phase angles for a specified delay, will manifest as a linear shift of the interference pattern on the source spectrum. This phase angle difference is reproduced in the autocorrelation. As such, the detected autocorrelation fields detected for two different scattering events can interfere.

The absolute autocorrelation field for specified time delays Δt (specified above each plot) for a system of two isotropic point scatterers under an illumination wavelength of 790 nm with 130 nm of bandwidth is presented in figure 6.3. This plot demonstrates the interferences of delay fields at locations where identical delays are created between the source and the 2 scatterers. This interfering of autocorrelation fields is a source of great

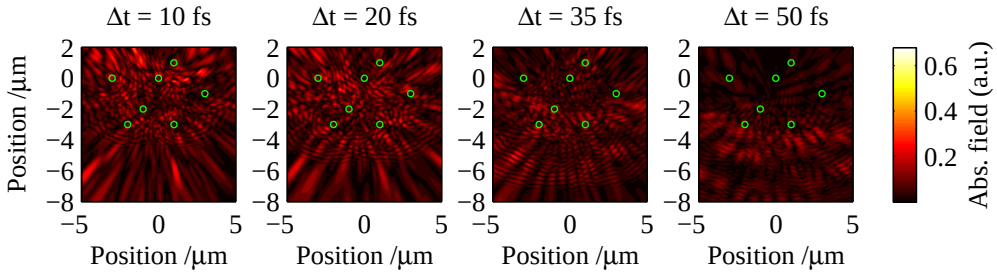

Figure 6.4: Theoretical temporally discriminated absolute autocorrelation fields for various time delays Δt (as specified above each plot) for seven randomly placed isotropic point scatterers under an illumination of wavelength of 790 nm and 130 nm bandwidth.

complexity in these delay maps, especially for a large number of scattering events.

Similar to the previous numerical simulations present, figures 6.4 and 6.5 present the numerically generated absolute autocorrelation fields at a specified time delay Δt of seven isotropic point scatterers using illumination sources with bandwidths of 130 nm and 25 nm respectively. The level of complexity of these plots has increased considerably with the number of scattering sites. Observation of the plots in figure 6.4, representing an illumination bandwidth of 130 nm, reveals that with a large number of scatterers, amplitude artefacts begin appearing at locations where such delays could not occur. A good example of this occurs for a delay of $\Delta t = 10$ fs. There are autocorrelation amplitudes detected, for this delay, between $-8\ \mu\text{m} \leq y \leq -6\ \mu\text{m}$. With the geometry of scatterers, such a delay of 10 fs could not occur in this region. However, the mapping of delays caused by the scatterers is still possible by observing the interference fringes close to the scatterers. The amplitudes mapped in the temporal discrimination plots appear to be chaotic in regards to their pattern but they fill the plot with an ambient intensity. Where the delay signal interferes with this ambient intensity,

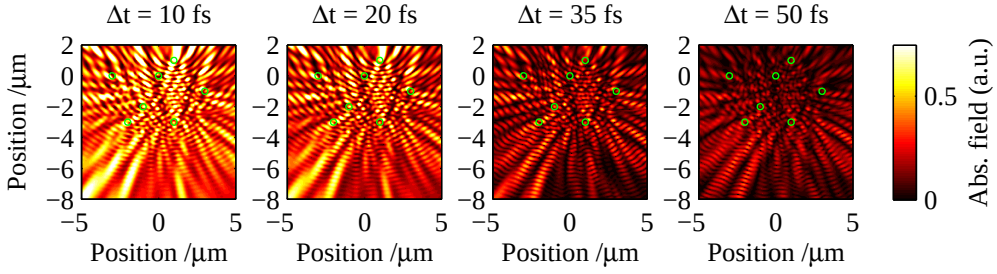

Figure 6.5: Theoretical temporally discriminated absolute autocorrelation fields for the same scattering setup as figure 6.4 under an illumination of wavelength of 790 nm and 25 nm bandwidth.

the changes in phase appear as fringes that map the location of the delay signals. This can be seen in figure 6.4 just above $y = -4\ \mu$m. The same fringe pattern can be seen in figure 6.5, but due to the reduced bandwidth occurs over larger areas (limiting the precision of the method to determine locations of specific time delays). This phenomena highlights that, for a large number of scatterers, the spatial behaviour of these autocorrelation delay interference fringes are more useful at highlighting temporal phenomena when a large number of scatters are present.

6.1.3 TEMPORAL DISCRIMINATION SUMMARY

This section has presented numerical simulations of temporally discriminated autocorrelation fields for a system of isotropic scatterers to provide familiarity to the information contained within the plots. The plots reveal areas that contain signals that have acquired a specified delay. For a large number of scatters, as is the case in the pinwheel tiling sample discussed in the previous chapter, the spatial behaviour of interference fringes and phase effects are more useful than observation of amplitude, as ambient autocorrelation fields appear as artefacts when searching for small delay values.

6.2 DELAY MAPPING IN THE PINWHEEL SAMPLE

The spectra collected when making measurements on the pinwheel samples with the SNOM setup will now be subject to the temporal discrimination technique. The aim of discriminating signals with a specified time delay is to identify propagation routes that light may be using to reach the end of the pinwheel sample.

6.2.1 INTENSITY-DELAY SIGNAL CORRELATION

Without specifying a time delay, with which to map the autocorrelation fields, the autocorrelation widths may provide insight into the spatial distribution of intensities whilst propagating inside the pinwheel region. A small propagation route inside the sample traversed multiple times would add a delay to the propagating signal and would cause an intensity build up in a specific area of the sample. However, if delays are occurring over larger propagation distances, this build up of intensity would necessarily be localised to a specific area in the sample. Figure 6.6 presents the total electric field intensity mapped (across all wavelengths) next to a plot which represents the variance in

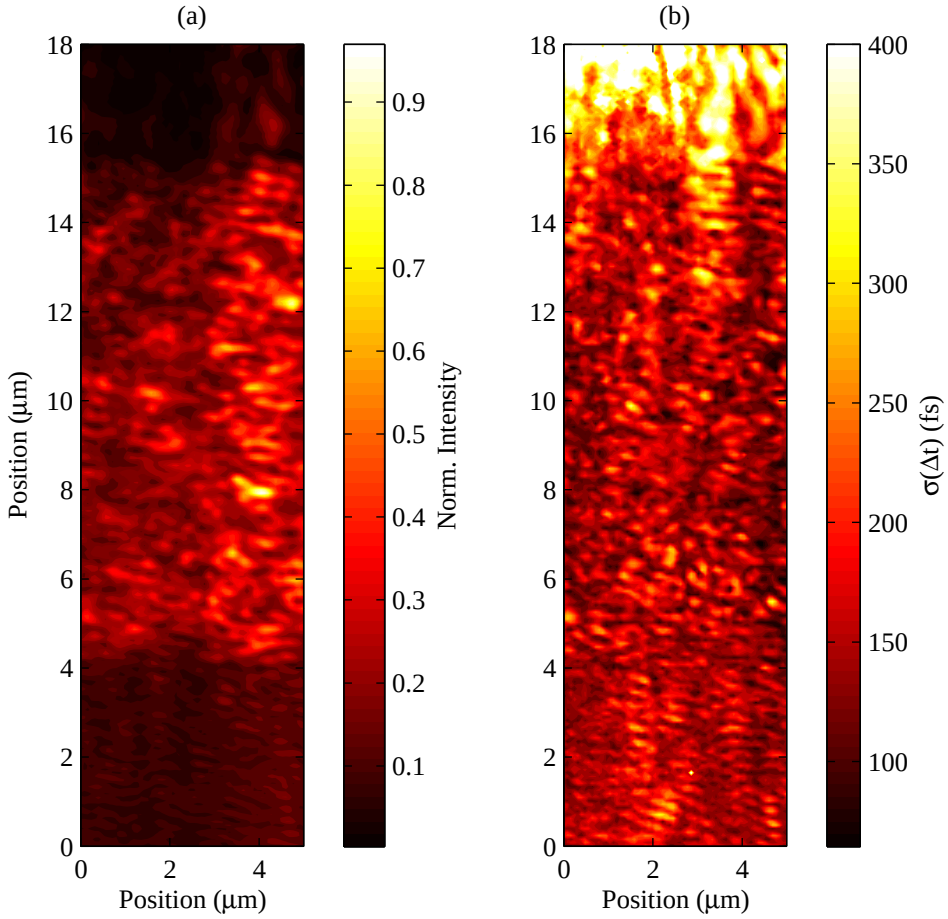

Figure 6.6: (a)The total intensity (for all wavelengths) map for the SNOM scan of the pinwheel waveguide sample. The pinwheel region is identifiable visibly as the region containing greater intensity between 4 μm $\leq y \leq$ 15 μm. (b) The variance of the absolute autocorrelation field for delay values greater than 50 fs, as a function of position.

absolute field values above 50 fs as a function of position on the sample. The intensity features on the intensity map plot do not correlate with any features in the autocorrelation variance. The autocorrelation variance image does not indicate any locations where delays caused by the sample structure are noticeably greater than at other locations. This lack of correlation is not discouraging as it suggests that the pinwheel structure can indeed be considered as quasi-isotropic. No feature of the intensity or delay values reveal the structure of the device; the delay values appear to be homogeneously distributed within the pinwheel sample.

6.2.2 TEMPORALLY DISCRIMINATED SIGNALS IN THE SAMPLE

The autocorrelation width, as plotted on the right side of figure 6.6, can only provide an indication of areas that acquire signals with a large delay. As discussed in the previous section, even this indication is subject to poor accuracy, as the large number of scatterers produce artefacts in the autocorrelation amplitude maps. Thus the variance in autocorrelation widths does not provide insight into the scattering paths down which light has propagated. To provide this insight, the signals in the pinwheel sample must be discriminated a specified time delay to other propagating signals.

The absolute autocorrelation field at a specified time delay Δt (indicated above plots) is presented (top plots) above the phase angle for such fields (below), as determined by Fourier analysis of the spectra collected from the pinwheel sample, in figure 6.7. The pinwheel region is indicated by horizontal lines (white for the top plot, green for the bottom plot). The plots of autocorrelation amplitudes corresponding to a delay of 100 fs or greater, suggest that the signals of a particularly long delay have a spatial localisation. This is most notable for the plot corresponding to a time delay of 150 fs (3^{rd} plot from left), where the spatial extent of the strongest signal is highlighted by the presence of the colour yellow. The signals appear to be localised to a narrow column that is centred around $x = 2\ \mu$m. Similarly, for a time delay of 210 fs this route is highlighted by the lighter shades of blue and, for a time delay of 100 fs, is highlighted by the presence of the colour red. Not easily shown in static plots, the presence of this route appears across a continuous range of time delays. This suggests that this spatial localisation is not imposed by some resonance condition which supports an argument for disorder-based localisation perpendicular to the propagation axis. Interference fringes between the autocorrelation fields at specific time delays do not provide any obvious insight into the scattering behaviour of the sample. For this information to be of more use, further work must be done on simpler scattering samples so that the presence of

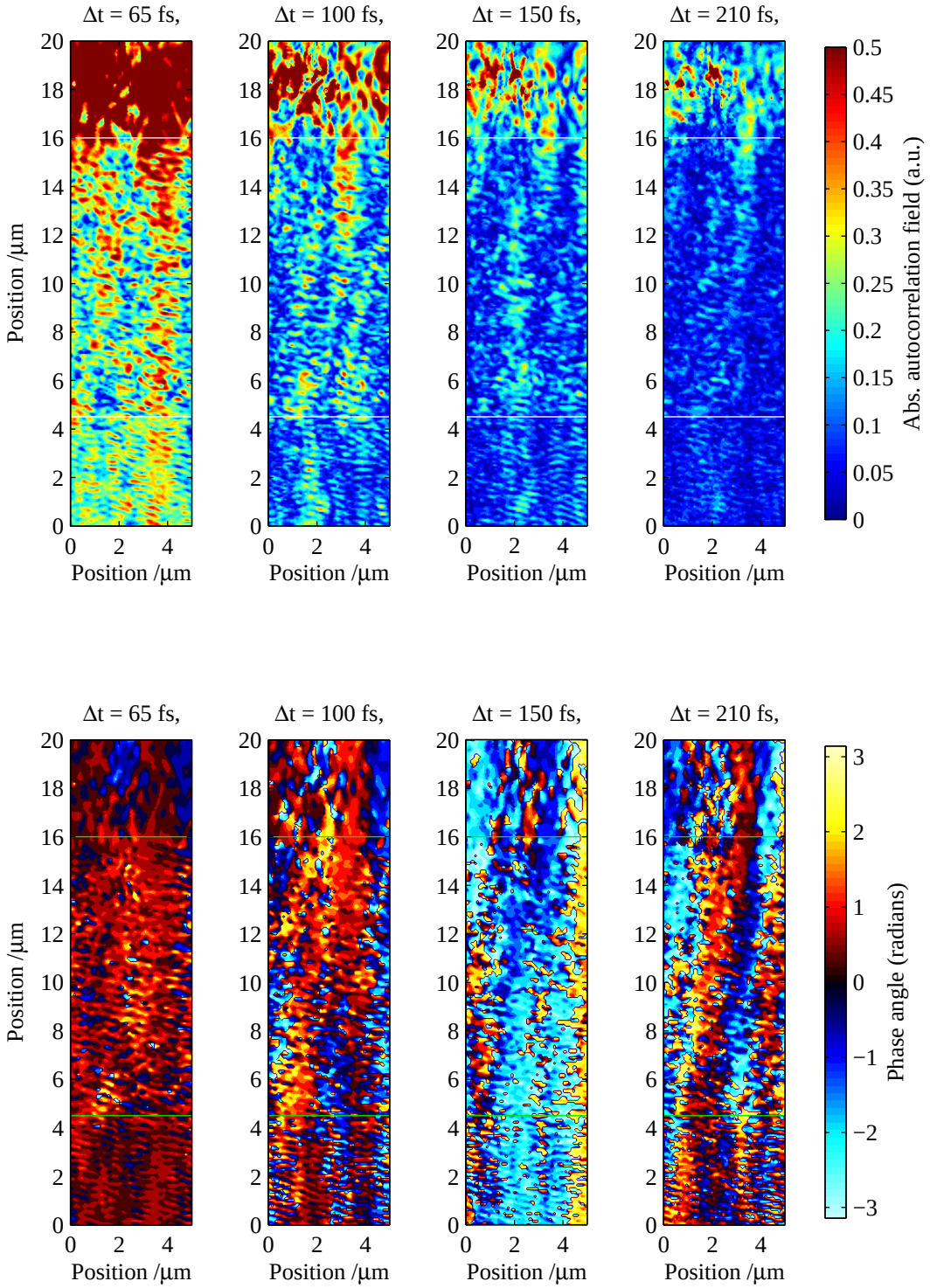

Figure 6.7: (top) local absolute field for time delay Δt (specified above plots) with the pinwheel region enclosed between the horizontal white lines. (bottom) the phase angle map for the local autocorrelation field for time delay Δt (specified above plots).

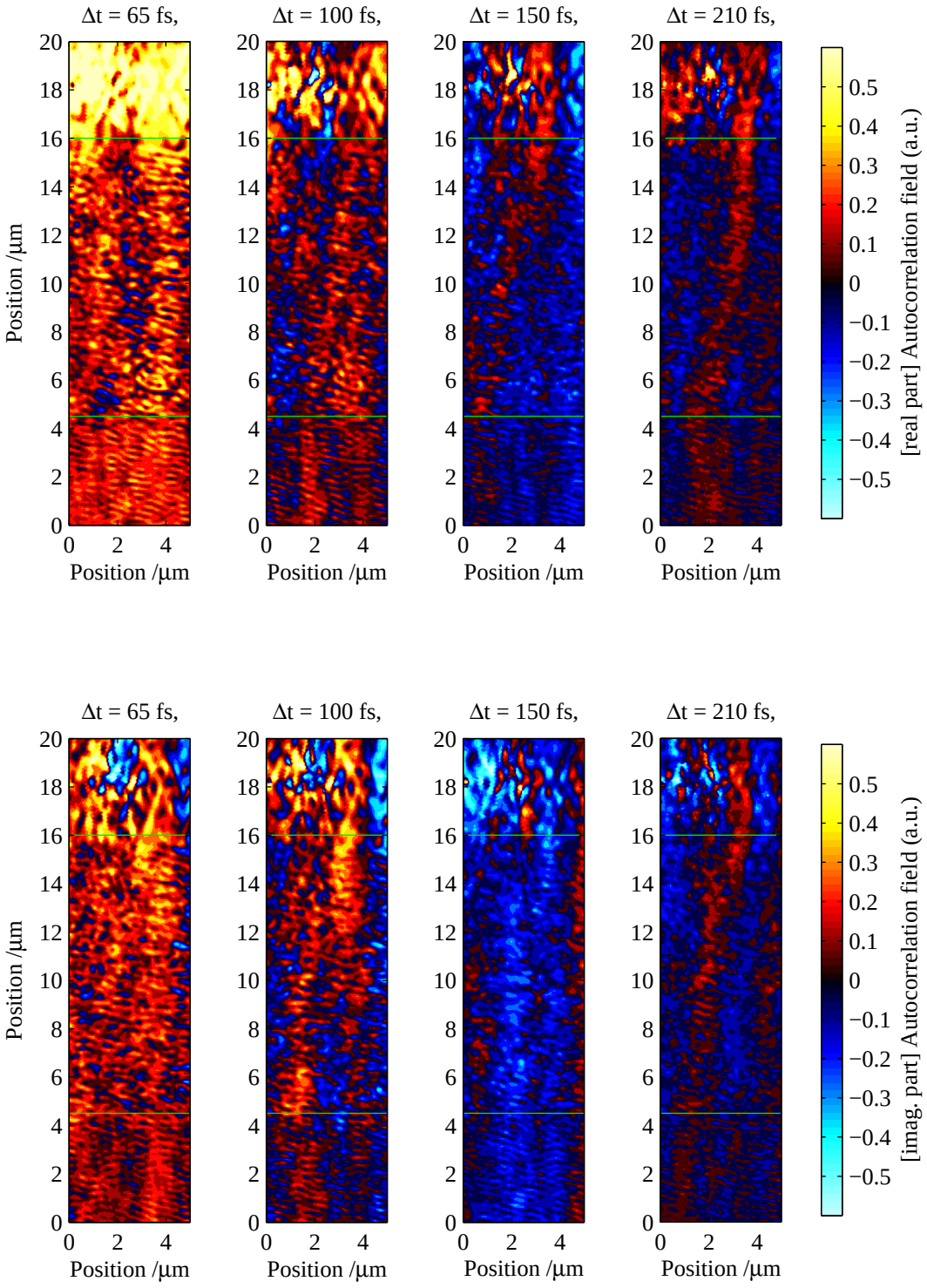

Figure 6.8: (top) the real part of the autocorrelation field for a time delay Δt (specified above plots) with the pinwheel region enclosed between horizontal green lines. (bottom) the imaginary part of the autocorrelation field for a time delay Δt (specified above plots)

features in the autocorrelation field maps can be attributed to scattering phenomena.

As discussed previously, for a sample with a large number of scatterers, the behaviour of interference fringes in the absolute autocorrelation field maps is the method most likely to reveal the scattering behaviour of the waveguide. Since interference fringes are related to the sum of fields with various phase angles, the phase angle map is present in the bottom plot of figure 6.7. The complexity of the scattering sample creates a range of phase angles for specific delays, thus no obvious scattering behaviour is revealed in these plots. Large areas of approximately constant phase angle appear to create near-vertical features in the phase angle maps for a delay of $\Delta t = 210$ fs (seen as a near vertical column of red with the colour map used in the plot), this could be attributed to the propagation of two plane waves with an angle to one another or a high-probability route that the light traverses with this delay. The latter interpretation is less likely since a delay of 210 fs corresponds to a propagation distance difference of $\frac{c}{n_g}\Delta t = 52\ \mu$m and a high probability for a scattered wave to return to its site of origin after propagating this distance is unlikely.

The phase angle map does not show the field amplitude levels. Plotting the real and imaginary parts of the autocorrelation field maps for a specified time delay provides a method of displaying the relative phase trends between time delayed signals and the ratio in their amplitudes. Such plots are presented in figure 6.8, where the real and imaginary parts of the autocorrelation field map for the time delays specified in figure 6.7 are presented. However, in the infancy of interpreting these temporally discriminated autocorrelation field maps, no obvious insights into the scattering phenomena occurring within the pinwheel sample is presented.

The temporal discrimination of autocorrelation fields has been presented for the pinwheel sample data from chapter 5, however it has been unable to identify temporal phenomena occurring in the sample conclusively. With certain enhancements however, the potential for this technique to view temporal phenomena an the nanometre scale remains. The next section discusses some improvements and further experiments that need to be done to better understand the information presented in the autocorrelation field maps.

6.3 TEMPORAL DISCRIMINATION AS A FUTURE TOOL

The temporal discrimination has been applied to the pinwheel sample data and has not been able to provide a complete picture of the scattering phenomena inside the sample. However, the setup used for collecting this data provided limited temporal

resolution. To observe the scattering phenomena that is occurring on the scale of the sample, a time resolution corresponding to a propagation distance comparible to the pinwheel tiling pitch is needed. Supercontinuum sources may provide the bandwidth necessary to observe temporal phenomena occuring within the sample presented here, but their complex power spectrum would complicate the interpretation of features in the autocorrelation maps.

To understand better the information presented in the temporal discrimination plots, scans on simpler scattering samples is also necessary. This would demonstrate the ability of the technique to identify the location of scattering sites. The ability to provide temporal discrimination plots of single scattering sites may also provide a practical way for measuring the group velocity in the planar layer of a PLC, by observing the spatial evolution dependence across specified time delays.

- CHAPTER 7 -

CONCLUSIONS & FUTURE WORK

The ability of a spectrally resolving SNOM to interrogate and determine various properties of optical waveguides has been demonstrated in thesis. This chapter summarises the key findings presented in this thesis and the significant results obtained in this work.

7.1 KEY RESULTS

A spectrally resolving SNOM system was developed as part of this project. The various technologies employed to realise such a SNOM system was presented in chapter 3. The use of a flexure stage with an integrated piezo actuator provided a scanning range of 4 mm x 4 mm with a resolution of 5 nm. Such a scanning range has enabled the direct observation of spatial beats between modes along the propagation distance, as presented in figure 4.4. This measurement ability enables the direct determination of the effective index difference between two propagating modes.

Chapter 4 presented basic waveguide theory for explaining the source of waveguide modes and their corresponding dispersion characteristics. Then the spectrally resolving SNOM system was used to directly measure the relative group velocity between two modes in a waveguide[1, 2]. This was achieved by observing the spectral interference on a source spectrum at a specific location along the guide. The measurement of inter-modal dispersion properties is of interest as multimode devices are studied as a route for extending current single mode technologies[3]. The local spectra collected from the guide enabled the relative phase profile of the modes to be determined by observing the spatial profile of the autocorrelation field for a specified time delay, similar to the method used by Nicholson *et al.* for analysing the modal content of multimode fibres[4].

In chapter 5, the spectrally resolving SNOM system was used to obtain local spec-

tra from a random scattering sample that was based on Conway's pinwheel tiling pattern. Spectral data was used to identify the delicate spectral response of the random scatterer and any evidence of effects due to the photonic bandgap nature of the sample. The measurements taken revealed an enhanced intensity response for a particular wavelength, however this could not be attributed to the Bragg condition of any ubiquitous scatterer spacing found inside the pinwheel tiling. The sample was also studied because, after modelling the electric field response of the sample, it was suggested that Anderson localisation may occur within the structure[5]. The SNOM did reveal that spatial localisation existed inside the pinwheel tiling, however the behaviour of such localisation could not be confirmed as Anderson localisation.

Investigating the temporal phenomena that may occur within the pinwheel sample was presented in chapter 6 The temporal discrimination of autocorrelation field was used to map the location of delays that occur in the guide as a consequence of random walk paths. With limited temporal resolution, the delays accrued by the light at the dimensions of the scatter sites were unresolvable. However, interference in the spectra that corresponded to a delay of 200 fs between signals highlighted a route inside the sample that light may be travelling because of similar spatial localisation discussed in chapter 5.

7.2 FUTURE WORK

This project has demonstrated examples of how a spectrally resolving SNOM can provide insight into the guiding properties of waveguides. Some suggestions for future projects using the spectrally resolving SNOM system are now presented.

7.2.1 TEMPORAL DISCRIMINATION OF SCATTERING SAMPLES

To better understand the information presented in the temporal discrimination plots, studies on simple weak scattering systems should be considered. The strong scattering caused by the sample studied in chapter 5 resulted in a large reduction of the incident power put into the sample, indicating that the propagation of the incident wave was greatly affected by the sample. In weakly scattering systems, the incident wave can be used as a reference wave for any delays created by the scattering process leading to easier interpretation of spatial existence of delays identified in the temporal discrimination plots.

For the investigation of disorder based location, the bandwidth of the source used

must provide a temporal resolution that corresponds to a propagation distance inside the guide of similar distance to the scattering site spacings. This would be better suited (than the current setup) for identifying delays caused by a few scattering events in strongly scattering samples. Supercontinuum sources may provide the necessary bandwidth to observe the temporal phenomena occuring at the length scale of the scattering sites.

Only Rayleigh scattering has been considered when investigating the temporal delays in waveguides in this thesis. Studies on the local delays caused by other, non-elastic, scattering mechanisms could provide insights into phenomena that could be used for the processing of information optically.

7.2.2 Mode propagation in multimode devices

The work presented in this thesis presented the ability of SNOM to observe the relative group delay between two propagating modes in a ridge waveguide at an arbitrary location along the waveguide. By utilising existing methods for measuring dispersion in optical fibre, the absolute dispersion properties may be determinable. For multimode devices, it has been shown that a radio frequency modulated tunable laser, can determine the absolute dispersion properties of modes propagating in an optical fibre[6]. If used with a SNOM system, the local dispersion properties of multimode (and single mode) PLCs could be directly determined for complex geometries, which would otherwise require numerical simulations.

REFERENCES

[1] Sam A Berry, James C Gates, and William S Brocklesby. Direct spatial-temporal discrimination of modes in a photonic lightwave circuit using photon scanning tunnelling microscopy. In *CLEO/Europe and EQEC 2011 Conference Digest*, OSA Technical Digest (CD), page CF_P19. Optical Society of America, May 2011.

[2] Sam A Berry, James C Gates, and William S Brocklesby. Determination of spatio-spectral properties of individual modes within multimode waveguides using spectrally resolved near-field scanning optical microscopy. *Applied Physics Letters*, 99(14):141107, 2011.

[3] Jonathan R Kurz, Jie Huang, Xiuping Xie, Takashi Saida, and Martin M Fejer. Mode multiplexing in optical frequency mixers. *Optics Letters*, 29(6):551, March 2004.

[4] Jeffrey W Nicholson, Andrew D Yablon, John M Fini, and Marc D Mermelstein. Measuring the Modal Content of Large-Mode-Area Fibers. *IEEE Journal of Selected Topics in Quantum Electronics*, 15(1):61–70, January 2009.

[5] Tom D M Lee. *Investigation of highly symmetric photonic quasi crystals*. PhD thesis, University of Southampton, 2006.

[6] J W Nicholson, S Ramachandran, S Ghalmi, E A Monberg, FV DiMarcello, M F Yan, P Wisk, and J W Fleming. Electrical spectrum measurements of dispersion in higher order mode fibers. *IEEE Photonics Technology Letters*, 15(6):831–833, June 2003.